

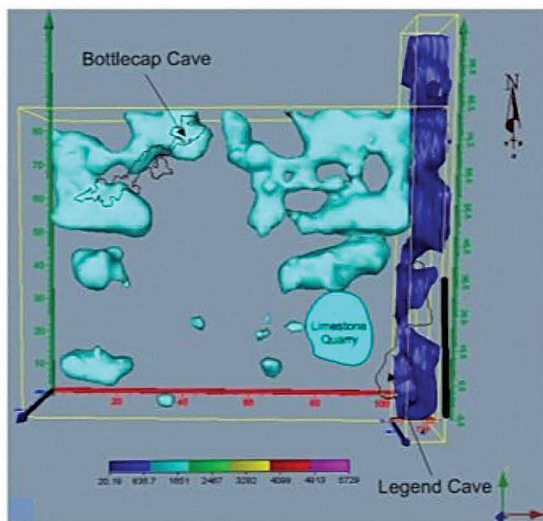
# JOURNAL OF CAVE AND KARST STUDIES

March 2022  
Volume 84, Number 1  
ISSN 1090-6924  
A Publication of the National  
Speleological Society



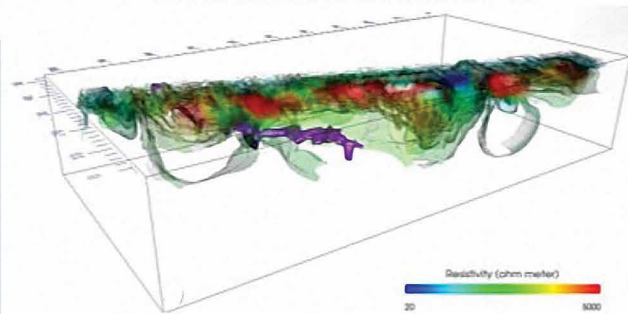
A

3D SITE MODEL



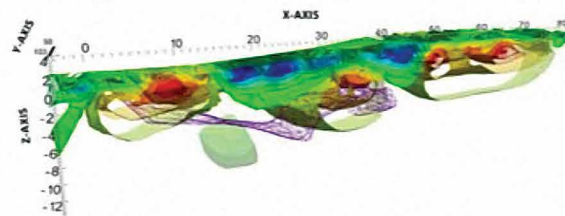
B

3D MODEL OF BOTTLECAP CAVE (MODEL 6)



C

3D MODEL OF LEGEND CAVE (MODEL 7)



DEDICATED TO THE ADVANCEMENT OF SCIENCE,  
EDUCATION, EXPLORATION, AND CONSERVATION

**Published By  
The National Speleological Society**

<http://caves.org/pub/journal>

**Office**

6001 Pulaski Pike NW  
Huntsville, AL 35810 USA  
Tel:256-852-1300  
nss@caves.org

**Editor-in-Chief  
Malcolm S. Field**

Washington, DC  
703-347-8601  
field.malcolm1@gmail.com

**Production Editor  
Scott A. Engel**

Knoxville, TN  
225-281-3914  
saecaver@gmail.com

The *Journal of Cave and Karst Studies*, ISSN 1090-6924, CPM Number #40065056, is a multi-disciplinary, refereed journal published four times a year by the National Speleological Society. The *Journal* is available by open access on its website, or check the website for current print subscription rates. Back issues are available from the NSS office.

POSTMASTER: send address changes to the National Speleological Society Office listed above.

The *Journal of Cave and Karst Studies* is covered by the following ISI Thomson Services Science Citation Index Expanded, ISI Alerting Services, and Current Contents/Physical, Chemical, and Earth Sciences.

Copyright © 2022  
by the National Speleological Society, Inc.

**BOARD OF EDITORS**

**Anthropology**

**George Crothers**  
University of Kentucky  
Lexington, KY  
george.crothers@utk.edu

**Conservation-Life Sciences**

**Julian J. Lewis & Salisa L. Lewis**  
Lewis & Associates, LLC.  
Borden, IN  
lewisbioconsult@aol.com

**Earth Sciences**

**Benjamin Schwartz**  
Texas State University  
San Marcos, TX  
bs37@txstate.edu

**Yongli Gao**

University of Texas at San Antonio  
yongli.gao@utsa.edu

**Mario Parise**

University Aldo Moro  
Bari, Italy  
mario.parise@uniba.it

**Carol Wicks**

Louisiana State University  
Baton Rouge, LA  
cwicks@lsu.edu

**Exploration**

**Paul Burger**

National Park Service  
Eagle River, Alaska  
paul\_burger@nps.gov

**Microbiology**

**Kathleen H. Lavoie**

State University of New York  
Plattsburgh, NY  
lavoiekh@plattsburgh.edu

**Paleontology**

**Greg McDonald**

National Park Service  
Fort Collins, CO  
greg\_mcdonald@nps.gov

**Social Sciences**

**Joseph C. Douglas**

Volunteer State Community College  
Gallatin, TN  
615-230-3241  
joe.douglas@volstate.edu

**Book Reviews**

**Arthur N. Palmer & Margaret V Palmer**

State University of New York  
Oneonta, NY  
palmeran@oneonta.edu

Front cover: Resistivity survey models in the study by McCrackin et. al. in this issue.

## 3D RESISTIVITY SURVEY OVER MAPPED CAVES IN EOGENETIC KARST TERRANE, WEST-CENTRAL FLORIDA, USA

Charles W. McCrackin<sup>1</sup>, Henok G. Kiflu<sup>2</sup>, Sarah E. Kruse<sup>2</sup>, Philip E. van Beynen<sup>2</sup>, Jason S. Polk<sup>3,C</sup> and Ben. Miller<sup>4</sup>

---

### Abstract

This study assesses the capability and practical applications of quasi-3 Dimensional (3D) Electrical Resistivity Tomography (ERT) for mapping air-filled conduits in eogenetic karst. A high-resolution quasi-3D ERT survey, consisting of multiple parallel 110m-long 2D profiles, was conducted over two mapped cave systems on the Brooksville Ridge, Florida. The irregularly shaped caves have diameters ranging up to 4 m and span depths from 3 m to 11 m below ground surface. Dipole-dipole array geometries with  $L_2$  (least squares) rather than  $L_1$  (robust) inversion produced the best fits of resistivity highs with the mapped cave locations. As expected, 3D inversions of sets of parallel lines produced better results than 2D inversions of individual transects. Better imaging was obtained of a cave over which cave-parallel profiles were run in addition to cross-cave profiles. However, even with the best acquisition and processing steps, there are significant misfits in the apparent size of the large cave sections, and narrower conduits are not imaged. Resolution decreased significantly with depth, as expected given the method limitations and the site constraints on profile lengths. 3D visualization techniques are explored, and found helpful in examining the data and comparing mapped caves and 3D resistivity datasets; however, when applied to eogenetic karst terrain, ERT has limited capacity to detect smaller cavities, which may require the additional use of other geophysical or subsurface investigative methods. With sinkholes continuing to be of concern to residential and urban development in west-central Florida, the results of this research present additional insight on the potential of quasi-3D ERT methods to map and characterize the potential hazards posed by karst terranes.

---

### INTRODUCTION

Electrical Resistivity Tomography (ERT) can be an effective detection method for caves and voids in karst terrain (e.g., Doll et al., 1998; Schoor, 2002; Gibson et al., 2004; El-Qady et al., 2005; Leucci and De Giorgi, 2005; Parise and Gunn, 2007; Ezersky, 2008; Abu-Shariah, 2009; Pánek et al., 2010; Gambetta et al., 2011; Kaufmann et al., 2011; Zhu et al., 2011, McCormack et al., 2017; Prins et al., 2019). ERT methods are sensitive to the resistivity contrast between the host bedrock material and the void space. When caves exist in the vadose zone, the empty void space has a higher resistivity than the host rock. In the phreatic zone, water-filled cavities generally appear as resistivity lows against the host rock background (Zhu et al., 2011; Land et al., 2012; Gary et al., 2013; Redhaounia et al., 2016; Majzoub et al., 2017; Nazaruiddin et al., 2017; Redhaounia et al., 2017).

The use of geophysical techniques for void detection was pioneered in telogenetic karst settings (Crawford, 1989; Crawford et al., 1999), where the rock has undergone diagenesis and compaction, and the porosity is often low, with voids existing in long, linear pathways following joints or bedding planes (Palmer, 2007). Such terranes include much of the southeastern and central United States. In contrast, eogenetic karst regions, such as Florida and much of the carbonate islands of the Caribbean, contain geologically young limestones having high primary porosity and matrix permeability (Vacher and Mylroie, 2002). Voids in eogenetic karst systems present challenges to detection, compared to the extensive cylindrical voids that may form in mature karst. In eogenetic karst, both high primary porosity (Vacher and Mylroie, 2002) and a tendency of voids to fill with sediments (Jenson et al., 2006) act to reduce the resistivity contrast between caves and rock. Caves tend to be smaller and may be more complex in geometry due to the higher permeability bedrock and dominance of matrix flow overprinting structural controls that tend to guide void detection in telogenetic karst areas (Florea, 2006; Palmer, 2007). Both vertical shafts and horizontal voids are expected from varied processes near the surface and near the water table (Jenson et al., 2006). Nevertheless, detecting voids in young carbonate karst systems (eogenetic limestones) is increasingly important as a tool for mapping the potentiometric surface, petroleum extraction, and salt water intrusion threats (Lace and Mylroie, 2013).

With the advent of automated multi-electrode resistivity array systems, resistivity survey times have significantly decreased and have allowed for greater amounts of data to be collected. This has led to the more frequent use of two-dimensional (2D) and now three-dimensional (3D) ERT imaging (Loke et al., 2013). Traditional 2D ERT surveys

---

<sup>1</sup> Rimkus Consulting Group, Inc.

<sup>2</sup> University of South Florida

<sup>3</sup> Western Kentucky University

<sup>4</sup> United States Geological Survey

<sup>C</sup>Corresponding Author: jason.polk@wku.edu

have proven successful in the detection of various 3D features when these features are large compared to the electrode spacing. Examples of such features include sinkholes (Schoor, 2002; Kruse et al., 2006; Margiotta et al., 2012), landslides (Schrott and Sass, 2008; Pánek et al. 2010; Zhou and Beck, 2011), and caves (Leucci and De Giorgi, 2005; El-Qady, 2005; Abu-Shariah, 2009; Gambetta et al., 2011; Kaufmann et al., 2011); however, 2D ERT may not always be appropriate for mapping complex geology (Loke and Barker, 1996b; Roth et al., 2002; Zhu et al., 2011). A 3D survey may be best suited, particularly when a volumetric approach is required or when resolution of geometric detail is desired, as in archeological surveys (Loke and Barker, 1996b; Roth et al., 2002; Papadopoulos et al., 2006; Neyamadpour et al., 2010; Chambers et al., 2012). Additionally, 2D ERT surveys can suffer from artifacts generated by off-line 3D features in complex environments such as might be expected in eogenetic karst (Roth et al., 2002; Gharibi and Bentley, 2005; Martorana et al., 2009; Zhu et al., 2011).

With true 3D arrays, many varieties of array geometries are possible. Currently, most 3D resistivity surveys are quasi-3D surveys, in which data are collected along sets of parallel linear profiles with classic 2D geometries. Parallel profiles are then inverted as a 3D block unit. This process can be repeated with orthogonal line sets (Papadopoulos et al., 2006; Papadopoulos et al., 2010; Rucker et al., 2009; Neyamadpour et al., 2010; Chambers et al., 2012;).

Such quasi-3D geometries have been applied to image complex geologic structures in a variety of terrains (Loke and Barker, 1996b; Gharibi and Bentley, 2005; Neyamadpour et al., 2010; Kaufmann et al., 2012; Mohamed et al., 2019; Fu et al., 2020; Torrese, 2020), but have not, to our knowledge, been described in shallow, thinly mantled eogenetic karst terranes. The foci of this study are to assess surveying and modeling strategies using the quasi-3D ERT method. The study utilizes currently available commercial systems and software to examine the practical limitations of the method for detecting voids in eogenetic karst terranes.

## REGIONAL GEOLOGY

The ~100 m by 110 m study site is situated on the Brooksville Ridge of West-central Florida and within the Withlacoochee State Forest of Citrus County (Fig. 1). The Brooksville Ridge is an upland area of west-central Florida, which hosts dozens of air-filled caves and cover collapse sinkholes (Florea, 2006; Harley, 2007; Pace-Graczyk, 2007; Polk, 2009). The larger southern portion of the Brooksville Ridge, where the study area is located, is approximately 175 kilometers in length and varies from 15 kilometers to 100 kilometers in width. The ridge trends in a NW to SE direction and is parallel to the western edge of Florida's coastline. The elevation of the Brooksville Ridge ranges from 20 meters to 60 meters with irregular areas of limestone outcrops (White, 1970).

Florida Study Area

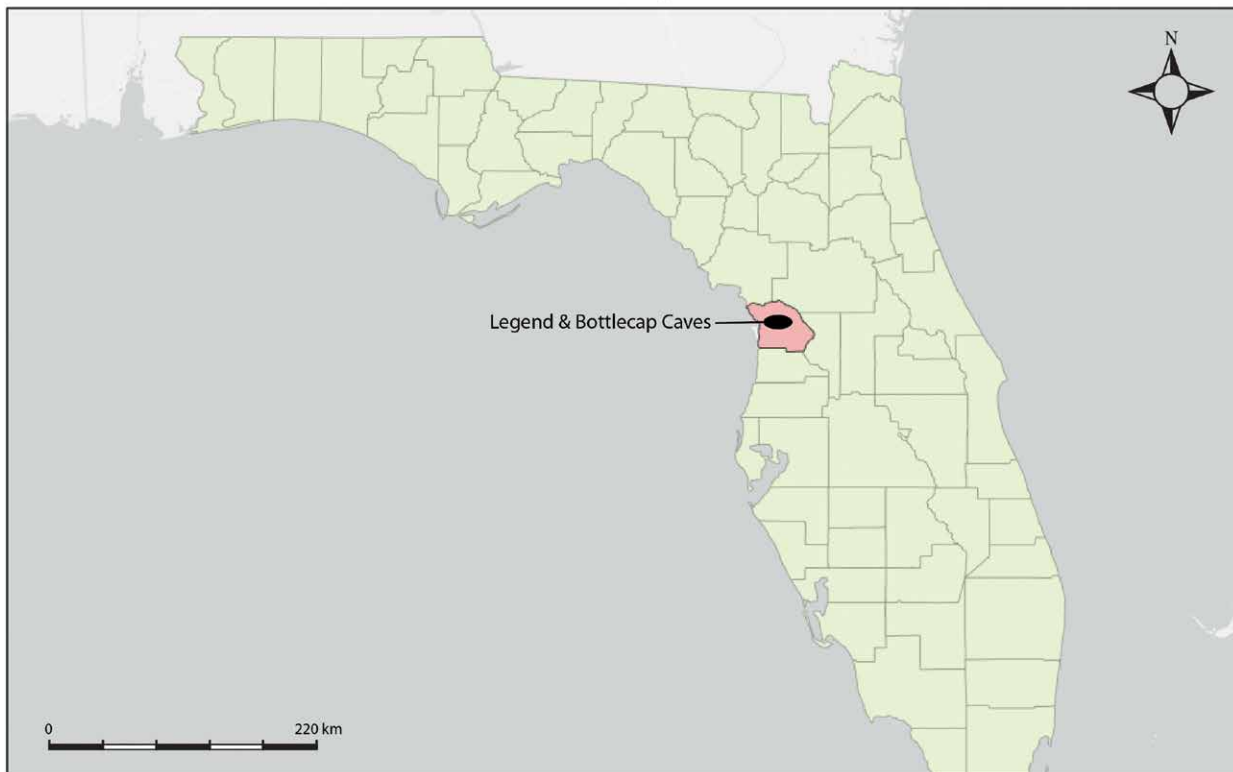


Figure 1. Location of Bottle Cap and Legend Caves on the Florida Peninsula.

The site was selected because it overlies two well-documented vadose caves, Legend Cave (Fig. 2) and Bottle Cap Cave (Fig. 3). Such caves are common features on the Brooksville Ridge, where changes in sea level have contributed to the formation of many vadose zone cavities (Sinclair et al., 1985; Brinkmann and Reeder, 1994; Florea, 2006). Many of these caves are characterized by a distinctive keyhole or diamond shape appearance that is a result of groundwater elevation responding to sea level fluctuations. Present day sea level is now approximately 30 meters to 45 meters lower than the Late Eocene time period (Lane, 1994). The vadose zone caves of the Brooksville Ridge are thought to have formed during periods of stability of Quaternary sea levels (Florea et al., 2007) although some passages in the caves do not adhere to this theory.

A strong correlation between Florida cave levels and marine terraces has been reported, suggesting a tiered system of subaerial caves on the Brooksville Ridge (Florea et al., 2007). Changes in sea level have significantly influenced the topography and the formation of caves in the state of Florida as indicated by the Marine Terraces and Shoreline of Florida Map (Healy, 1975). The two caves imaged in this study are located between the Wicomico and Penholoway terrace. The contact between the Wicomico and Penholoway terrace is at an elevation of approximately 21 meters, which corresponds with the elevation of the study area. Many of the cave passages on the Brooksville have been reported as similar in architecture and characterized by laterally extensive, air-filled cavities with bedrock pillars, dissolution features, and passages that often terminate in blind pockets (Florea, 2006). The groundwater table for this area is below a depth of 16 meters. Cave passages in the ridge generally are known to trend along a NE to SW and NW to SE system of fractures.

In this region, a thin veneer of Miocene (5 Ma to 23 Ma) siliciclastic sands and clays (Hawthorn Group) overlie highly karstified Suwannee Limestone, which, in turn, unconformably overlies the eogenetic Ocala Limestone (Scott, 2001). Outcrops of Oligocene Suwannee Limestone consist of dolostone to dolomitic limestone that is highly silicified with chert lenses. Where the Suwannee Limestone has been eroded away, the underlying Ocala Limestone can be found at the surface. This Late Eocene Ocala Limestone underlies most of Florida and is a soft, highly porous and permeable limestone, but can locally be less porous and permeable, because of the cementation by crystalline calcite (FGS, 2010). Numerous disappearing streams and springs are associated with the Ocala Limestone. At the surface, exposures of the Ocala limestone reveal caverns and solution pipes that result from intense karstification (Sinclair et al., 1985; Florea, 2006) and often develop into voids eventually leading to the formation of cover collapse sinkholes. Together, these limestone units form part of the intermediate confining unit of the Florida Aquifer System (Scott, 2001; FGS, 2010). In areas where Hawthorn deposits exist, the Hawthorn provides a cap of protection from dissolution, and directs water off the mixed sand and phosphatic clays into subsurface conduits, whereby cave development often occurs in the first 10–30 meters of bedrock (Polk et al., 2012). This is primarily due to the highly permeable (up to  $10^{-6}$  m s<sup>-1</sup>) rock, which can have an initial porosity of nearly 30 percent or more (Florea and Vacher, 2006).

This Late Eocene Ocala Limestone underlies most of Florida and is a soft, highly porous and permeable limestone, but can locally be less porous and permeable, because of the cementation by crystalline calcite (FGS, 2010). Numerous disappearing streams and springs are associated with the Ocala Limestone. At the surface, exposures of the Ocala limestone reveal caverns and solution pipes that result from intense karstification (Sinclair et al., 1985; Florea, 2006) and often develop into voids eventually leading to the formation of cover collapse sinkholes. Together, these limestone units form part of the intermediate confining unit of the Florida Aquifer System (Scott, 2001; FGS, 2010). In areas where Hawthorn deposits exist, the Hawthorn provides a cap of protection from dissolution, and directs water off the mixed sand and phosphatic clays into subsurface conduits, whereby cave development often occurs in the first 10–30 meters of bedrock (Polk et al., 2012). This is primarily due to the highly permeable (up to  $10^{-6}$  m s<sup>-1</sup>) rock, which can have an initial porosity of nearly 30 percent or more (Florea and Vacher, 2006).

**STUDY SITE**

At the study site, resistivity profiles were performed over Legend Cave (Fig. 2) and Bottlecap Cave (Fig. 3). Their entrances are ~100 m apart and separated by a limestone quarry pit approximately 20 m in diameter

**Legend Cave**

Citrus County, Florida

Cartography by Jason S. Polk, 3/2012  
 11/19/2011 survey by:  
 Grant Harley  
 Karmal Humagain  
 Glen Hunt  
 Charles McCrackin  
 Jason Polk

Datum: Station AG  
 (WGS 82 NAD 83)  
 Datum Elevation: 80 feet (24 m)  
 Surveyed length: 147 ft (44 m)  
 Surveyed depth: 26 ft (8 m)  
 Cave is formed within the  
 Ocala Limestone.  
 Cave is on Wilcoxcohee State Forest property  
 Permit required for entry.

Key To Features	
	Sediment floor
	Trench
	Large breakdown
	Small breakdown
	Bedrock pillar
	Entrance pit
	Bonus
	Passage
	Sink Stream
	Pit Depth (ft)
	Change in ceiling height
	Change in floor height
	Change in ceiling
	Intermittent Stream
	Direction of slope
	Survey station
	Ceiling height (ft)
	Breakdown Slope
	Stalagmite
	Stalactite
	Column

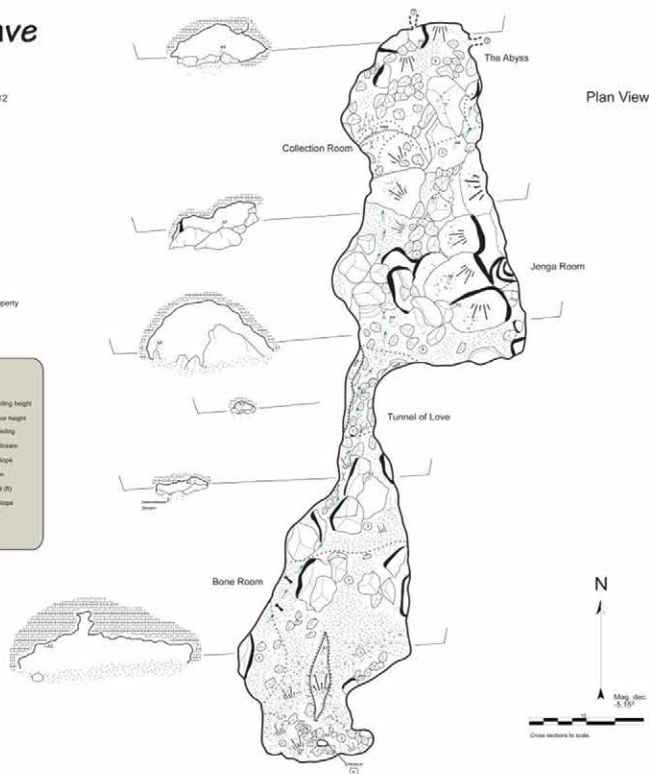


Figure 2. Map of Legend Cave, Citrus County, Florida (Polk, unpublished).

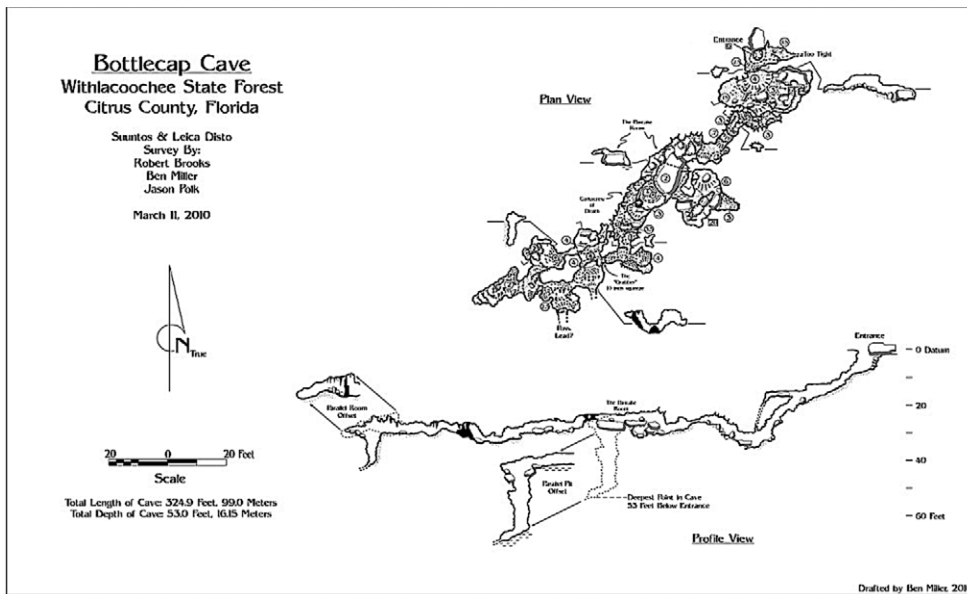


Figure 3. Map of Bottlecap Cave, Citrus County, Florida.

and approximately 3 m to 7 m in depth. The limestone quarry has a water table that is perched for most of the year. The quarry is underlain by organic and clayey soils that overlie the siliceous Suwannee Limestone.

The entrance to Legend Cave is located at the southeast corner of the quarry pit and the cave trends in a N-S direction at the eastern boundary of the site. A detailed cave survey measured a depth of approximately 3 m to 9 m below land surface and a length of 44 m (Fig. 2). Legend Cave consists of three large rooms separated by two narrow, collapsed passages located at the central and north-central portions of the cave. Consider-

able breakdown from roof collapse and infilling of sediments are readily visible. Roof collapse has blocked the far north end of the cave and prevented further exploration.

Bottlecap Cave trends in a NE-SW direction with an entrance at the northwest portion of the site. This cave is characterized by small circular conduits. Cave depth ranges from 6 m to 11 m below the surface with a surveyed length of 107 m (Fig. 3). A dry vertical shaft that extends to a depth of approximately 18 m below datum is the deepest part of the cave. No groundwater is present in either cave.

The geometries of both Bottlecap and Legend Cave suggest relatively simple linear structures, which have undergone extensive dissolution, collapse, and partial sediment in-filling. Cave development occurred during past periods of higher sea levels and groundwater flow. Currently, meteoric waters are washing the clayey Hawthorn sediments into the caves, with thicker sediments at the entrances and subsequent thinning of sediments further into the caves. Large limestone blocks from roof collapse prevent the exact identification of the lowest levels of the caves. Cave walls are often irregular due to extensive breakdown of the eogenetic bedrock, and thus, unclear structural controls on localized passage development. Although the limestone surface in the caves is generally dry, various zones of saturated rock were observed along fractures in the roof and walls. Variable topography, irregular limestone surfaces and passage development, and infilling of sediments in the relatively simple caves present a complex subsurface geology for geophysical imaging, and clearly limits precise delineation of the cave's true extent. Most notably, collapse structures at the ends of the caves suggest potential inaccessible voids.

## ARRAY GEOMETRY

For the quasi-3D process, the user runs a series of parallel 2D profiles. In this study, we sought to select from 2D array geometries that are available, pre-programmed by commercial software or hardware manufacturers, and thus readily used by practitioners in the field. The broader field of optimal selection of arbitrary combinations of readings is a topic of current research, but the capacity to generate specifically optimized arrays remains beyond the reach of the typical end-user at present (Loke et al., 2013). Pre-programmed 2D arrays typically available are the Dipole-Dipole, Wenner, and Inverse-Schlumberger arrays (Fig. 4). Selecting the most appropriate array type depends on survey goals, site geology, and structure of the feature being surveyed (Dahlin and Zhou, 2004).

Each of these arrays has previously been used for cavity detection (Gharibi and Bentley, 2005; Neyamadpour et al., 2010; Pánek et al., 2010). The Wenner and Inverse Schlumberger arrays have a higher signal to noise ratio and a deeper depth of investigation compared to other arrays (Dahlin and Zhou, 2004; ASTM D 6431-99). We note the Inverse-Schlumberger array mimics a traditional Schlumberger array, but with the roles of outer current and inner potential electrodes switched to outer potential and inner current (Fig. 4). Many multi-electrode resistivity systems are now available in a mode such that, potential differences between multiple pairs of electrodes can be measured and recorded simultaneously. The Wenner array geometry cannot exploit the capability of such multi-channel systems so acquisition is slower per potential-current pair combination than for other geometries. Dipole-Dipole surveys in particular yield a high number of measurements in the near-surface and offer good horizontal resolution, and are thus well suited for



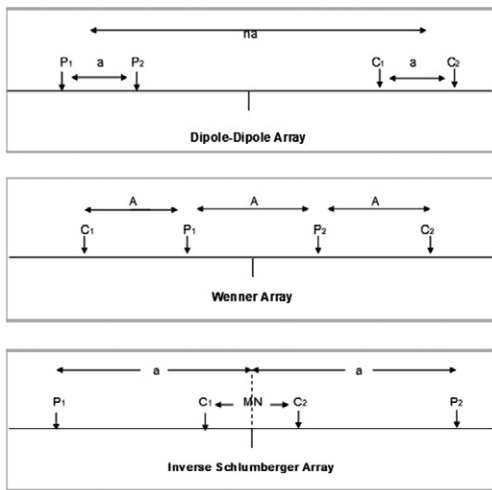


Figure 4. Dipole-Dipole, Wenner, and Inverse Schlumberger array type.

mapping complex structures (Dahlin and Zhou, 2004). The Dipole-Dipole geometry can also provide better resolution of higher resistive anomalies (Martorana et al., 2009; Pánek et al., 2010). As a result, the Dipole-Dipole array has proven to be one of the more effective array types for cavity detection (Cardarelli et al., 2010; Neyamadpour et al., 2010; Kaufmann et al., 2011); however, the Dipole-Dipole array suffers from a lower signal to noise ratio (Dahlin and Zhou, 2004; Gharibi and Bentley, 2005) and is especially susceptible to near-surface artifacts from electrode spacing errors, thus combining it with a strong-gradient array may improve the ability to resolve irregularities in the subsurface.

In this case study, in which lateral variability (the presence of caves) is our primary target, we consider the relative value of Dipole-Dipole and Inverse Schlumberger measurements and their combination. The slower Wenner arrays with lower lateral resolution were not acquired.

In addition to the type of array(s) selected, consideration of array orientation and electrode spacing is critical to image quality (Jackson et al., 2001; Gharibi and Bentley, 2005; Abu-Shariah, 2009; Pánek et al., 2010; Cardarelli et al., 2010; Zhu et al., 2011; Leucci et al., 2016). For the interpretation of a single profile over an elongated cave, it is clearly desirable

to orient the profile perpendicular to the cave. The optimal orientation for quasi-3D approach, however, will depend on target shapes. Gharibi and Bentley (2005) suggest that closely spaced transect lines in one direction may be more beneficial than orthogonal transects with a larger electrode spacing.

### Optimal Inversion Methods

Once the readings are acquired, the terrain resistivity is determined by inverting the raw data for the best-fitting underlying structure. The definition of best-fit typically falls into one of two categories: an L2-norm (Least-Squares or Smooth) inversion in which a weighted mean square error (between readings and model predications) is minimized, and an L1-norm (Robust) inversion in which a weighted mean absolute error is minimized (Loke and Barker, 1996a; Dahlin and Zhou, 2004; Gharibi and Bentley, 2005; Catt et al., 2009; Cardarelli et al., 2010). While both methods have been successfully used to resolve cavities, selecting the most appropriate inversion depends largely on the target type, target geometry, (Dahlin and Zhou, 2004; Catt et al., 2009) and the amount of noise in the dataset (Catt et al., 2009). With constraints on the smoothness of the model, the L2-norm inversion has been more commonly used (Loke and Barker, 1996; Jackson et al., 2001; Roth et al., 2002; Gharibi and Bentley 2005; Papadopoulos et al., 2006; Cardarelli et al., 2010, Zhu et al., 2011), although its inability to accurately resolve the position of geologic boundaries has been noted (Chambers et al., 2012). When mapping complex and abrupt geologic boundaries, the L1-norm (Robust) inversion, has been described as the more accurate of the two methods (Dahlin and Zhou 2004; Neyamadpour et al., 2009; Neyamadpour et al., 2010; Chambers et al., 2012). These studies also show that robust inversion works well with noisier data sets and may help to resolve 3D structures when lateral variations are more frequent. The two inversion methods are compared in this case study.

## METHODS

### Cave Mapping

Each of the caves in this study area was mapped to the Union Internationale de Spéléologie UIS “UISv1 5-4-B” survey grade with an expected overall accuracy of two percent (Häuselmann, 2010). A UIS Grade 5 level survey requires measurement length to be within 0.05 m of error, as well as compass (declination corrected) and clinometer readings to the nearest degree (Häuselmann, 2010). Surveys used foresight and backsight measurements of passage distances, inclinations, and azimuths, and all loops were closed and adjusted. The precision total length was within 0.05 m and the compass and clinometer readings within one degree of accuracy. Final survey data reduction was completed using COMPASS cave software to produce lineplots that were converted to 3D shapefiles and exported for 3D modeling via ArcGIS and used for final map drafting of features, which was completed in Adobe Illustrator (Legend Cave) and Xara (Bottlecap Cave) software (Kambesis et al. 2015). Both the surveyed length and total length measurements were used as appropriate in correcting for the 3D ERT survey. ArcGIS was used to georeference the cave entrances and passages relative to the ERT survey (Kambesis et al. 2015).

3D models of Legend and Bottlecap Caves were created using the plan and cross-sectional views from each of the cave maps using AutoCAD Civil 3D and Meshlab. These models are simplified versions of the cave geometry, designed to capture the major cave dimensions with an accuracy of ~0.5–1 m. This accuracy is higher than the typical

spatial resolution of the resistivity inversions at comparable depths, so is deemed sufficient for comparison of the cave locations and the resistivity data.

### Site Delineation

A fence along the access road was used as the baseline from which each ERT transect was measured. Survey boundaries and ERT transect endpoints were established using a Total Station GPS and locations were collected at the site boundaries to identify coordinates for georeferencing and positioning relative to georeferencing aerial imagery and LiDAR data.

A topographic map was created from the Citrus County LiDAR data obtained from the Southwest Florida Water Management District, which has vertical resolution of ~0.3 m (SWFWMD, 2006). The topographic data were used to generate a terrain correction for the ERT survey. Topographic relief is approximately 9 meters across the site.

### Survey Design

A 2D synthetic model was created to determine the optimum transect layout prior to surveying (Jackson, et al, 2001; Abu-Shariah, 2009; Catt et al., 2009). Based on the cave depths and the forward model results, a linear array of 56 electrodes was selected with an electrode spacing of 2 meters, which was a compromise between spatial resolution and depth of investigation. With a total line length of 110 meters, resistivity resolution below the cave depths was expected along the central portion of each profile. Parallel 2D transects were collected and spaced 4 meters apart so as not to exceed 2 times the electrode spacing (Gharibi and Bentley, 2005). The quarry pond and limestone outcrops prohibited acquisition in the southeast section of the site, and access prohibited data acquisition beyond the southern and eastern site boundaries and hence optimal resolution of Legend Cave. In total, there were 31 ERT transects with their direction and path selected for accessibility and to optimize coverage over the two known cave systems (Fig. 5a). On each profile, both the Dipole-Dipole and Inverse Schlumberger data sets were acquired.

### Resistivity Data Processing

Measurements for each of the ERT transects were processed and terrain corrected with EarthImager software 2D version 2.4.0 and 3D version 1.5.4 (32-bit). Outlying data points that had a relative data misfit greater than 40 percent to the inverse model predictions after 6 iterations were deleted. In general, data with a relative misfit of 50 percent or greater is considered poorly fit and should be removed (AGI, 2009). Fewer than five percent of the data points were selected for removal. Selected profiles were then inverted individually with 2D inversions. Profiles were then inverted with EarthImager's 3D inversion algorithm in batches of up to six adjacent profiles (Fig. 5b).

Computer memory limitations precluded a full 3D inversion of larger subsets of the data. This is a significant limitation of the method and has been previously noted (Rucker et al., 2009). Both 2D and 3D inversions were run for various combinations of data and inversion parameters, including Dipole-Dipole and Inverse Schlumberger and combination arrays,  $L_1$ -norm and  $L_2$ -norm error criteria, various convergence criteria to terminate iterations, and various smoothing criteria. Finally, results of 2D and 3D inversions were compared to slices through or volumes of the mapped cave positions. 2D plotting was done with EarthImager, 3D plotting was completed with EarthImager 3D and imported into Voxler 3D. Other forms of data processing, including 3D gridding of inverted resistivity data, may have assisted in generating void volume representations.

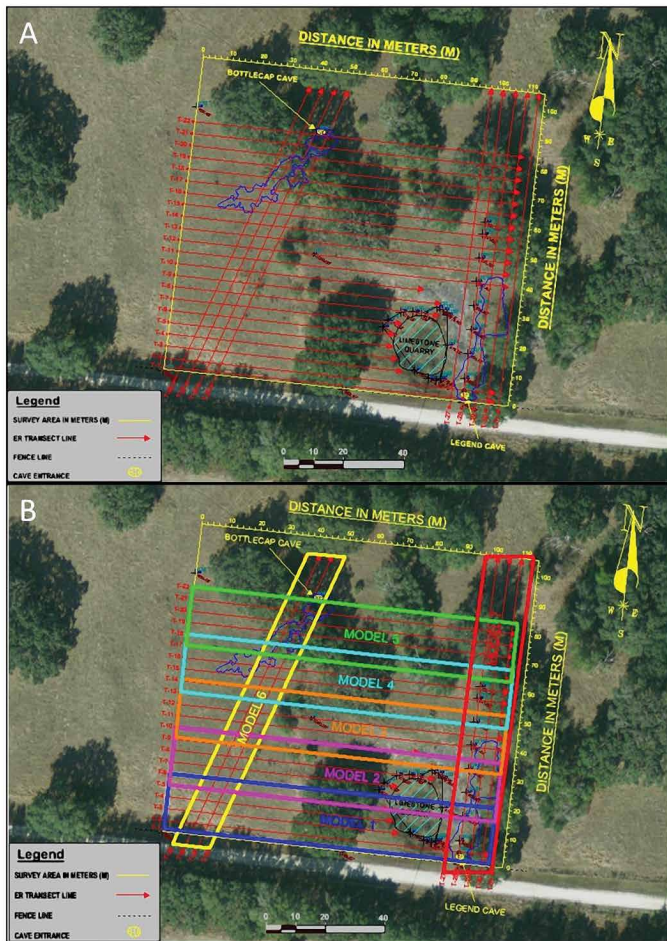


Figure 5. (a) View of the survey area with twenty-two (22) ERT transects performed in a west to east direction which trended from the south of Legend Cave to the north of Bottlecap Cave. Additionally, four (4) orthogonal transects were performed over the approximate centerline of Bottlecap Cave and five (5) orthogonal transects were performed over Legend Cave; (b) diagram showing the 7 models which were individually processed, terrain corrected, and imported into a larger 3D data set.



## RESULTS AND ANALYSIS

### Array Geometries

To assess the relative effectiveness of the Dipole-Dipole and Inverse Schlumberger array geometries, 2D inversion results for Transect 29 were compared against known cave position. Transect 29 closely tracks the centerline of Legend Cave, as shown in Figure 6a. For this test, the  $L_2$ -norm with EarthImager default inversion parameters were used. None of the 2D arrays properly captures information about the base of the cave, but the Dipole-Dipole and merged Dipole-Dipole and Inverse Schlumberger arrays show much more pronounced resistivity contrasts associated with the top of the northern section of the cave. The images generated from all three geometries show a distinctive shallow resistivity high to the north of the mapped caves (Fig. 6a). This feature is persistent in the data regardless of inversion method, and is discussed further below. For 3D inversions (of the data blocks as shown in Figs. 7 and 8) similar analysis showed that the Dipole-Dipole data gave subjectively better fits to the cave geometries.

### 2D vs. 3D Resistivity

3D inversions should theoretically yield improved matches between resistivity highs and mapped cave locations. Our data suggest this is generally the case at the study site. A 3D inversion profile was extracted from a block inversion consisting of three transects (Transects 28 thru 30).

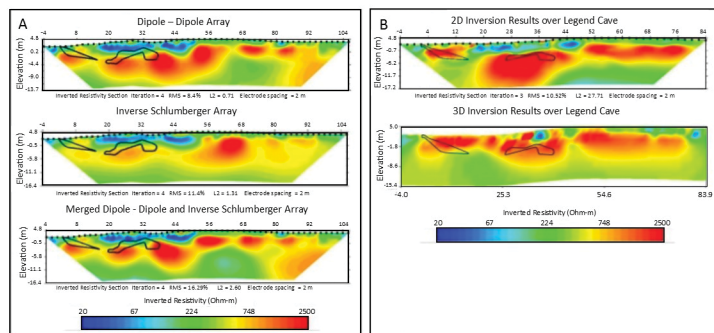


Figure 6. (a) 2D analysis of profile T29 (location shown on Figure 3) with different array geometries. The Dipole-Dipole and merged array geometries show a stronger resistivity contrast associated with the top of the cave; (b) comparison of 2D and 3D inversion profiles over the center of Legend Cave using the Dipole-Dipole array and  $L_2$ -norm inversion criteria

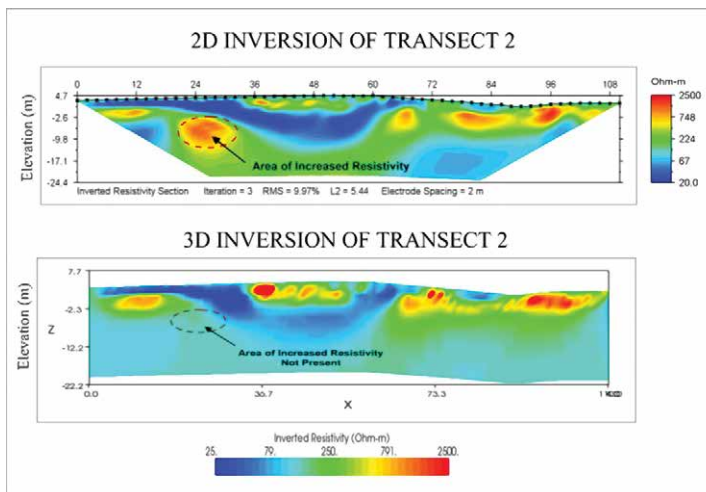


Figure 7. 2D inversion along Transect 2 indicates an isolated area of increased resistivity at 24 meters along the transect line, in comparison; 3D combined inversion of transects 1–3 shows no anomaly.

### Profile Orientation

To assess whether it is preferable to run transect lines parallel or perpendicular to elongated cave features, we compared the central profile of the 3D block consisting of transects T17–T22, Model 5 trending in an E–W direction, and perpendicular to the Bottlecap Cave (Figure 9a) against the central profile of a 3D block consisting of transections T32–

For comparison, 2D and 3D results are generated with  $L_2$ -norm EarthImager default criteria (Fig. 6b). Figure 6b shows the 2D inversion of the single central profile of T29 over Legend Cave in comparison to the central transect extracted from the 3D inversion block. Although the 2D result better fits the top of the northern portion of the cave, the 3D inversion better recovers the bottom and general structure of Legend Cave. We unfortunately have no direct observations to assess differences between the 2D and 3D models in the very near surface.

Figure 7 illustrates another example of differences between 2D and 3D inversions in this heterogeneous setting. Here profiles are compared which run along the southern boundary of the site that do not span a mapped cave feature. A 2D inversion of profile T2 indicates an apparent anomaly that is absent in a 3D inversion of profiles T1–T3.

### $L_1$ -norm and $L_2$ -norm Inversion Methods

We compared results from the  $L_1$ -norm and  $L_2$ -norm inversions at this study site. Figure 8 shows the two inversion types for the 3D grouping of four north-south profiles that traverse Legend Cave. For this study, the  $L_2$ -norm inversion yields a better fit in that it shows a resistivity high at the northern segment of Legend Cave. Overall, the  $L_2$ -norm smooth inversion was determined to be the method that better reproduced known features and was used for the 3D block results described below. It is important to note that others have reported best results with the  $L_1$ -norm robust inversion method (Loke and Barker, 1996a; Dahlin and Zhou, 2004; Gharibi and Bentley, 2005; Catt et al., 2009; Cardarelli et al., 2010). This may be related to site conditions, which are particularly heterogeneous in terms of host rock resistivity and the geometry of the target.

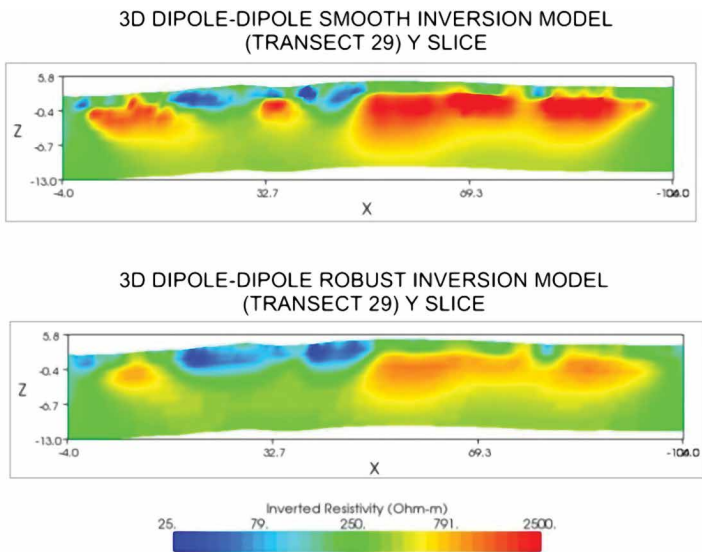


Figure 8. A comparison of the  $L_2$ -norm (smooth) inversion and the  $L_1$ -norm (robust) inversion. The profile was extracted along T29 from the 3D block model using profiles T28–T31 over Legend Cave (see Figure 3 for location).

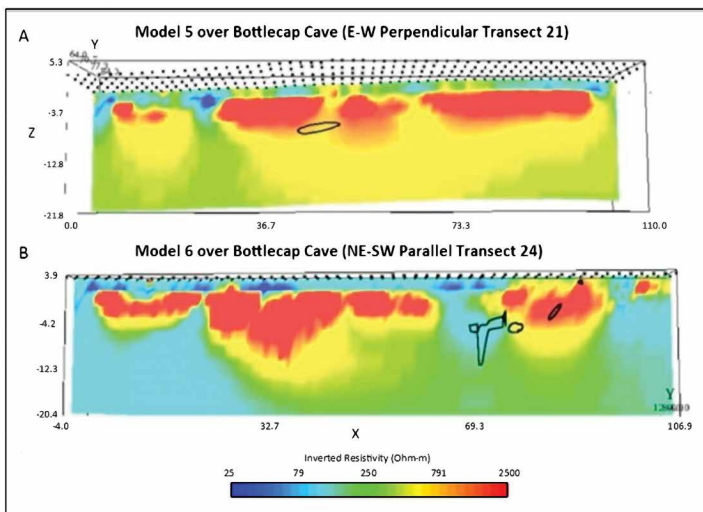


Figure 9. (a) Profile extracted from Model 5 over Bottlecave Cave (see Figure 8 for location). Black line shows projected geometry of Bottlecave Cave under T21. Contour interval ranging from 25–2,500  $\Omega\text{m}$ ; (b) Profile extracted from Model 6 over Bottlecave Cave (see Figure 8 for location). Black line shows projected geometry of Bottlecave Cave under T21. Contour interval ranging from 25–2,500  $\Omega\text{m}$ .

Figure 10a shows a resistivity low just north of the limestone quarry pit, which could possibly indicate an out-of-plane effect of the water-filled pit. An isolated resistivity high coincides with limestone outcrops. The northernmost extent of Legend Cave is not apparent in the eastern edge of the resistivity grid, presumably due to lack of depth resolution at the edge of the grid.

Taken together, the seven 3D Dipole-Dipole Models showed some correlations between resistivity highs and the sites of the two known cave systems. Bottlecave Cave, with depths centered approximately 8.5 meters below land surface, generally coincides with resistivity highs as seen in Figure 10b. Legend Cave, 3 meters to 9 meters below datum, conforms generally in length and depth with resistivity highs in the block model that is aligned with the cave (Fig. 10c), but there are significant mismatches in details of the shapes of the voids (Fig. 10b).

There are numerous zones of high resistivity in the inversions that are similar in size, shape, and depth of the two known cave systems at the site (Figs. 10b-c). The resistivity data suggest that significant unmapped void features may

T35, Model 6 trending in an NE–SW direction, and parallel to Bottlecave Cave (Fig. 9b). The first block, labeled Model 5 in Figure 9a, was created from E–W electrode arrays set at an angle of  $\sim 60$  degrees to the long axis of Bottlecave Cave. In the second block, labeled as Model 6 in Figure 9b, the NE–SW electrode arrays are set more closely parallel, at an angle of  $\sim 20$  degrees to the long axis of Bottlecave Cave (Fig. 10).

The results are inconclusive, as neither dataset showed agreement with the mapped cave passage location. In Model 6, we note an increase in resistivity corresponding with the entrance to Bottlecave Cave; however, where a vertical increase in the cave height exists, a discontinuity and low resistivity response are observed. Similarly, in Model 5, the known cave feature lies below a zone of resistivity highs. We note that Transect 24 is off-line from the center of Bottlecave Cave and that the cave passages consist of small diameters and highly complex morphology.

Comparatively, we note that on the 3D models discussed below there is generally better resolution of Legend Cave from profiles that are more closely parallel to the cave than there is for Bottlecave Cave, where profiles are more oblique to the centerline of the cave.

Analysis of cross-over points and model statistics of the resistivity values show a higher increase in resistivity over cave areas in the E–W transects than in the N–S transects. At crossings, perpendicular transects may show significantly different resistivities for the same material at similar depths. These cross-over errors range from 50  $\Omega\text{m}$  to 8,000  $\Omega\text{m}$  and indicate that the uncertainties associated with the resistivity values derived from the 2D transects are quite large in this highly variable 3D environment. This high variability illustrates the inherent geomorphologic heterogeneity and structural complexity of this karst landscape.

### 3D Block Models

In total, seven 3D block models were generated and then terrain corrected (Fig. 8). Three of the models shown here were derived from the Dipole-Dipole array and inverted using the Smooth inversion method (Fig. 8). A large increase in resistivity was observed on the north side of Legend Cave, which is cut off by roof collapse.

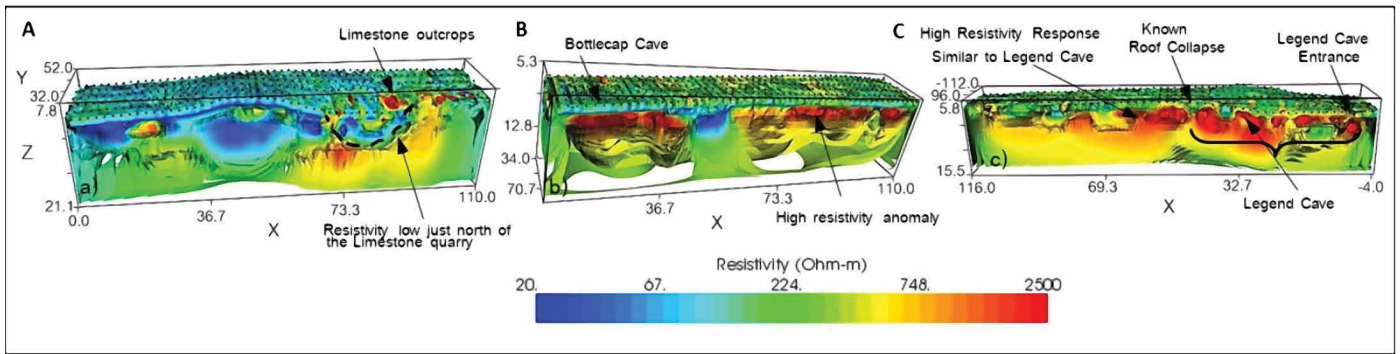


Figure 10. (a) A view of Model 3 facing North. See orange box on Figure 8 for location. Note the resistivity low that appears just north of the edge of the limestone quarry pit; (b) A view of Model 5 facing North. See green box on Figure 3b for location. Note the multiple high resistivity anomalies extending further to the north at the northeast portion of the study area and Bottlecap Cave to the west; (c) A view of Model 7 facing East. See the red box on Figure 3b for location. Note the cross-sectional view of Legend Cave which conforms well with the known cave length. A large increase in resistivity was observed on the north side of Legend Cave which is cut off by roof collapse.

exist, particularly to the north of Legend Cave (Fig. 10c). The presence of additional caves at similar elevations and in close proximity to one another can be expected in west-central Florida. The Dames Caves complex, located only one kilometer east of the study area, consists of several isolated caves within a few tens of meters of each other. From previous research, it appears that other shallow voids do indeed exist in the Brooksville Ridge area and elsewhere, often occurring as near-surface water table features that may have formed without entrances until subsequent sea level drop allowed their breach (Florea et al., 2007; Gulley et al., 2013).

**3D Visualization**  
**3D Site Model**

Additional software is necessary to simultaneously present the 3D resistivity data and the cave geometries. The combined site model was compiled from each of the 3D block models and then imported into Voxler 3D. A relatively high range in resistivity was observed across the study area and ranged from tens to thousands of  $\Omega\text{m}$ . Analysis of the ERT

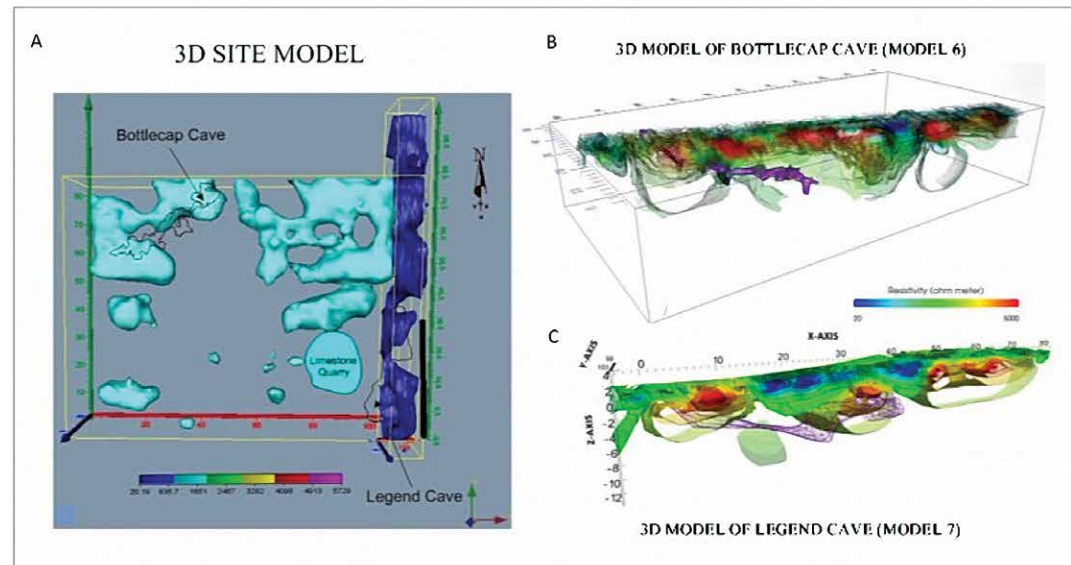


Figure 11. (a) A plan view of the 3D isosurface site model, contoured at  $375 \Omega\text{m}$  in dark blue and  $2,000 \Omega\text{m}$  in light blue. (Note the lower range in resistivity in the N-S oriented transect lines when compared to the higher resistivity range in the E-W transects); (b) shows a 3D view of Bottlecap Cave (Model 6) facing southeast. Model 6 indicates some correlation with high resistivities at the cave entrance. The deeper extent of the cave lies in a portion of the resistivity volume in which resistivities vary quite smoothly, and few iso-contours exist; (c) shows a 3D view of Legend Cave (Model 7) facing west which shows good correlation with the two larger rooms and no detection of the smaller connecting passage way.

Previous studies also noted poor results using the iso-surface plot (Chambers et al., 2012), revealing a significant limitation with this method for large scale use. A significant loss in 3D structure and resolution has also been previously noted when combining smaller subdomains (Rucker et al., 2009).

data along with the use of cross-over plots conducted for known cave locations indicates that the  $375 \Omega\text{m}$  contour conforms most closely to the known Legend Cave location and the  $2,000 \Omega\text{m}$  corresponds most closely to the known Bottlecap Cave location (Fig. 11a). This difference conforms to the previous observation that E-W surveys tend to show higher resistivities at cross-over points. This iso-surface plot from the 3D site model suggests potential voids at many locations and various depths, but it shows poor resolution of the mapped 3D structures.



### 3D Cave Models

To make 3D visual comparisons between the quasi-3D ERT data with the 3D cave models, we used Paraview to render an isosurface map of the resistivity data exported from EarthImager 3D. A color map was applied using the data scales, values and range of resistivity across the site. The 3D cave models were then imported into Paraview and spatially referenced to align the cave mesh with the 3D resistivity contour model. Display settings were adjusted to allow for shading and wireframe rendering. Autodesk Maya was utilized to render the exported 3D models with more advanced features and image quality enhancements, such as lighting and transparency (Figs. 11b-c).

Figures 11b and 11c illustrate that some cave anomalies appeared interconnected where roof collapse was known and in other cases very tight passages were not detected at all. The two large northern rooms, which are connected by a small passage, are detected as one large anomaly. As seen in Figures 10b and 10c, several other highly resistive anomalies are also observed in the 3D block models, which are similar in resistivity, structure, and depth to the cave anomalies. As previously noted, these highly resistive features are suspected to be additional voids, which may suggest a series of cave passages that are not interconnected.

## DISCUSSION

Overall, the findings from the 3D block models and the 3D visualization illustrate the difficulties of imaging cave geometries in eogenetic karst settings that are highly heterogeneous geomorphologically. The mapped voids presented here are only moderately complex cave structures; however, surrounding subsurface geology, consisting of near-surface clays (low resistivity, underlain by siliceous limestone (medium to high resistivity) with potentially numerous unmapped and potentially sediment-filled voids (high resistivity) appears highly variable. Thus, high matrix porosity plus disconnected voids present complexities that are often difficult to resolve using 2D and 3D ERT imaging in shallow eogenetic karst areas. Small interconnecting conduits within Legend Cave are not detected and, in some cases, large known cavities are exaggerated in size and shape. Relatively small cave features are increasingly difficult to detect with depth (Parise et al., 2015), as demonstrated for a synthetic sphere (van Nostrand and Cook, 1966). In this morphologically-diverse, eogenetic karst environment, higher data density, array geometries with higher resolution at depth, and multiple geophysical methods may clearly be desirable based on the results presented herein when attempting to detect shallow subsurface voids.

At this site, the lines in the E–W direction had a generally higher resistivity response than in the N–S direction. This could be indicative of an overall anisotropy in the resistivity, or of data sets acquired under different soil moisture conditions. However, the two elongated cave systems are not parallel, which does not indicate preferential orientation of voids at this site that would contribute to an overall anisotropy. Significantly different rainfall conditions were not noted at the time of acquisition of the N–S versus E–W trending profiles.

We also note that Legend Cave was better resolved, with lines directly overhead and in line with the cave's path, than Bottlecap Cave. The ability to resolve Bottlecap Cave significantly diminished at depth (Figure 10). This may have been a result of the slight off-set of the ERT transect lines overlying Bottlecap Cave, and highlights the importance of transect line orientation and the diminished resolvability of off-line features. Additionally, the Bottlecap Cave tablet shaped passage is significantly smaller than Legend Cave, which most likely resulted in the ERT's inability to detect the smaller cave passage. Lack of electrical current penetration at depth is particularly a problem in settings where conductive (low-resistivity) zones exist near the surface and concentrate current flow near the surface. Furthermore, with resistivity systems with a fixed number of electrodes, there is inherently a trade-off between line length, for greater depth penetration, and spatial resolution, which requires more closely spaced electrodes.

Studies have shown that water content at the time of ERT data collection can have an effect on the void resolution (Soupios et al., 2007). This is most closely related to seasonal changes in pore water during times of high and low rainfall that can influence the overall conductivity of the subsurface soils. For large scale surveys, we note that timely data collection may not always be possible. Water ponding in cave floors could make current flow pathways-and resistivity signals significantly more difficult to detect.

## CONCLUSIONS

Overall, we find that quasi-3D ERT for mapping air-filled caves in the vadose zone of eogenetic karst in west-central Florida is an improvement over simple 2D profiles, but suffers several limitations of the technology. Prior to surveying, the use of a synthetic model was highly beneficial for selecting the most appropriate array geometry. The Dipole-Dipole array was determined to be an effective array for identifying complex 3D structure with little added value by combining additional arrays and, while not part of this study, the addition of a strong-gradient array may work better to identify karst features. The EarthImager  $L_2$ -norm (Smooth) inversion method provided somewhat better results when compared against the  $L_1$ -norm (Robust). This is contrary to the results of other cave studies. We would recommend trying both inversions to determine the most appropriate inversion method at a given site. The orientation of transects should also

be a point of consideration as the best results in this case were obtained by profiles parallel to the strike of the cave. The 3D inversions should try to incorporate as many lines as possible in one block model (Rucker et al., 2009). This study was limited by computing access to invert the data in independent subsets. Possible use of an algorithm for faster 3D inversion of subsurface electrical resistivity data may also be beneficial in modeling larger data sets (Papadopoulos et al., 2011). In this study, line length was limited by site constraints, as clearly longer lines could have improved resolution at depth.

This study of Bottlecap and Legend Caves demonstrates the challenges of detecting the true 3D cave structure in highly variable eogenetic karst terranes. In this environment, a heterogeneous limestone with high matrix porosity and shallow cavities, the quasi-3D ERT approach was expected to provide a more accurate picture of subsurface resistivity than isolated 2D profiles. We found that 3D surveys indeed produced generally better agreement between resistivity anomalies and mapped cave locations than did isolated 2D lines. 3D visualization of the cave models indicated good resolution in the near-surface, with large cavities being detected, and diminished resolution with depth. However, a clear limitation of ERT for eogenetic karst terranes is the inability to detect smaller cavities and resolve their morphology, which may require the additional use of other geophysical methods and consideration of site-specific soil overburden and moisture conditions at the time of investigation.

## ACKNOWLEDGEMENTS

Special thanks to the University of South Florida's (USF) School of Geosciences, which facilitated a collaboration of multiple disciplines including geophysics, geology, speleology, geography and environmental science. We thank Rimkus Consulting Group, Inc. for use of their electrical resistivity survey equipment; the USF Alliance for Integrated Spatial Technologies for use of their geospatial lab; and the USF Advanced Visualization Center and Research Computing for their assistance with some of the 3D rendering and visualization images presented. Thanks to Kamal Humagain and Grant Harley for assistance with cave survey of Legend Cave and Robert Brooks for assistance with Bottlecap Cave survey. Special thanks to Withlacoochee State Forest for permits and access to the study sites.

## REFERENCES

- Abu-Shariah, Mohammed I.I., 2009, Determination of cave geometry by using a geoelectrical resistivity inverse model: *Engineering Geology*, v.105, p. 239–244. <https://doi.org/10.1016/j.enggeo.2009.02.006>
- ASTM, 1999, Standard Guide for using the Direct Current Resistivity Method for Subsurface Investigation D 6431-99.
- Brinkmann, R. and Reeder, P., 1994, The influence of sea-level change and geologic structures on cave development in west-central Florida: *Physical Geography* v. 16, no. 1, p. 52–61. Cardarelli, E., Cercato, M., Cerreto, A., and Di Filippo, G., 2010, Electrical resistivity and seismic refraction tomography to detect buried cavities: *Geophysical Prospecting*, v. 58, p. 685–695. <https://doi.org/10.1111/j.1365-2478.2009.00854.x>
- Catt, L.M.L., West, L.J., and Clark, R.A., 2009, The use of reference models from a priori data to guide 2D inversion of electrical tomography data: *Geophysical Prospecting*, v. 57, p. 1035–1048. <https://doi.org/10.1111/j.1365-2478.2008.00774.x>
- Chambers, J.E., Kuras, O., Meldrum, P.I., Ogilvy, R.D., Hollands, J., 2006, Electrical resistivity tomography applied to geologic, hydrogeologic, and engineering investigations at a former waste-disposal site: *Geophysics*, v. 71, no. 6, p. B231–B239. <https://doi.org/10.1190/1.2360184>
- Chambers, J.E., Wikinson, P.B., Wardrop, D., Hameed, A., Hill, I., Jeffrey, C., Loke, M.H., Meldrum, P.I., Kuras, O., Cave, M., and Gunn, D.A., 2012, Bedrock detection beneath river terrace deposits using three-dimensional electrical resistivity tomography: *Geomorphology*. <https://doi.org/10.1016/j.geomorph.2012.03.034>
- Crawford, N., 1989, The Karst Landscape of Warren County: Warren County Comprehensive Plan. Bowling Green. Special Report to the City-County Planning Commission of Warren County: p. 22–41.
- Crawford, N., Lewis, M., Winters, S., and Webster, J., 1999, Microgravity Techniques for Subsurface Investigations of Sinkhole Collapses and for Detection of Groundwater Flowpaths through Karst Aquifers, in *Beck, B.F., Pettit, A.J. and Herring, J.G., eds., Hydrology and Engineering Geology of Sinkholes and Karst*, Balkema, Rotterdam, 478 p.
- Dahlin, T. and Zhou, B., 2004, A numerical comparison of 2D resistivity imaging with 10 electrode arrays: *Geophysical Prospecting*, v. 52, p. 379–398. <https://doi.org/10.1111/j.1365-2478.2004.00423.x>
- Doll, W.E., Nyquist, J.E., Carpenter, P.J., Kaufmann, R.D., and Carr, B.J., 1998, Geophysical Surveys of a Known Karst Feature, Oak Ridge Y-12 Plant, Oak Ridge, Tennessee, *Environmental and Engineering Geophysics* 3, p. 133–146 (Accessed on July 14, 2010). <https://doi.org/10.2172/8046>
- El-Qady, G., Hafez, M., Abdalla, M.A., and Ushijima, K., 2005, Imaging Subsurface Cavities Using Geoelectric Tomography and Ground-Penetrating Radar: *Journal of Cave and Karst Studies*, v. 67, no. 3, p. 174–181.
- Ezersky M., 2008, Geoelectric structure of the Ein Gedi sinkhole occurrence site at the Dead Sea shore in Israel: *Journal of Applied Geophysics*, v. 64, p. 56–69. <https://doi.org/10.1016/j.jappgeo.2007.12.003>
- Florea, L., 2006, Architecture of air-filled caves within the karst of the Brooksville Ridge, west central Florida. *Journal of Cave and Karst Studies*, v. 2, no. 2, p. 64–75.
- Florea, L.J., and Vacher, H.L. 2006, Springflow Hydrographs: Eogenetic vs. Telogenetic Karst: *Groundwater*, v. 44, no. 3, p. 352–361. <https://doi.org/10.1111/j.1745-6584.2005.00158.x>
- Florea, L.J., Vacher, H.L., Donahue, B., and Naar, D., 2007, Quaternary cave levels in peninsular Florida: *Quaternary Science Reviews*, v. 26: p. 1344–1361. <https://doi.org/10.1016/j.quascirev.2007.02.011>
- Florida Geological Survey, 2010, Florida Rocks and Minerals: [http://www.dep.state.fl.us/geology/geologictopics/rocks/florida\\_rocks.htm#Rocks%20of%20Florida](http://www.dep.state.fl.us/geology/geologictopics/rocks/florida_rocks.htm#Rocks%20of%20Florida) (Accessed July, 29, 2010).
- Fu, Z., Ren, Z., Hua, X., Shi, Y., Chen, H., Chen, C., Li, Y., and Tang, J., 2020, Identification of underground water-bearing caves in noisy urban environments (Wuhan, China) using 3D electrical resistivity tomography techniques: *Journal of Applied Geophysics*, v. 174, <https://doi.org/10.1016/j.jappgeo.2020.103966>



- Gambetta, M., Armadillo, E., Carmisciano, C., Stefanelli, P., Cocchi, L., and Tontini, C., 2011. Determining geophysical properties of a near-surface cave through integrated microgravity vertical gradient and electrical resistivity tomography measurements: *Journal of Cave and Karst Studies*, v. 72, no. 1, p. 11–15. <https://doi.org/10.4311/jcks2009ex0091>
- Gary, M.O., Rucker, D.F., Smith, B.D., Smith, D.V. and Befus, K., 2013. Geophysical Investigations of the Edwards-Trinity Aquifer System at Multiple Scales: Interpreting Airborne and Direct-Current Resistivity in Karst: *Proceedings of the 13th Sinkhole Conference NCKRI Symposium 2*, p. 195–206.
- Gharibi, M. and Bentley, L., 2005. Resolution of 3-D Electrical Resistivity Images from Inversions of 2-D Orthogonal Lines: *Journal of Environmental and Engineering Geophysics*, v. 10, no. 4, p. 339–349. <https://doi.org/10.2113/JEEG10.4.339>
- Gibson, P.J., Lyle, P., and George, D.M., 2004. Applications of resistivity and magnetometry geophysical techniques for near-surface investigations in karstic terranes in Ireland. *Journal of Cave and Karst Studies*, v. 66, no. 2, p. 35–38.
- Gulley, J. D., Martin, J. B., Moore, P. J. and Murphy, J., 2013. Formation of phreatic caves in an eogenetic karst aquifer by CO<sub>2</sub> enrichment at lower water tables and subsequent flooding by sea level rise: *Earth Surface Processes and Landforms*, v. 38, p. 1210–1224. <https://doi.org/10.1002/esp.3358>
- Häuselmann, P. (ed.), 2010, *UIS Mapping Grades: Survey and Mapping Working Group, UIS Informatics Commission, Version 1*.
- Jackson, P.D., Earl, S.J., and Reece, G.J., 2001. 3D resistivity inversion using 2D measurements of the electric field: *Geophysical Prospecting*, v. 49, p. 26–39. <https://doi.org/10.1046/j.1365-2478.2001.00241.x>
- Jenson, J.W., Keel, T.M., Mylroie, J.R., Mylroie, J.E., Stafford, K.W., Taborosi, D., and Wexel, C., 2006. Karst of the Marian Islands: The interaction of tectonics, glacio-eustasy, and freshwater/seawater mixing in island carbonates, in Harmon, R.S., Wicks, C.M., Ford, D.C., and White, W.B. eds., *Perspectives on Karst Geomorphology, Hydrology, and Geochemistry: Geological Society of America, Special Paper 404*. [https://doi.org/10.1130/2006.2404\(11\)](https://doi.org/10.1130/2006.2404(11))
- Kambesis, P.N., Larson, E.B., Mylroie, J.E., 2015. Morphometric analysis of cave patterns using fractal indices, in Feinberg, J., Gao, Y., and Alexander, E.C., Jr., eds., *Caves and Karst Across Time: Geological Society of America Special Paper*, 516, p. 1–20. <https://doi.org/10.1130/SPE516>
- Kaufmann, G., Romanov, D., and Nielbock, R., 2011. Cave detection using multiple geophysical methods: Unicorn cave, Harz Mountains, Germany: *Geophysics*, v. 76, no. 3, p. B71–B77. <https://doi.org/10.1190/1.3560245>
- Kaufmann, O., Deceuster, J., and Quinif, Y., 2012. An electrical resistivity imaging-based strategy to enable site-scale planning over covered paleokarst features in the Tournaisis area (Belgium): *Engineering Geology*, v. 133–134, p. 49–65. <https://doi.org/10.1016/j.enggeo.2012.01.017>
- Kirk, G.K., 1981, *Handbook of geophysical cavity-locating techniques with emphasis on electrical resistivity*, U.S. Department of Transportation Federal Highway Administration, Environmental Exploration, U.S. Government Printing Office, HP, Morgantown, 175.
- Kruse, S., Grasmueck, M., Weiss, M., and Viggiano, D., 2006. Sinkhole structure imaging in covered Karst terrain: *Geophysical Research Letters*, v. 33: L16405. <https://doi.org/10.1029/2006GL026975>
- Lace, M. and Mylroie, M., 2013. Coastal Cave and Karst Resource Management, in Lace, M. and Mylroie, M., eds., *Coastal Karst Landforms*, v. 5, p. 127–143. [https://doi.org/10.1007/978-94-007-5016-6\\_6](https://doi.org/10.1007/978-94-007-5016-6_6)
- Land, L. and G. Veni, 2012, *Electrical resistivity surveys of anthropogenic karst phenomena, southeastern New Mexico*, New Mexico: *Geology*, v. 34, p. 117–125.
- Leucci G., Parise M., Sammarco M., and Scardozzi G., 2016, The use of geophysical prospections to map ancient hydraulic works: the Triglio underground aqueduct (Apulia, Southern Italy): *Archaeological Prospection*, v. 23, p. 195–211. <https://doi.org/10.1002/arp.1541>
- Loke, M.H. and Barker, R.D., 1996a, Rapid least-squares inversion of apparent resistivity pseudosections by a quasi-Newton method: *Geophysical Prospecting*, v. 44, p. 131–152. <https://doi.org/10.1111/j.1365-2478.1996.tb00142.x>
- Loke, M.H. and Barker, R.D., 1996b, Practical techniques for 3D resistivity surveys and data inversion: *Geophysical Prospecting*, v. 44, p. 499–523. <https://doi.org/10.1111/j.1365-2478.1996.tb00162.x>
- Loke, M.H., Chambers, J.E., Rucker, D.F., Kuras, O. and Wilkinson, P.B., 2013, Recent developments in the direct-current geoelectrical imaging method: *Journal of Applied Geophysics*, v. 95, p. 135–156. <https://doi.org/10.1016/j.jappgeo.2013.02.017>
- Majzoub, A.F., Stafford, K.W., Brown, W.A., and Ehrhart, J.T., 2017, Characterization and delineation of gypsum karst geohazards using 2D electrical resistivity tomography in Culberson County, Texas, USA: *Journal of Environmental and Engineering Geophysics*, v. 22, p. 411–420. <https://doi.org/10.2113/JEEG22.4.411>
- Martorana, R., Fiandaca, G., Casas Ponsati, A., and Cosentino, P.L., 2009, Comparative tests on different multi-electrode arrays using models in near-surface geophysics: *Journal of Geophysics and Engineering*, v. 6, p. 1–20. <https://doi.org/10.1088/1742-2132/6/1/001>
- Margiotta S., Negri S., Parise M., and Valloni R., 2012, Mapping the susceptibility to sinkholes in coastal areas, based on stratigraphy, geomorphology and geophysics: *Natural Hazards*, v. 62, no. 2, p. 657–676. <https://doi.org/10.1007/s11069-012-0100-1>
- McCormack, T., O'Connell, Y., Daly, E., Gill, L.W., Henry, T., and Perriquet, M., 2017, Characterisation of karst hydrogeology in Western Ireland using geophysical and hydraulic modelling techniques: *Journal of Hydrology: Regional Studies*, v. 10, p. 1–17. <https://doi.org/10.1016/j.ejrh.2016.12.083>
- Miller, Benjamin V., 2010, *Cave map of Bottlecage Cave, Citrus County, Florida*, unpublished, Florida Speleological Survey.
- Mohamed, A.M.E., El-Hussain, I., Deif, A., Araffa, S.A.S., Mansour, K., and Al-Rawas, G., 2019, Integrated ground penetrating radar, electrical resistivity tomography and multichannel analysis of surface waves for detecting near-surface caverns at Duqm area, Sultanate of Oman: *Near Surface Geophysics*, v. 17. <https://doi.org/10.1002/nsg.12054>
- Nasserri-Moghaddam, A., Cascante, G., and Hutchinson, J., 2005, A New Quantitative Procedure to Determine the Location and Embedment Depth of a Void Using Surface Waves: *Journal of Environmental and Engineering Geophysics*, v. 10, no. 1, p. 51–64. <https://doi.org/10.2113/JEEG10.1.51>
- Nazaruddin, D. A., Amiruzan, Z. S., Hussin, H., & Jafar, M. T. M., 2017, Integrated geological and multi-electrode resistivity surveys for ground-water investigation in Kampung Rahmat village and its vicinity, Jeli district, Kelantan, Malaysia: *Journal of Applied Geophysics*, v. 138, p. 23–32. <https://doi.org/10.1016/j.jappgeo.2017.01.012>
- Neyamandpour, A., Taib, S., and Wan Absullah, W.A.T., 2009, An Application of Three-Dimensional Electrical Resistivity Imaging for the Detection of an Underground Waste-Water System: *Studia Geophysica et Geodaetica*, v. 53, p. 389–402. <https://doi.org/10.1007/s11200-009-0027-5>
- Neyamandpour, A., Wan Absullah, W.A.T., Taib, S., and Neyamandpour, B., 2010, Comparison of Wenner and dipole-dipole arrays in the study of an underground three-dimensional cavity. *Journal of Geophysics and Engineering*, v. 7, p. 30–40. <https://doi.org/10.1088/1742-2132/7/1/003>
- Palmer, A.N., 2007, *Cave Geology*, Dayton, Ohio: Cave Books.
- Pánek T., Margielewski, W., Taborik, P., Urban, J., Hradecky, J., and Szura, C., 2010, Gravitationally induced caves and other discontinuities detected by 2D electrical resistivity tomography: Case studies from the Polish Flysch Carpathians: *Geomorphology*, v. 123, p. 165–180. <https://doi.org/10.1016/j.geomorph.2010.07.008>

- Papadopoulos, N.G., Tsourlos, P., Tsokas, G.N., and Sarris, A., 2006, Two-dimensional and Three-dimensional Resistivity Imaging in Archeological Site Investigation: *Archaeological Prospection*, v. 13, p. 163–181. <https://doi.org/10.1002/arp.276>
- Papadopoulos, N.G., Yi, M., Kim, J., Tsourlos, P., and Tsokas, G. N., 2010, Geophysical investigation of tumuli by means of surface 3D Electrical Resistivity Tomography: *Journal of Applied Geophysics*, v. 70, p. 192–205. <https://doi.org/10.1016/j.jappgeo.2009.12.001>
- Pánek, T., Margielewski, W., Taborik, P., Urban, J., Hradecky, J., and Szura, C., 2010, Gravitationally induced caves and other discontinuities detected by 2D electrical resistivity tomography: Case studies from the Polish Flysch Carpathians. *Geomorphology*, v. 123, p. 165–180. <https://doi.org/10.1016/j.geomorph.2010.07.008>
- Parise, M., and Gunn, J., (eds.), 2007, *Natural and anthropogenic hazards in karst areas: Recognition, Analysis and Mitigation*: Geological Society London, sp. publ. 279. <https://doi.org/10.1144/SP279.1>
- Parise M., Closson D., Gutierrez F., and Stevanovic Z., 2015, Anticipating and managing engineering problems in the complex karst environment: *Environmental Earth Sciences*, v. 74, 7823–7835. <https://doi.org/10.1007/s12665-015-4647-5>
- Polk, J.S., 2009, *Proxy Records of Climate Change in Subtropical and Tropical Karst Environments*, [Ph.D. Dissertation]: Tampa, University of South Florida.
- Polk, J.S., 2012, Legend Cave Map, unpublished, Withlacoochee State Forest, Citrus, County, Florida.
- Polk, J.S., van Beynen, P.E., and Wynn, J.G., 2012, An Isotopic Calibration Study of Precipitation, Cave Dripwater, and Climate in West-central Florida: *Hydrological Processes*. <https://doi.org/10.1002/hyp.8169>
- Prins, C., Thuro, K., Krautblatter, M., Schulz, R., 2019, Testing the effectiveness of an inverse Wenner-Schlumberger array for geoelectrical karst void reconnaissance, on the Swabian Alb high plain, new line Wendlingen–Ulm, southwestern Germany: *Engineering Geology*, v. 249, p. 71–76. <https://doi.org/10.1016/j.enggeo.2018.12.014>
- Redhaouia, B., Ilondo, B. O., Gabtni, H., Sami, K., and Bédir, M., 2016, Electrical Resistivity Tomography (ERT) applied to Karst carbonate aquifers: case study from Amdoun, northwestern Tunisia: *Pure and Applied Geophysics*, v. 173, no. 4, 1289–1303. <https://doi.org/10.1007/s00024-015-1173-z>
- Redhaouia, B., Bédir, M., Gabtni, H., Batobo, O. I., Dhaoui, M., Chabaane, A., and Khomsi, S., 2016, Hydro-geophysical characterization for groundwater resources potential of fractured limestone reservoirs in Amdoun Monts (North-western Tunisia): *Journal of Applied Geophysics*, v. 128, 150–162. <https://doi.org/10.1016/j.jappgeo.2016.03.005>
- Roth, M.J.S., Mackey, J.R., Mackey, C., and Nyquist, J.E., 2002, A case study of the reliability of the multielectrode earth resistivity testing for geotechnical investigations in karst terrains: *Engineering Geology*, v. 65, p. 225–232. [https://doi.org/10.1016/S0013-7952\(01\)00132-6](https://doi.org/10.1016/S0013-7952(01)00132-6)
- Rucker, D.F., Levitt, M.T., and Greenwood, W.J., 2009, Three-dimensional electrical resistivity model of a nuclear waste disposal site: *Journal of Applied Geophysics*, v. 69, p. 150–164. <https://doi.org/10.1016/j.jappgeo.2009.09.001>
- Schoor, M.V., 2002, Detection of sinkholes using 2D electrical resistivity imaging: *Journal of Applied Geophysics*, no.50, p. 393–399. [https://doi.org/10.1016/S0926-9851\(02\)00166-0](https://doi.org/10.1016/S0926-9851(02)00166-0)
- Schrott, L., and Sass, O., 2008, Application of field geophysics in geomorphology: Advances and limitations exemplified by case studies: *Geomorphology*, v. 93, p. 55–73.
- Scott, T.M., 1997, Miocene to Holocene History of Florida. In: Randazzo, A.F., Jones, D.S. (Ed.) *The Geology of Florida*, University Press of Florida, Gainesville, p. 57–67. <https://doi.org/10.1016/j.geomorph.2006.12.024>
- Scott, T.M., 2001, *The Geologic Map of Florida*: Florida Geological Survey Report 80.
- Sheehan, J.R., Doll, W.E., and Watson, D.B., 2005, Detecting Cavities with Seismic Refraction Tomography: Can it be done? Extended abstract, presented at the 2005 Annual Meeting of the Symposium on the Application of Geophysics to Engineering and Environmental Problems, Atlanta, GA, April 307, 2005. <https://doi.org/10.4133/1.2923557>
- Sinclair, W.C., Stewart, J.W., Knutilla, R.L., Gilboay, A. E., and Miller, R.L., 1985, Types, Features, and Occurrence of Sinkholes in the Karst of West-central Florida: US Geological Survey, Water Resources Investigations Report, 85-4126.
- Soupios, P.M., Georgakopoulos, P., Papadopoulos, N., Saltas, V., Andreadakis, A., Vallianatos, F., Sarris, A., and Makris, J.P., 2007, Use of engineering geophysics to investigate a site for a building foundation: *Journal of Geophysics and Engineering*, v. 4, p. 94–103. <https://doi.org/10.1088/1742-2132/4/1/011>
- Southwest Florida Water Management District, 2006, Lidar data acquired from <http://www.swfwmd.state.fl.us/data/>
- Sumanovac, F and Weisser, M., 2001, Evaluation of resistivity and seismic methods for hydrogeological mapping in karst terrains: *Journal of Applied Geophysics*, v.47, p. 13–28. [https://doi.org/10.1016/S0926-9851\(01\)00044-1](https://doi.org/10.1016/S0926-9851(01)00044-1)
- Torrese, P., 2020, Investigating karst aquifers: Using pseudo 3-D electrical resistivity tomography to identify major karst features: *Journal of Hydrology*, v. 580. <https://doi.org/10.1016/j.jhydrol.2019.124257>
- Vacher, L. and Mylroie, J., 2002, Eogenetic Karst from the Perspective of an Equivalent Porous Medium: *Carbonates and Evaporites*, v.17, no. 2, p. 182–196. <https://doi.org/10.1007/BF03176484>
- Van Nostrand, R.G. and Cook, K.L., 1966, *Interpretation of Resistivity Data*: Geological Survey Professional Paper 499. United States Government Printing Office, Washington. <https://doi.org/10.3133/pp499>
- Wilkinson, P.B., Chambers, J. E., Meldrum, P.I., Ogilvy, R.D., Mellor, C.J., and Caunt, S., 2005, A Comparison of Self-Potential Tomography with Electrical Resistivity Tomography for the Detection of Abandoned Mineshafts: *Journal of Environmental and Engineering Geophysics*, v.10, no. 4, p. 381–389. <https://doi.org/10.2113/JEEG10.4.381>
- Xia, J. and Miller, R.D., 2007, Integrated geophysical survey in defining subsidence on a golf course: *Journal of Geophysics and Engineering*, v.4, p. 443–451. <https://doi.org/10.1088/1742-2132/4/4/010>
- Zhou, W. and Beck B.F., 2011, Engineering issues on karst: In: P. van Beynen (Ed), *Karst Management*. Springer, Dordrecht, p. 9–45. [https://doi.org/10.1007/978-94-007-1207-2\\_2](https://doi.org/10.1007/978-94-007-1207-2_2)
- Zhu, J., Currens, J. C. and Dinger, J. S., 2011, Challenges of using electrical resistivity method to locate karst conduits-A field case in the Inner Bluegrass Region, Kentucky: *Journal of Applied Geophysics*, v.75, p. 523–530. <https://doi.org/10.1016/j.jappgeo.2011.08.009>

## GEOLOGY AND PALAEOENVIRONMENT OF KARIN TAK CAVE (LESSER CAUCASUS)

Avagyan Ara<sup>1\*</sup>, Sahakyan Lilit H.<sup>1</sup>, Igityan Hayk<sup>1</sup>, Gevorgyan Mikayel<sup>1</sup>, Sahakyan Kristina<sup>1</sup>, Antonosyan Maria<sup>2</sup>, Tepanosyan Gevorg<sup>3</sup>, Sahakyan Lilit V.<sup>3</sup>, Atalyan Tatul<sup>1</sup>, Grigoryan Taron<sup>1</sup>, Aspaturyan Narek<sup>4</sup>, Avagyan Seda<sup>1</sup>, and Yepiskoposyan Levon<sup>5</sup>

---

### Abstract

Karin Tak cave is located in the south-eastern end of the Lesser Caucasus (NE of the Armenian Highland). Development of the cave was related to the dissolution of Middle-Upper Jurassic limestone by meteoric water recharge controlled by pre-existing faults and fissures beginning in the Neogene. Geophysical studies of the cave, including by ground penetrating radar, have been conducted, and a map of the pit's walls constructed showing the extent of the roof collapse breccia and of sediment deposits on the cave floor. The collapse material consists of chaotic limestone breccia and blocks. Careful analysis of cave floor sediments allowed the Late Pleistocene palaeoenvironment in the vicinity of the cave to be reconstructed. Analyses included integrated sedimentological studies (stratigraphy, grain size analysis) together with geochemical (X-ray fluorescence) and palynological observations. Pollen studies indicate the dominance of conifers (>60 % *Tsuga sp.*, *Pinus sp.*) together with *Fraxinus sp.* (fam. *Oleaceae*) and *Quercus sp.* (fam. *Fagaceae*), which indicate a cold temperate continental climate in the Late Pleistocene. Non-dramatic climate change occurred during the Last Glacial Maximum (LGM) in the cave area, with conditions favorable for hominin activity.

---

### INTRODUCTION

The Lesser Caucasus is part of the geologically active Alpine-Himalayan orogenic belt and is composed of a variety of different types of magmatic, metamorphic, and sedimentary rocks including remnant oceanic crust. Sedimentary rocks include thick carbonates of Jurassic-Cretaceous age (e.g., Shikhaylibeli et al., 1994) that have been karstified in places as a result of subaerial exposure with the development of karst landforms and cave systems. One such karst cave occurs at Karin Tak in the SE-most Lesser Caucasus (NE Armenian Highland: Fig. 1) where a Late Pleistocene to Holocene sediment infill has been found to contain well-preserved hominin remains and obsidian tools together with faunal and floral remnants (Stafford and Yepiskoposyan, 2015; Antonosyan, et al., 2019). The importance of the cave derives from the fact that it is located on an established migration route used by hominins (e.g., Adler et al., 2014; Fernández-Jalvo et al., 2016). During the Last Glacial Maximum (LGM), corresponding to MIS 2 (Marine Isotope Stage) (26,500–19,000 calibrated years before present (cal. BP) by Clark et al., 2009) led to ecological restructuring, species redistribution and extinctions (Provan and Bennett, 2008) the Great Caucasus served as climatic buffer for southern areas. Additionally, the ameliorating effects of the Black and Caspian Seas favored the Lesser Caucasus as a biogeographical refugium throughout the Pleistocene (e.g., Gabunia et al., 2000; Bar-Yosef et al., 2011; Fernández-Jalvo et al., 2016).

Cave infilling sediments reflect the geomorphological, climatic, and biological setting of the karst systems, and provide a long-term record of past environments and possible human activity. Sediments at depths of about 0.5 m below the present-day Karin Tak cave floor surface contain evidence from obsidian tools bracketed with <sup>14</sup>C-dated animal bones that the site was inhabited by early humans from at least 42,000 years ago (Stafford and Yepiskoposyan, 2015). The Paleolithic occupations are well-documented in Aghitu-3 Cave (around 65 km WSW from Karin Tak cave) occurred between 36 and 32 ka cal BP and between 29 and 24 ka cal BP (Bertacchi et al., 2020).

The environmental and other conditions of the cave are optimal for the preservation of biomolecules, potentially allowing genomic reconstructions to be made of the prehistoric ecosystem of the region. A human tooth found in the Karin Tak cave is dated to ca. 6900 years BP yielded high-quality ancient DNA (aDNA) and indicated genetic continuity of the population inhabiting the Armenian Highlands since at least the Neolithic (Margaryan et al., 2017).

Excellent aDNA preservation allowed successful species identification and has improved Late Pleistocene palaeoenvironmental reconstructions for the region (e.g., Antonosyan et al., 2019; Bertacchi et al. 2020). Genetic screening of the bones has indicated a high faunal diversity between ca. >42,000 and 24,803 cal BP. A total of 27 different taxa, represented by 11 mammalian and three avian families were identified (Antonosyan et al., 2019). The genetically recovered tax-

---

<sup>1</sup>Institute of Geological Sciences, National Academy of Sciences of Republic of Armenia (NAS RA), 24a M. Baghramyan ave., Yerevan 0019, Armenia

<sup>2</sup>Russian-Armenian University, 123 Hovsep Emin St, Yerevan 0033, Armenia

<sup>3</sup>Center for Ecological-Noosphere Studies, NAS RA, 68 Abovyan St., Yerevan 0025, Armenia

<sup>4</sup>Yerevan State University, 1 Manukyan St., Yerevan, 0025, Armenia,

<sup>5</sup>Institute of Molecular Biology, NAS RA, 7 Hasratyan St., Yerevan 0014, Armenia

\* Corresponding author: avagn1064@gmail.com

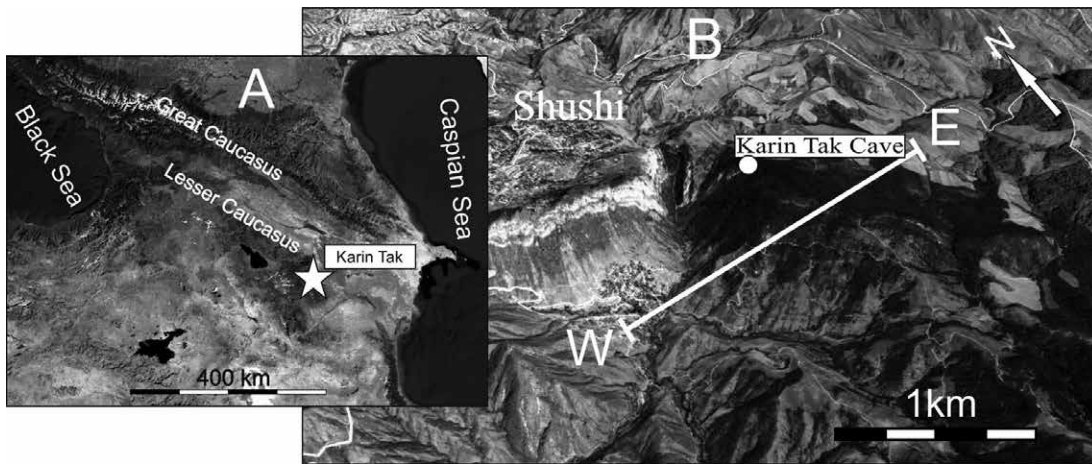


Figure 1. (A) Geographic location of Karin Tak Cave in the Lesser Caucasus (SE part of Armenian Highland), (B) Situation of Karin Tak cave on the Google Satellite 3D Image. SW-NE cross section for schematic model of cave development (Figure 14).

onomic composition rich and diverse and consists predominantly of extant wild mammalian and avian taxa, together with species that are regionally extinct (including *Gazella subgutturosa*, *Ursus tibetanus*, *Crocota crocuta* and *Mesocricetus raddei*). Overall, the results of the fossil taxonomy indicate the continuity of the faunal composition of the region throughout the Late Pleistocene. It seems, therefore, that the cold and arid conditions during MIS 2 did not cause a change in faunal

Pleistocene. It seems, therefore, that the cold and arid conditions during MIS 2 did not cause a change in faunal

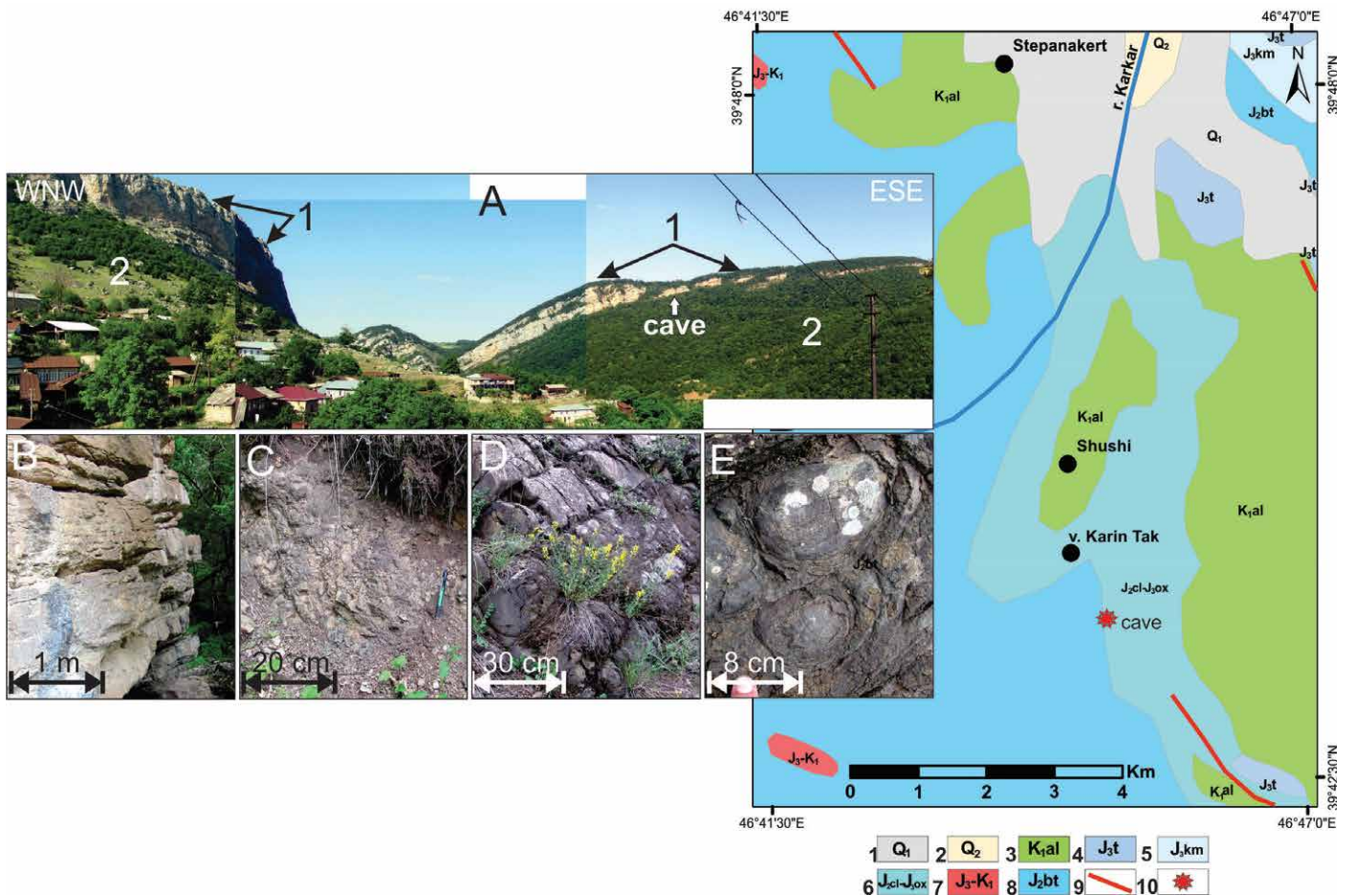


Figure 2. (A) Field photography of Karin Tak cave, (B) Middle and Upper Jurassic (Callovian-Oxfordian) thickly bedded limestones, (C-E) Middle Jurassic, Bathonian sedimentary rocks, (C) volcanic breccias, (D) siltstones, (E) volcanic formations of on-ion-skin weathering. Simplified geological map of the area. 1. Modern sediments, 2. Lower Quaternary sediments, 3. Lower Cretaceous (Albian) pyroclastic rocks, 4. Upper Jurassic (Tithonian) limestones, 5. Upper Jurassic (Kimmeridgian) organogenic-detrital, pelitomorphic, sandy limestones with volcano-sedimentary lenses of small thicknesses, 6. Middle Jurassic (Callovian), Upper Jurassic (Oxfordian) limestones, 7. Upper Jurassic-Lower Cretaceous quartz-diorites, 8. Middle Jurassic volcanic, pyroclastic, volcanosedimentary rocks, 9. Faults, 10. The locality of Karin Tak cave

composition. During that time span, Karin Tak cave was located at the boundary between arid subtropical and humid climate regions (with the latter supporting forests), a pattern similar to the present-day setting of the site (Antonosyan et al., 2019).

The previous results also indicate that Karin Tak cave should be considered as a regionally important site from which viable molecular data can be obtained. These data will allow the reconstruction of the Late Pleistocene ecosystem in the Lesser Caucasus, and will give new insights into the early human occupation and biodiversity of the region.

The principal aims of this paper are therefore to: (i) describe the formation of Karin Tak cave in terms of geological processes; (ii) report on the depth and spatial dimensions of soft sediments in the cave on the basis of geophysical surveys to determine strategies for future excavation; and (iii) present the results of sedimentological, X-ray diffraction, geochemical, and palynological studies of the cave floor sediments to investigate depositional processes and to reconstruct the paleoenvironmental record of the site.

### Geological setting of the cave

Karin Tak cave (39°44'35.23" N, 46°45'58.47" E, 1405 masl) is located on the East bank of the Karkar river and is named after a nearby village (Figs. 1, 2). The cave is about 60 m long containing at least six chambers, and is in general oriented NE-SW (Fig. 3). The cave has formed in thickly-bedded Callovian to Oxfordian (Middle-Upper Jurassic) limestones (Shikhaylibeli et al., 1994) that outcrop in the area (Fig. 2, A–B). These limestones typically display grainstone (occasionally packstone) texture and in some places silicification is evident. The bedrock strata dip approximately 18° towards NE near the cave.

The limestones unconformably overlie the Middle Jurassic (Bathonian) volcanoclastic (Fig. 2, C–D), sedimentary and volcanic rocks. The outcropping porphyric basalts display onion skin weathering in places (Fig. 2, E). The Bathonian rocks have a strike of N138°–N142° and dip between 29°–51° NE, which is markedly steeper than the overlying limestones.

In terms of the regional geological structure, the SE Lesser Caucasus is located in an area that underwent intense compression and uplift during the Neogene as a result of convergence between the Arabian Plate and the South Armenian block or microplate (e.g., Avagyan et al., 2010; Sosson et al., 2010). The regression of the Sarmatian sea occurred and continental conditions were initiated in the late Messinian in the Ararat depression to the south of the Lesser Caucasus as a result of Late Miocene tectonic activity and uplift (Gabrielyan et al., 1981; Avagyan et al., 2018).

Middle-Upper Jurassic limestones were probably exposed subaerially at this time and have subsequently undergone karstification. Near-surface caves developed along pre-existing fractures and faults due to meteoric dissolution of the host rock. We suggest that the development of the Karin Tak was initiated during this period.

### MATERIALS AND METHODS

Karin Tak cave was studied using conventional geological and structural mapping techniques. Two- and three-dimensional ground penetrating radar surveys were conducted in the cave. An SIR-3000 (USA, 2008) GPR system with a 400 MHz antenna was used, enabling a survey to be made to depths of up to 3 m.

Pit excavations were used to investigate the cave floor sediments. Six sediment layers were identified in the SE and SW walls of the excavated pit in the cave. Sediments were categorized by particle size, texture, and fabric using White's

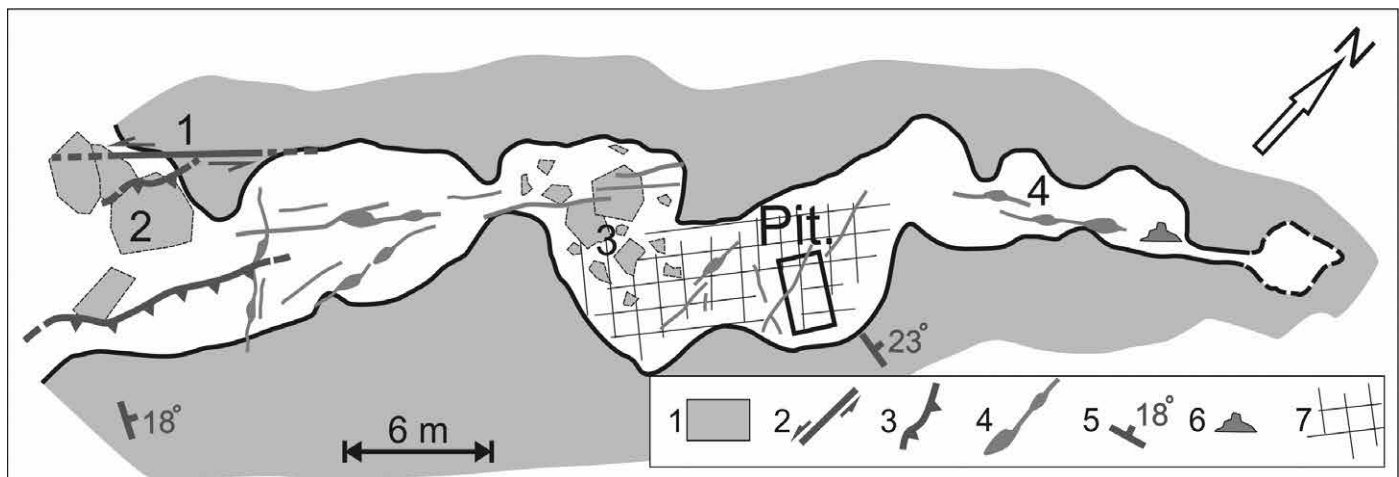


Figure 3. The plan of Karin Tak cave with observed structures. The location of the pit is indicated. 1. Limestones; 2. Strike-slip fault; 3. Reverse faults; 4. Fractures and vertical shafts; 5. Limestone dip; 6. Stalagmites; 7. Profile lines of the geophysical survey.



classification (White, 2007). The Munsell color chart system (<https://munsell.com/>) has been used to define the colors of cave sediments.

The immersion method was used to study the mineralogical content of samples from A–D layers. One hundred grams of sample from each layer were separated into light and heavy fractions by Bromoform liquid. The minerals were studied using liquids of N 1,490 (for light fraction) and 1,530 (for heavy fraction) refractive indexes. For pollen analysis, 10 mL of each dry sediment sample was processed following the method of Grichuk and Zaklinskaya (1948) with the following steps: first adding 20 mL 10 % HCl to each sample with 10 minutes in a hot water bath. Second is adding 20 mL 10 % KOH, 20 minutes in the hot water bath, and the last step is heavy liquid flotation, which contains KJ and CDJ<sub>2</sub>. Each step is followed by flushing with distilled water, centrifuging 12 minutes at 3000 rpm in a swing rotor centrifuge and carefully decanting the liquid.

Eleven samples were studied using a conventional light microscope. Nine samples were collected from the cave pit for spectrometry analysis, together with one chert sample. The samples were air-dried, homogenized, sieved (<2 mm), milled in compliance with ISO-11464 (ISO, 2006) and then stored in sealed bags. The cave sediment samples were analyzed by X-ray fluorescence spectrometry using an Olympus Innov-X-5000 (USA) apparatus following EPA standard 6200 (US EPA, 2007) in the Center for Ecological-Noosphere Studies (CENS, Armenia). The XRF was equipped with a Ta X-ray tube that allowed the determination of elements (Cr, V, Ti, Mo, Zr, Sr, Rb, As, Zn, Cu, Co, Fe, Mn, Pb and Ba) in 3-beam soil mode. Beam time was 120 seconds. Detailed quality assurance and quality control (QA/QC) was carried out using standard reference materials (National Institute of Standards and Technology 2711a and NIST 2710a, USA), a blank (SiO<sub>2</sub>) obtained from the NIST(USA), as well as lab duplicates. QA/QC showed that the accuracy and precision of the analyses were 2.2–15.4 % and 0.1–6.9 %, respectively. Values below detection limits (BDL) were observed for Mo. Considering the relatively low number of BDL records (<15 % of all samples) (Johnson et al., 2011; Rothwell, and Croudace 2015) element concentrations BDL are given a value of one-half of the detection limit.

## RESULTS

### Structural features

The general orientation of Karin Tak cave (N 46°) is controlled by the dominant system of regional fractures which trend N 40°–N 55° (Fig. 3). The presence of sinkholes on the surface of the surrounding limestone plateau and of numerous well-developed vertical shafts in the cave indicate intense circulation of meteoric groundwater with the leeching and dissolution of the limestone host rock. Most of the shafts in the cave have developed along fractures and are oval

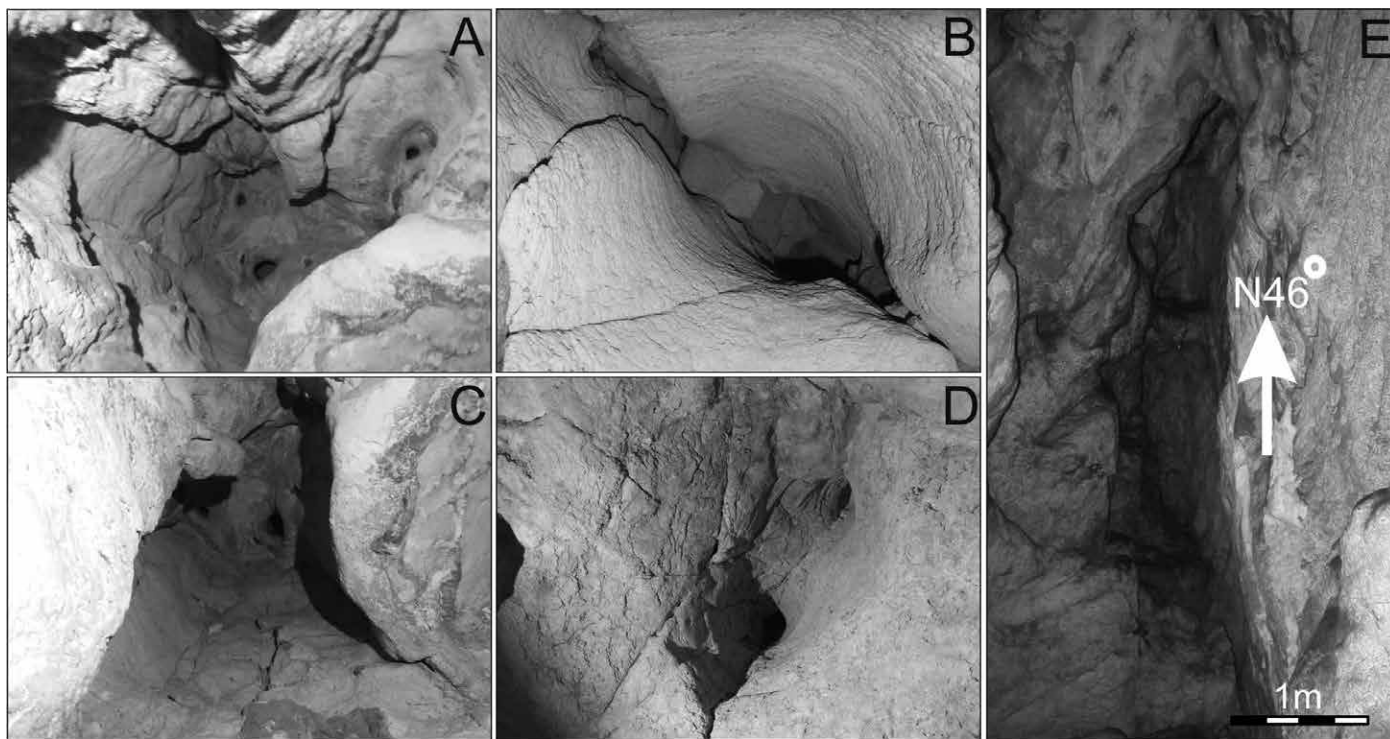


Figure 4. The vertical shafts (A–D) with upward continuation. Most of them routed on the fracture and developed oval-shape sections, (E) The roof of the inner part of the cave showing its development along a pre-existing crack. The location of the roof is shown in Figure 3, marked 4.

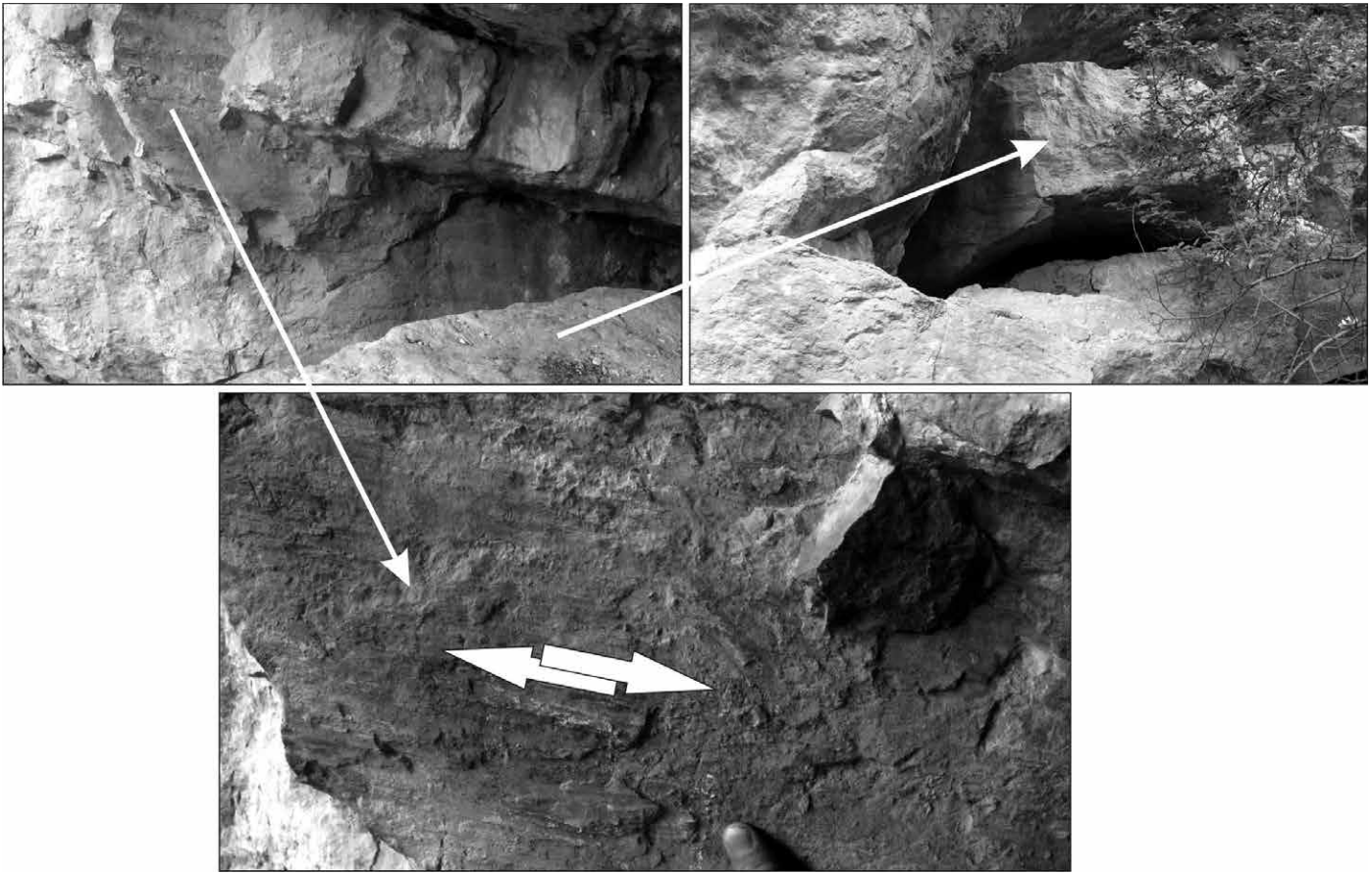


Figure 5. Strike-slip fault near the actual entrance of the cave. Its situation is marked 1 in Figure 3.

in cross-section (Fig. 4). The roof of the inner part of the cave (see area 4 on the cave map in Fig. 3) shows shaft development along a pre-existing fissure (Fig. 4).

Horizontal or oblique-slip movement may have occurred on some of the fractures because a left-lateral strike-slip fault with almost the same strike ( $N 50^\circ$ ) is observed in the northern part of the cave entrance ( $N 50^\circ 80^\circ SSE 11^\circ NE$ ) (see area 1 on the cave map in Fig. 3 and Fig. 5). Reactivation of faults and the opening of subsurface migration routes for meteoric waters had an important role in development of the cave. A number of reverse faults have also been observed near the cave entrance, but do not appear to have had a significant effect on the cave.

### Geophysical survey

The ground-penetrating radar allowed qualitative and quantitative surveys of the cave floor deposits. The aerial extent of the geophysical survey in the central chamber is presented by the profile lines in Fig. 3.

The deposits were divided into horizontal layers 0.25 m thick. Horizontal cross-sections of the floor stratum in the chambers with the pit are presented in Figure 6. Layer 1 corresponds to the cave floor surface. The next layer, 0.25 m deep, contains features whose colors were substantially different from those of the background (white color marks limestone blocks and boulders). With increasing depth, contours bounding the buried limestone blocks and the depths of their spreading in the horizontal sections become more apparent (Fig. 6).

Based on data produced by the analysis of two-dimensional GPR surveys, a three-dimensional model was produced (Fig. 7), where the white and green colors correspond to hard limestone blocks; and the dashed lines mark the borders of soft sedimentary deposits. A sedimentary layer is outlined in the central part of the section, and limestone blocks are recorded in more marginal areas.

The GPR surveys reveal the presence of buried limestone blocks and boulders, which are the possible result of cave roof collapse. This suggestion is further verified by ground-truthing in the pit sections through the cave sediment. The location of the pit was chosen according to GPR survey as a place with fewer blocks and boulders.

### Sediment sources (collapse and clastic deposits)

Sedimentological investigations of the southeast and southwest walls of the pit (Fig. 3), which was excavated in 2016-2018, showed six stratigraphic layers (Figs 8 and 9).

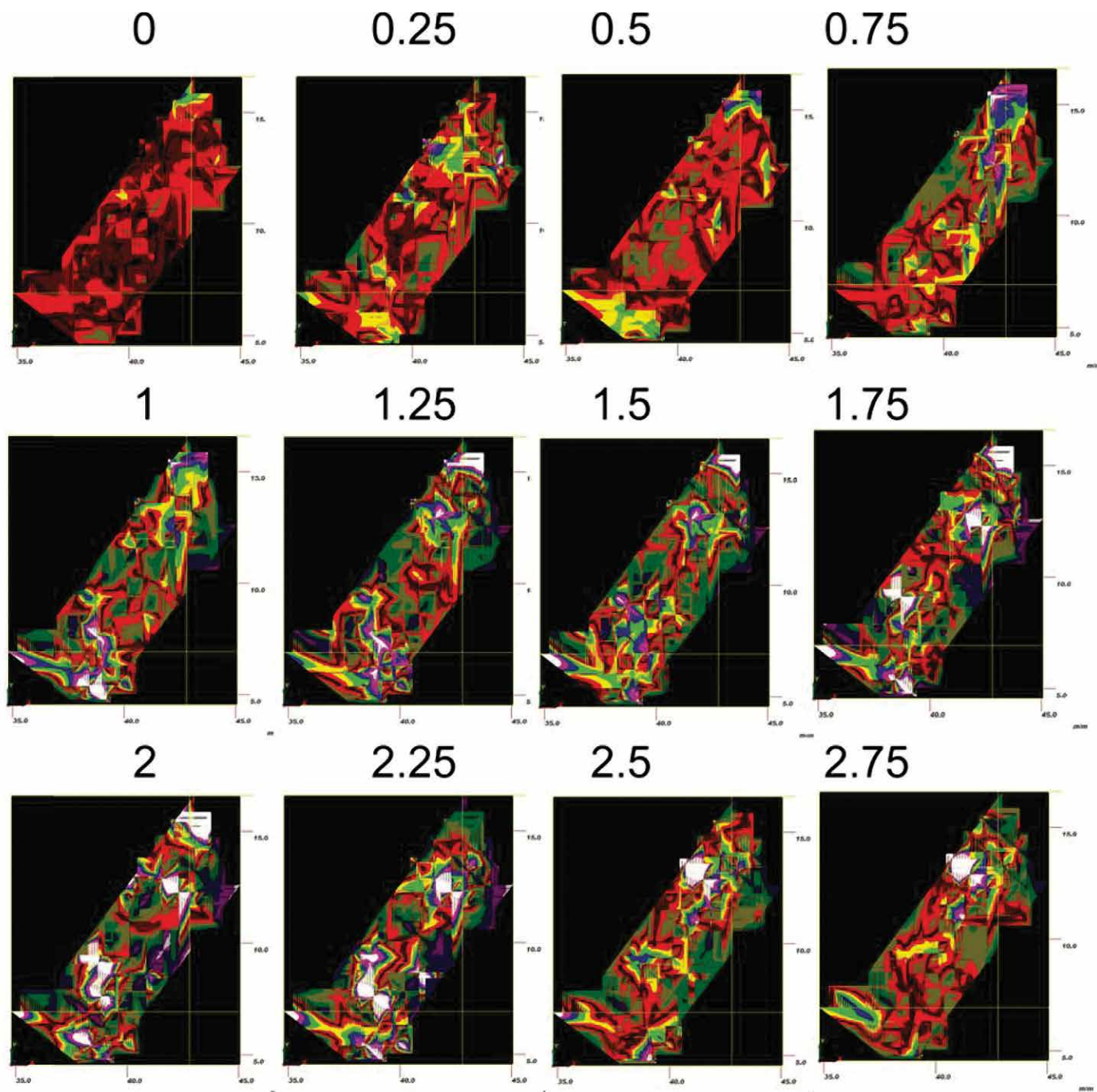


Figure 6. Horizontal sections of the GPR survey along depth (with the step of 0.25 m) in the chambers of the excavated pit (Figure 3) (white color marks buried limestone blocks).

The lowermost layer H (15–40 cm thick) comprises of a strongly calcareous, pale yellow (2.5Y 7/4) silt loam. The observed layers are not, or only slightly, stratified and developed over different time intervals. The coarse collapse debris by contrast developed instantaneously. Layer H has loess-like features and is archeologically barren, containing less material than the overlying layers. Layer H is overlain by layer F (a dark brown (10YR 3/3) sandy loam, up to 30 cm thick) rich in organic matter and demonstrate some post-depositional perturbations (Fig. 9). Layer G presented only in southwest wall of the pit comprises of olive (5Y 5/3) loam with isolated clasts of limestones (0.5–30 cm). Layer E mainly consists of grayish-brown (2.5Y 5/2) calcareous loamy sand (10–70 cm); it contains pale brown clay lens in its upper part (E') and dark grayish-brown (2.5 Y 4/2) lens E''. The latter is composed of calcareous silt containing phytolith particles. Layer D (20–30 cm) is a pale brown (10YR 6/3), silty clay loam displaying a weak stratification. Layer C (5–35 cm) is composed of whitish-grey (2.5Y 7/3), strongly calcareous silty clay-loam with limestone granules and bones. Layer B,



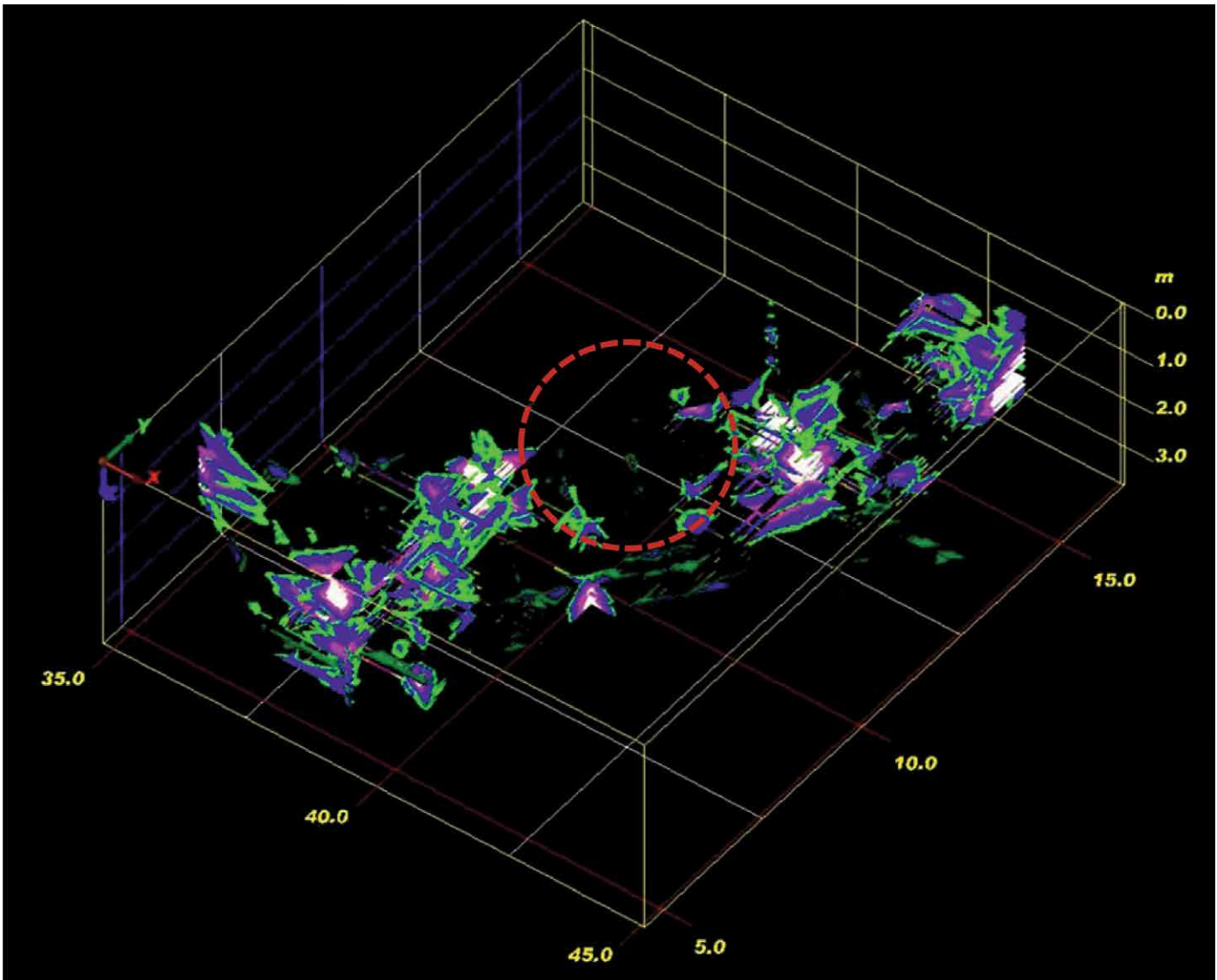


Figure 7. The 3D model of the hall with the pit (the white and gray colors correspond to limestone blocks; the dashed lines encompass the soft sediments).

50–80 cm thick, is a light olive-brown (2.5Y 5/4), friable, calcareous sandy loam and contains small carbonate pebbles.

The layers A and B were formed between  $24,589 \pm 149$  BP and  $22,947 \pm 204$  BP according to  $^{14}\text{C}$  dating on bones from different depths (Antonosyan et al., 2019). The top 2 cm below the present-day cave floor is a blackish calcareous cave sediment horizon (A') which overlies pale-brown (10YR 6/3) loam (5–12 cm) containing pebbles and bones (A).

Karin Tak cave contains a variety of siliciclastic and chemical sediments deposited by a range of mechanisms. Autochthonous deposits are derived from the surrounding bedrock and include collapse breccia and their breakdown products.

Breakdown products consist of fragments of bedrock with a range of clast sizes, most of which result from cave collapse due to seismic activity. Less pronounced collapse features include wedge-shaped debris cones that are developed below collapsed sinkholes (see area 3 on the cave map in Fig. 3). Within the pit excavated in the cave floor, limestone clasts <0.25 m in diameter were observed in the SW wall in layer D (Fig. 9).

Large blocks of limestone were observed near the cave entrance (2 in Fig. 3), which has retreated due to past episodes of collapse. These blocks probably correspond to collapse debris (including limestone blocks and boulders of >0.5 m in diameter) identified by the radar survey and observed in deeper parts of the floor pit (Figs. 7, 8 and 9).

The allochthonous sediments, derived from external sources, include washed-in soils, debris flows, and materials derived from biological (animal and possibly human) activity. The most accentuated layers with these sediments are the layers A, B, C, D, E, and especially F. Detrital sediments include sands and silts deposited from subsurface streams and storm run-off into sinkholes. They are present in practically all layers. Chemical deposits include calcite and gypsum



Figure 8. Photography of the southwest and southeast walls of the excavated pit.

together with oxides and hydroxides of iron and manganese. Speleothems, including stalactites, stalagmites, and stalagnates (columns) are less developed in the biggest chambers and more prominent in the NE end of the cave.

The light mineral composition in sediments from A to D layers is presented mostly by undetermined weathered minerals, lesser amounts of volcanic glass, plagioclase, quartz, phylolith, and opal. The heavy mineral assemblages are characterized by clear predominance of opaque minerals with abundant ilmenite, with lesser amounts of hornblende and diopside. Carbonate content varies from 26.1–38.5 %.

Samples for pollen analyses were taken from the SE and SW walls of the cave-floor pit (Figs 8 and 9). More than 400 grains were counted for each sample, and grain proportions were calculated based on the sum of all palynomorphs present. The results (Fig. 10) point to the presence of abundant organic material in layers A, B and E'. In lens E' and in layer H, no pollen or other palynomorphs were found (Fig. 10).

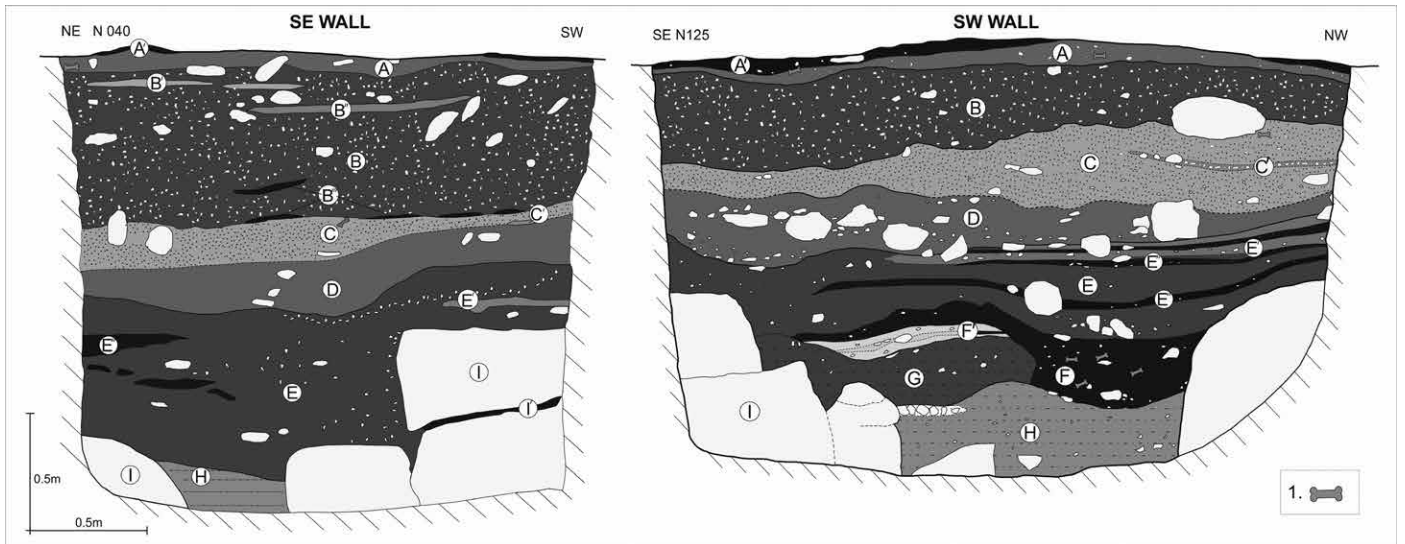


Figure 9. Log of the southwest and southeast walls of the pit. Cave sediment colors according to the Munsell color chart. (A) Pale brown loam with pebbles and bones; (A') Blackish soil horizon; (B) Light olive brown sandy loams with limestone rubbles; (B') Carbonate crust lenses; (B'') Very pale brown strongly calcareous clay lens; (B''') Very dark grayish brown clayey lenses; (C) Light brownish silty clay loam with limestone pebbles, bones; (C') Rubified lens; (D) Pale brown silty clay loam; (E) Grayish brown loamy sand; (E') Pale brown clay lens; (E'') Dark grayish brown calcareous silty lens; (I) Limestone boulders; (I') Very dark grayish clay; (G) Olive loam; (F) Dark brown sandy loam; (H) Pale yellowish brown silt loam; (1) Bones.



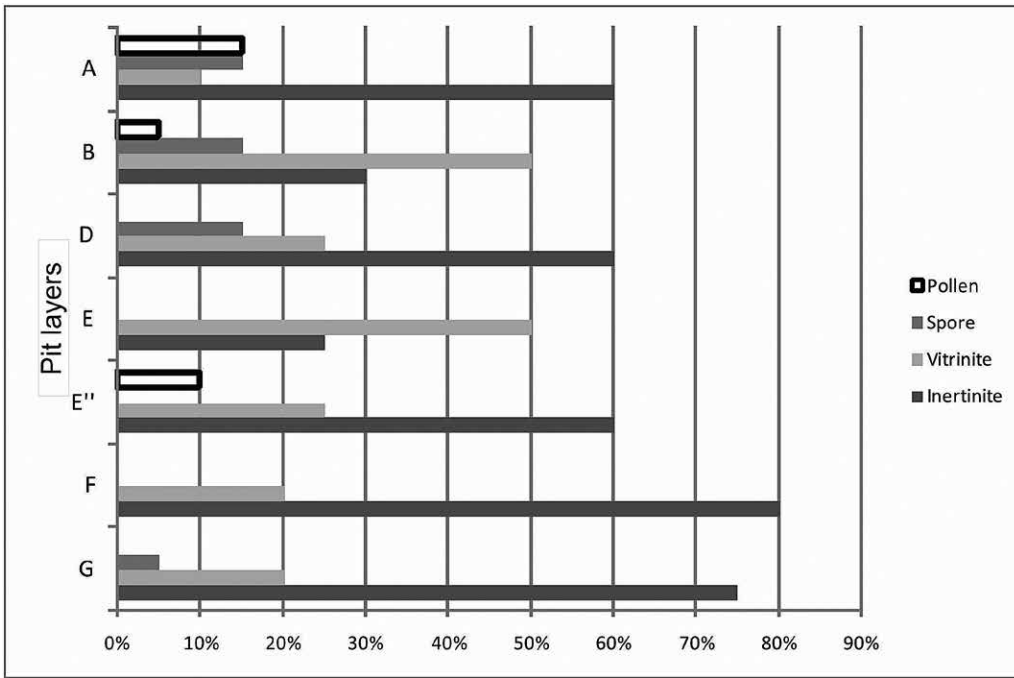


Figure 10. Summary diagram showing pollen and palynomorphs (pollen, spore, vitrinite, inertinite).

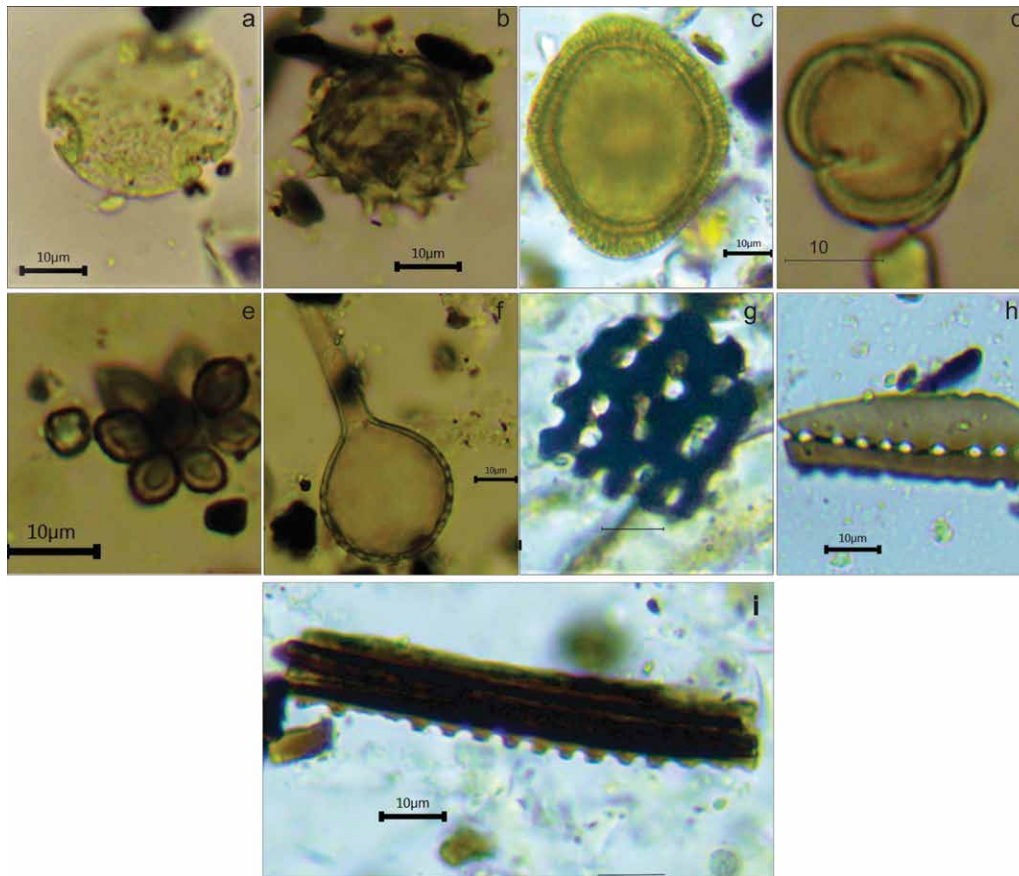


Figure 11. Representative micrographs of pollen and palynomorphs under light microscope: (a) *Tilia* sp. (fam. *Malvaceae*), (b) *Asteraceae* sp., (c) *Tsuga* sp. (fam. *Pinaceae*), (d) *Fraxinus* sp. (fam. *Oleaceae*), (e, f) Fungi, (h, i) Phytoclasts (a, b, f) from the layer (A), (c) ( layer B), (d, i) (layer E), (e, g) (layer D), (h, i) (layer F).

A geochemical study of the chert lens observed a few hundred meters from the cave in the upper part of the volcanoclastic rocks showed that some elemental ratios are similar to those in layer F (Fig. 13). Chert, a high-silica rock dom-

Layer A contains pollen from *Tilia* sp. (fam. *Malvaceae*), *Fraxinus* sp. (fam. *Oleaceae*), *Apiaceae* sp., *Asteraceae* sp., *Quercus* sp. (fam. *Fagaceae*), and *Chenopodiaceae* sp. (Fig. 11), layer B contains pollen from *Tsuga* sp. and small amounts of *Pinus* sp. (fam. *Pinaceae*), *Rosaceae* sp., *Quercus* sp. (fam. *Fagaceae*), and *Asteraceae* sp. (Fig. 11). In the lens E'', *Asteraceae* sp. and *Quercus* sp. (fam. *Fagaceae*) pollen were recorded (Fig. 11 a-d). Large amounts of fungal spores, phytoliths, and charcoals were recorded in many samples (Fig. 11 e-i). Pollen preservation was poor and taxonomic resolution to species level was impossible.

**Bulk sediment geochemistry: X-ray fluorescence**

Nine cave sediment samples from the pit in the floor of Karin Tak cave were analyzed for their contents of elemental Pb, Cr, Pb, Ba, Mo, Cu, Sr, Co, Ti, As, Zn, Zr, V, and Mn (Fig. 12).

Geochemical markers in layers G and F at nearly the same stratigraphic level in the floor pit (SW wall, Fig. 9) show quite different content of Pb, Cr, Rb, Ba, Fe, Co, Ti, As, Zr and V (Fig. 12). Results showed comparable high contents of Pb, Cr, Rb, Ba, Fe, Mo, Co, Ti, As, Zn, Zr, V, and Mn in layer F and depleted contents of Pb, Cr, Rb, Ba, Fe, Co, Ti, As, Zr, and V in layer G. The difference in Mo, Mn and Zn contents are less marked in layers F and G. The layers E, F and G are characterized by peaks in the contents of Cu, Zn, and Mo; Mo enrichment also occurs in layer A.

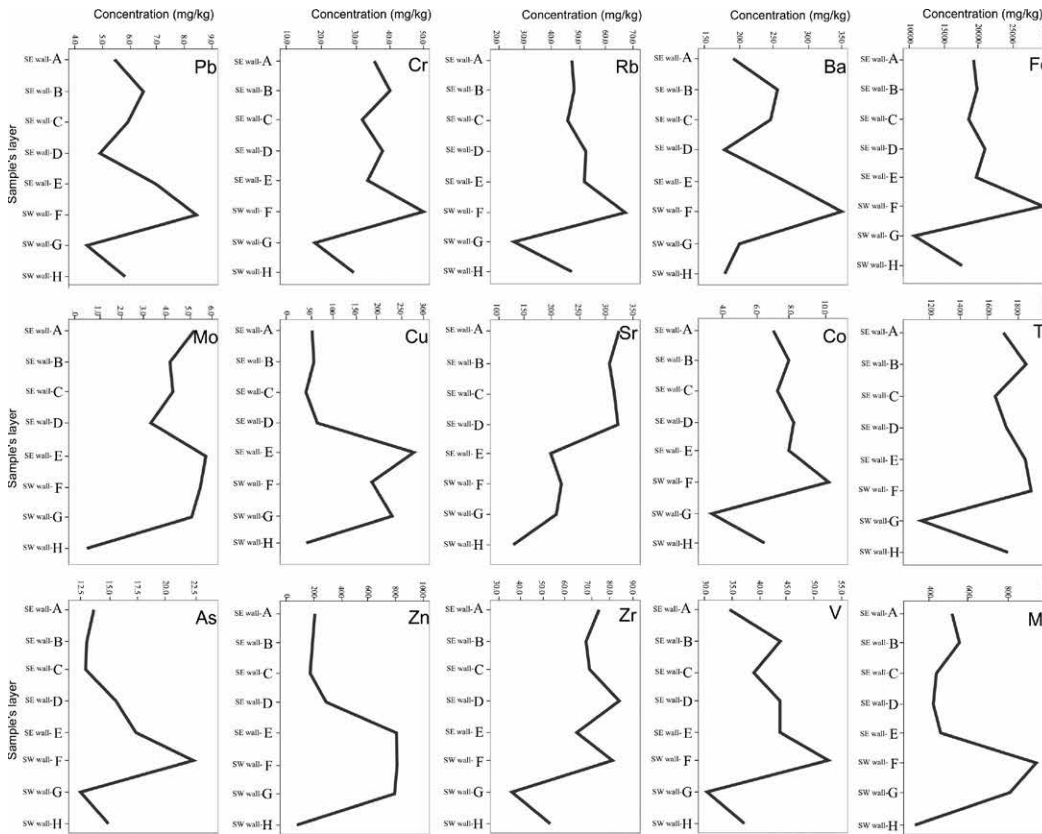


Figure 12. Trace element analyses of the pit layers (A–H).

ical, and climatic factors. The cave originated with Neogene regional uplift when the regression of the Sarmatian Sea occurred and continental conditions were initiated conducive to the exposure of the Jurassic carbonate rocks to the surface and to subaerial weathering and karstification. The cave is developed along NW–SE trending oblique slip faults and fissures indicating a structural control. The presence of numerous vertical shafts in the cave, together with sinkholes and speleothems, indicate its epigenetic nature. Nevertheless, we have observed one or two cupolas, the origin of which

inantly composed of SiO<sub>2</sub> minerals were among the first raw materials utilized by hominine.

In general, the Sr and Zr contents decrease with depth (Fig. 12), as does the content of Mo except for layers E, F and G. The content of V was correlated with that of Ba. Ba shows a positive value in layer F and a negative value in layers A, D, G and H. The loess-like sample from layer H is free of organic material and shows negative anomalies of Mn, Ba, Sr, Zn and Mo.

### DISCUSSION

Both external and internal factors control the development of caves in carbonate rocks, and the origin and development of Karin Tak cave was influenced by tectonic, lithological, and climatic factors. The cave originated with Neogene regional uplift when the regression of the Sarmatian Sea occurred and continental conditions were initiated conducive to the exposure of the Jurassic carbonate rocks to the surface and to subaerial weathering and karstification. The cave is developed along NW–SE trending oblique slip faults and fissures indicating a structural control. The presence of numerous vertical shafts in the cave, together with sinkholes and speleothems, indicate its epigenetic nature. Nevertheless, we have observed one or two cupolas, the origin of which is unclear, therefore, in the initial stages, the hypogenic influence is not excluded as in the case of Azokh Cave in the same geographic region, developed in Jurassic limestones (Domínguez-Alonso et al., 2016). Even if there were hypogenic parts in the formation of the cave, it is minimal and epigenetic ones are dominant. Cave development activity is not the same now as it was at the beginning of its formation: after the roof collapse and breakdown no speleothems were formed in the two largest chambers of the cave.

Geophysical investigations in the central cham-

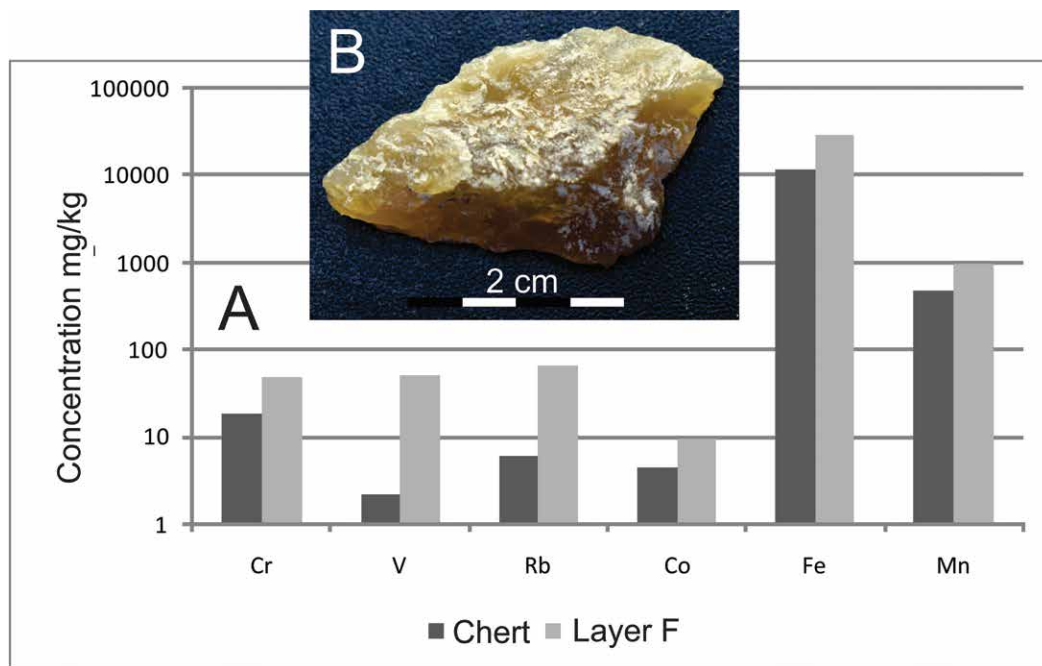


Figure 13. Trace element analyses of the chert and pit layer (F).

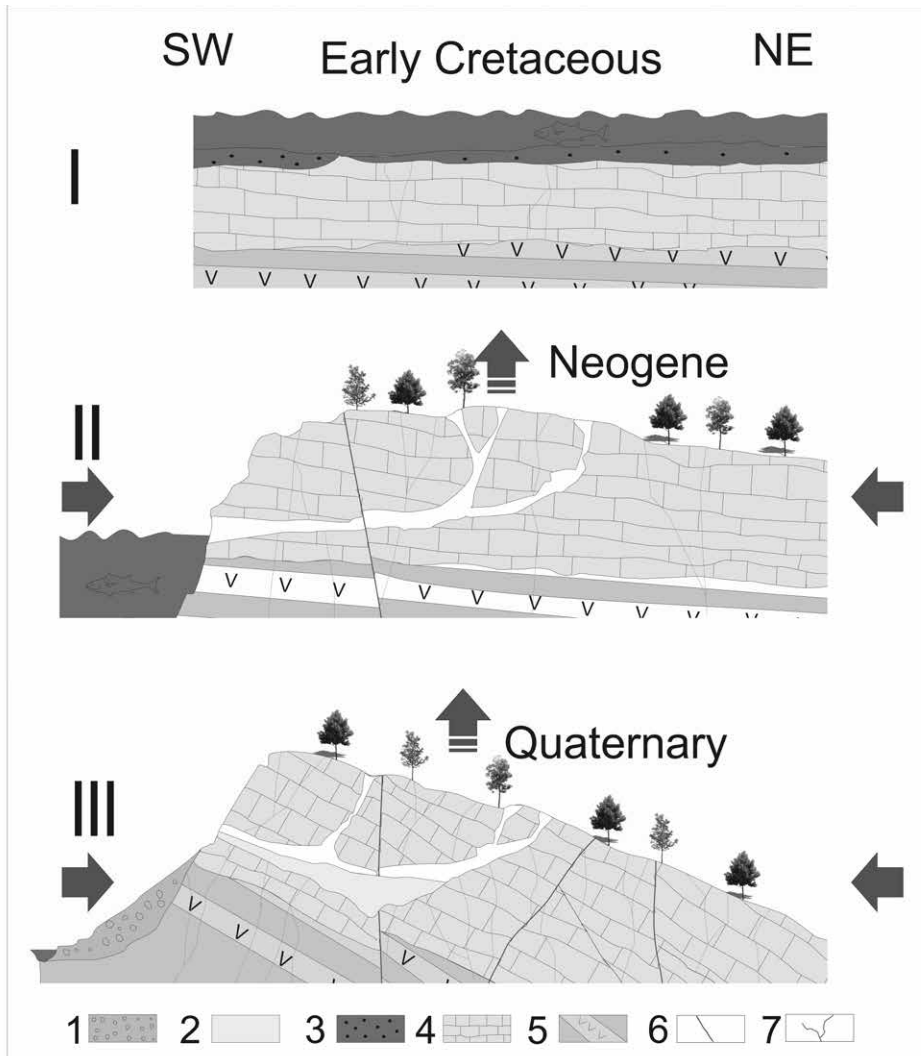


Figure 14. Cave development stages. (I) Cretaceous, (II) Miocene-Pliocene, (III) Pleistocene-Holocene. (1) colluvion, (2) recent cave sediments, (3) dip non-consolidated sediments, (4) Callovian-Oxfordian limestones, (5) Bathonian volcanoclastics, (6) faults, (7) fractures. SW-NE cross section line shown in Figure 1.

dramatic climate change during LGM MIS 2.

The X-ray fluorescence studies of cave sediment samples identified variations in elemental compositions, although the effects of post-depositional contamination (e.g., due to human activity should be carefully considered).

From a stratigraphic point of view, it is interesting to compare the geochemical markers in layers G and F. Although these layers are adjacent (Fig. 9) they show quite different contents. As, Cr, Cu, Pb, Zn, and Ba positive anomalies can be result of concentrations of skeletal and organic detritus or charcoals (e.g., Basta et al., 2005; Calvert and Pedersen, 2007), which are visible by *in situ* observation of layer F.

The increased concentrations of Fe and Ti may derive from the bones of animals, but may also be linked with higher contents of ilmenite mineral observed in layers A-D by the immersion method.

The contents of Cu, Zn and Mo are abundant in layers E, F and G; however, they are not related to human activity such as metallurgy, because the age of the layers (>41,700 BP) places them long before the Copper and Bronze Ages. An interesting result from the trace element analyses of the chert sample and layer F was obtained. X-ray study of the chert sample showed similarities with soil layer F for several elements (Cr, V, Rb, Co, Fe, Mn) (Fig. 13, A). The only chert piece, probably a tool (Fig. 13, B) was found in rubbish of washed material (unfortunately of unknown exact stratigraphic position). The aforementioned data shows the high probability of using the chert as a raw material, but more finds will be needed for future investigations.

## CONCLUSIONS

- The Karin Tak cave has important tectonic control. The NW-SE trending oblique-slip faults and dominant fissures favored the cave initiation and its general orientation. The hypogenic influence in the initial stages is not

bers allowed us to map and also distinguish relatively soft deposits from harder limestone blocks resulting from the roof collapse. The excavations are focused on the central area (outlined by the dashed line in Fig. 7), which is promising in terms of archaeological and biological remains. Pollen grains were observed in layers A and B (Fig. 11) formed between 24.803–34.486 Cal BP (Antonosyan et al., 2019). The overall pollen profile is dominated by trees that are adapted to relatively moist and cool temperate areas with cool summers to very heavy winter snowfalls and ice storms. The pollen record is over-represented in conifers (>60%), which belong to the genera of *Tsuga* sp. (Fig. 11, c) and *Pinus* sp. Deciduous trees from the genres of *Fraxinus* sp. (Fig. 11, d) and *Quercus* sp., which demand comparably dry soil and are more photophilic, are relatively well-represented. These trees are more distributed in the tropical and subtropical regions of the northern hemisphere. The presence of inertinite in the cave sediment samples (equidimensional opaque in the sections) indicates a relatively long transportation distance.

The new pollen data presented in this study is consistent with the results of Antonosyan et al. (2019) and provides no evidence of dramatic climate change during LGM MIS 2.

excluded, but the presence of numerous vertical shafts in the cave together with sinkholes and speleothems indicate its principal epigenic nature.

- The geophysical, morphological, and sedimentary study indicates two major collapses of different magnitudes of presumed seismic origin. The material of the second, less pronounced collapse, forms a wedge-shaped cone, which becomes thicker below the collapsed sinkhole. The first more important collapse is the result of the roof collapse (breakdown).
- The pollen record evidence of non-dramatic climate change during LGM MIS 2 in the area and it could serve as a refugial zone for hominin activity.
- Layer F, rich in organic matter and its similarity in several elements to the chert sample (possible raw material) from the surrounding rocks, indicates hominin activity. Nevertheless, the high contents of Cu, Zn and Mo are not related to human activity such as metallurgy.

## ACKNOWLEDGMENTS

This work is supported by the Science Committee of the Republic of Armenia, in the frames of the research project № 18T-1E131. The authors are grateful for constructive remarks of the anonymous reviewers that helped to significantly improve the first version of the manuscript.

## REFERENCES

- Adler, D.S., Wilkinson, K.N., Blockley, S., Mark, D.F., Pinhasi, R., Schmidt-Magee, B.A., Nahapetyan, S., Mallol, C., Berna, F., Glauberman, P.J., Raczynski-Henk, Y., Wales, N., Frahm, E., Jöris, O., MacLeod, A., Smith, V.C., Cullen, V.L., and Gasparian, B., 2014 Early Levallouis technology and the Lower to Middle Paleolithic transition in the Southern Caucasus: *Science*, v. 345, p. 1609–1613, <https://doi.org/10.1126/science.1256484>.
- Antonosyan, M., Seersholm, F. V., Greal, A. C., Barham, M., Werndly, D., Margaryan, A., and Yepiskoposyan, L., 2019, Ancient DNA shows high faunal diversity in the Lesser Caucasus during the Late Pleistocene: *Quaternary Science Reviews*, v. 219, p. 102–111. <https://doi.org/10.1016/j.quascirev.2019.07.012>.
- Avagyan, A., Sosson, M., Karakhanian, A., Philip, H., Rolland, Y., Melkonyan, R., and Davtyan, Y., 2010, Recent stress-field evolution in the Lesser Caucasus and adjacent regions. *in* Sosson, N., Kaymakci, N., Stephenson, R., Bergerat, F., and Starostenko, V., eds., *Sedimentary Basin Tectonics from the Black Sea and Caucasus to the Arabian Platform*, Geological Society of London, Special Publication, v. 340, p. 393–408, <http://dx.doi.org/10.1144/SP340.17>.
- Avagyan, A., Sosson, M., Sahakyan, L., Sheremet, Y., Vardanyan, S., Martirosyan, M., and Muller, C., 2018, Tectonic evolution of the South-Eastern margin of the Ararat basin, (Lesser Caucasus, Armenia): *Journal of Petroleum Geology*, v. 41, n.4, p. 495–511, <https://doi.org/10.1111/jpg.12718>.
- Bar-Yosef, O., Belfer-Cohen, A., Mesheviliani, T., Jakeli, N., Bar-Oz, G., Boaretto, E., Goldberg, P., Kvavadze, E., and Matskevich, Z., 2011. Dzuazuana: an upper palaeolithic cave site in the Caucasus foothills (Georgia): *Antiquity*, v. 85, p. 331–349. <https://www.antiquity.ac.uk/ant/085/ant0850331.htm>.
- Basta, N.T., Ryan, J.A., and Chaney, R.L., 2005, Trace element chemistry in residual treated soil: *Journal of Environment Quality*, v. 34, p. 49–63, <https://doi.org/10.2134/jeq2005.0049dup>.
- Bertacchi, A., Gasparian, G., Gruwier, B., Rivals, F., and Kandel, W.A., 2020, Upper Paleolithic animal exploitation in the Armenian Highlands: The zooarchaeology of Aghitu-3 Cave: *Quaternary International*, v. 587–588, p. 400–414. <https://doi.org/10.1016/j.quaint.2020.04.029>.
- Calvert, S.E., and Pedersen, T.F., 2007, Elemental proxies for palaeoclimatic and palaeoceanographic variability in marine sediments: interpretation and application: *in* Hillaire-Marcel, C., De Vernal, A. eds., *Proxies in Late Cenozoic Paleoclimatology: Developments in Marine Geology*, Elsevier, p. 567–644. [https://doi.org/10.1016/S1572-5480\(07\)01019-6](https://doi.org/10.1016/S1572-5480(07)01019-6).
- Clark, P.U., Dyke, A.S., Shakun, J.D., Carlson, A.E., Clark, J., Wohlfarth, B., Mitrovica, J.X., Hostetler, S.W., and McCabe, A.M., 2009, The last glacial maximum: *Science*, v. 325, p. 710–714, doi:10.1126/science.1172873.
- Domínguez-Alonso, P., Aracil, E., Porres, J.A., Andrews, P., Lynch, E.P., and Murray, J., 2016, Geology and geomorphology of Azokh Caves: *in* Azokh Cave and the Transcaucasian Corridor, Fernández-Jalvo, Y., ed., Springer, p. 55–84. DOI: 10.1007/978-3-319-24924-7\_3
- Fernández-Jalvo, Y., Andrews, P., King, T., and Yepiskoposyan, L., 2016, Introduction: Azokh Cave and the Transcaucasian Corridor: *in* Delson, E., Sargis, E., eds., *Vertebrate Paleobiology and Paleoanthropology*. Springer, Dordrecht, p. 1–26, [https://doi.org/10.1007/978-3-319-24924-7\\_1](https://doi.org/10.1007/978-3-319-24924-7_1).
- Gabrielyan, A., Sarkisyan, H., Simonyan, G. 1981, *Seismotectonics of the Armenian SSR*: Yerevan State University; Pub. Yerevan, Armenian Soviet Socialist Republic, 283 p. (in Russian).
- Gabunia, L., Vekua, A., Lordkipanidze, D., 2000, The environmental contexts of early human occupation of Georgia (Transcaucasia): *Journal of Human Evolution*, v. 38, p. 785–802. <https://doi.org/10.1006/jhev.1999.0383>.
- Grichuk, V.P., Zaklinskaya, E.D., 1948, *Analiz-iskopaemykh pylyci i spor i ego primenenie v paleogeografii*: (Fossil pollen and spore analysis and its application in paleogeography). Pub. OGI, Moscow, 223 p.
- Johnson, C.C., Demetriades, A., Locutura, J., and Ottesen, R.T. Eds., 2011, *Mapping the Chemical Environment of Urban Area*, First edition, Wiley-Blackwell, 640 p., <https://doi.org/10.1002/9780470670071>.
- Margaryan, A., Derenko, M., Hovhannisyants, H., Malyarchuk, B., Heller, R., Yepiskoposyan, L., Willerslev, E., and Allentoft, M. E., 2017, Eight millennia of matrilineal genetic continuity in the South Caucasus: *Current Biology*, v. 27, p. 2023–2028. <https://doi.org/10.1016/j.cub.2017.05.087>.
- Provan, J., and Bennett, K.D., 2008, Phylogeographic insights into cryptic glacial refugia: *Trends in Ecology and Evolution*, v. 23, p. 564e571. <https://doi.org/10.1016/j.tree.2008.06.010>.
- Rothwell, R.G., and Croudace, I.W., 2015, Micro-XRF studies of sediment cores: A perspective on capability and application in the environmental sciences, *in* Croudace, I. W. and Rothwell, R. G. eds., *Twenty years of XRF core scanning marine sediments: What do geochemical proxies tell us?* (Developments in Paleoenvironmental Research, 17) Dordrecht, NL: Springer, p. 25–102. [https://doi.org/10.1007/978-94-017-9849-5\\_2](https://doi.org/10.1007/978-94-017-9849-5_2).
- Shikhaylibeli, E., Abdulaev, R., Gasanov, T., Musaev, A., Panakhov, A., Gamzaev, O., and Akhundov, A., 1994. *Geologia i poleznie iskopaemie Nagornogo Karabakha*: ANA, Academie of Sciences of Azerbaijan. Institute of geology named after Academician I.M. Gubkina, p. 284 (In Russian) [Translation: Geology and minerals of Nagorno-Karabakh.]

Ara, Lilit H., Hayk, Mikayel, Kristina, Maria, Gevorg, Lilit V., Tatul, Taron, Narek, Seda, and Levon

- Sosson, M., Rolland, Y., Muller, C., Danelian, T., Melkonyan, R., Adamia, S., Kangarli, T., Avagyan, A., Galoyan, G., and Mosar, J., 2010, Subductions, obduction and collision in the Lesser Caucasus (Armenia, Azerbaijan, Georgia), new insights: *in* Sosson, M., Kaymakci, N., Stephenson, R., Bergerat, F., and Starostenko, V. eds., *Sedimentary Basin Tectonics from the Black Sea and Caucasus to the Arabian Platform: Special Volume Geological Society of London*, v. 340, p. 329–352. <http://dx.doi.org/10.1144/SP340.14>
- Stafford, T., and Yepiskoposyan, L., 2015, Cave survey, Summary of Radiocarbon, Geological and Zooarchaeological Data from Test Excavations at Karin Tak Cave, Artsakh Republic (unpublished report).
- White, W.B., 2007. Cave sediments and paleoclimate. *Journal of Cave and Karst Studies*, v. 69, p. 76–93.



# LAND-USE IMPACTS ON THE HYDROLOGY OF THE HIDDEN RIVER GROUND-WATER SUBBASIN, HORSE CAVE, HART COUNTY, KENTUCKY

Cesalea N. Osborne<sup>1,2\*</sup>, David J. Keeling<sup>1</sup>, Jason S. Polk<sup>1</sup>, Patricia N. Kambesis<sup>1</sup>, and Kevin B. Cary<sup>1</sup>

---

## Abstract

Hidden River Cave, located in the city of Horse Cave, Ky., forms one of the main tributaries of the Hidden River groundwater subbasin that spans multiple counties in south-central Kentucky. Hidden River Cave formed in Mississippian-aged carbonates and consists of a dendritic network of canyons and collapsed domes; a major trunk stream flows through the cave that supports myriad subsurface ecosystems and recharges the Mammoth Cave aquifer and the Green River, important water resources on which several communities depend. Poor land-use practices historically have contaminated the cave stream. As a result, the hydrology of the Hidden River groundwater subbasin has been extensively studied using fluorescent dye-tracing, and developments in groundwater resource management have improved cave conditions. However, land-use boundaries that intersect with areas of recharge still influence contaminant transport to groundwater. This study combined groundwater dye-tracing, high-resolution stage data collection, and supervised classification in a geographic information system (GIS) to assess land-use impacts on the hydrology of the Hidden River groundwater subbasin. Dye-tracing confirmed that stormwater infrastructure in Horse Cave discharges to Hidden River Cave, and, subsequently, the Hidden River groundwater subbasin. High-resolution stage data determined that the cave's major trunk streams respond to precipitation within 40 minutes to 1.5 hours, while baselevel conditions, except after sustained precipitation, are met three to four days after precipitation ends. Supervised classification determined that development is concentrated in Horse Cave and has increased by approximately 7 % between 1989 and 2017. These results suggest opportunities for the implementation of karst-specific stormwater management regulations where such regulations are weak.

---

## INTRODUCTION

Institutional policies that govern groundwater management at local, regional, and global scales often are either lacking or absent, which is particularly true, and even more challenging, where aquifers span the geographic boundary of multiple political territories. Approximately 263 transboundary groundwater resources exist globally, many of which lie in karst regions (Jarvis et al., 2005). Karst, characterized by the chemical dissolution of carbonate bedrock, comprises 15–20 % of the Earth's ice-free landscape and includes karst aquifers, which provide 25 % of the world's population with drinking water (Ford and Williams, 2007; Palmer, 2007). In karst regions, surface and groundwater flow are highly interconnected, and drainage occurs rapidly through conduits created by dissolution. Thus, the distribution and availability of groundwater resources is highly variable. Further, contaminants that enter the subsurface of karst regions can easily be dispersed throughout the groundwater system and across political boundaries.

Some of the challenges associated with policy development regarding transboundary karst aquifers include a limited understanding of recharge and discharge mechanics and uncertainties in the spatial and temporal components of subsurface flow (Theesfeld, 2010; Milanović, 2016). Some transboundary karst aquifers (i.e., the Dinaric, Yucatán Peninsula, and Arbuckle-Simpson karst aquifers) have benefited from hydrogeologic studies, such as groundwater dye-tracing and the development of groundwater flow models, to characterize subsurface flow (Bauer-Gottwein et al., 2011; Christenson et al., 2011; Stevanović et al., 2016). Studies such as these provide data for the implementation of groundwater protection policies where such policies are either weak or absent; however, challenges related to the lack of systematic monitoring and inconsistent land-use zoning have limited the ability to implement policies that are specific to the protection of karst aquifers. Few karst regions in the world have been more extensively studied and, more notably, dye-traced than in south-central Kentucky.

South-central Kentucky is a classic example of a well-developed karst landscape and includes the longest-known cave system, Mammoth Cave. Three physiographic regions comprise this area, including the Mammoth Cave Plateau, the Dripping Springs Escarpment, and the Pennyroyal Plateau, as well as the shallow, well-developed Mammoth Cave karst aquifer that formed in the Girkin, Ste. Genevieve, and St. Louis Limestones (Palmer, 1995). The once widely-accepted concept of “out of sight, out of mind,” coupled with rapid recharge and discharge rates, historically led to the contamination of the Mammoth Cave aquifer via point-source pollution; specifically, the intentional, direct injection of waste into the subsurface.

---

<sup>1</sup>Department of Earth, Environmental, and Atmospheric Sciences, Western Kentucky University, Bowling Green, KY 42101

<sup>2</sup> current affiliation: Oklahoma Geological Survey, Sarkeys Energy Center, Norman OK 73019

\* Corresponding author cesalea.osborne@gmail.com

Between 1975 and 1987, regional hydrogeologic investigations, including over 500 groundwater dye-traces, were conducted in the south-central Kentucky karst region to identify sources of contamination. Twenty-eight major groundwater basins were delineated in the Pennyroyal Plateau physiographic region during this time, including the Gorin Mill groundwater basin, one of the largest in south-central Kentucky, draining an area of 394 km<sup>2</sup> (Quinlan and Ewers, 1989; Meiman et al., 2001; Blair et al., 2012). The Gorin Mill groundwater basin drains two distinct subbasins that converge approximately eight kilometers northeast of the city of Horse Cave. The southwestern segment of this groundwater basin, known as the Hidden River groundwater subbasin, comprises over 80 % (324 km<sup>2</sup>) of the Gorin Mill groundwater basin and includes Hidden River Cave (Fig. 1). The results of the hydrogeologic investigations determined that the most extensive contamination occurred within the Hidden River groundwater subbasin.

The Hidden River groundwater subbasin is a trans-boundary basin that spans multiple counties in south-central Kentucky, including Barren, Hart, and Metcalfe counties, and includes L&N Cave (surveyed at 3 km) in Cave City, Hidden River Cave (16 km) in Horse Cave, and the Hidden River Complex (32 km) situated near the Green River, which have all been connected via groundwater dye-tracing. All serve as subsurface tributaries of the Hidden River groundwater subbasin and exhibit distributary flow; flooded, low-level conduits have created a system of interconnected passages where water flows north and resurges through 46 springs along the Green River, an important water resource on which several communities depend (Quinlan and Rowe, 1977). This study focused on Hidden River Cave due to its proximity to industrial development, its history of significant contamination, and its direct connection to the Mammoth Cave aquifer, which also serves as a water resource.

The entrance to Hidden River Cave is located in a 30 m deep collapse sinkhole that is owned and managed by the American Cave Museum (McGrain and Currens, 1978; Foster, 2009). High, interspersed breakdown rooms, large river passages, and floodwater mazes exist in the cave that recharge the Mammoth Cave aquifer and support myriad subsurface ecosystems (White et al., 1970; Quinlan and Ewers, 1989; Worthington et al., 2000).

Commercial development, along with point-source groundwater contamination, increased in Horse Cave during the 1970s. Pollutants were commonly injected into the subsurface through sinkholes and included raw sewage, heavy metals from a chrome plating plant, creamery waste, and oil refinery waste, among others. Based largely on the regional hydrogeologic investigations of Quinlan and Rowe (1977) and the Environmental Protection Agency (EPA, 1981), a new wastewater treatment facility was developed in 1989, which has significantly improved the water quality of Hidden River Cave. Additionally, the American Cave Conservation Association (ACCA) has established good working relationships with the industries that have directly impacted recharge to the cave system. Despite these changes in groundwater resource management, land-use boundaries in the city of Horse Cave intersect with areas of recharge that still introduce contaminants into the groundwater system.

This study used an integrative approach by combining groundwater dye-tracing, high-resolution stage data collection, and remote sensing analysis in a geographic information system (GIS) to assess land-use impacts on the hydrology of the Hidden River groundwater subbasin. Additionally, implications for U.S. federal, state, and local stormwater management regulations were reviewed, and suggestions were made to improve on these regulations to protect karst groundwater.

## MATERIALS AND METHODS

### Groundwater Dye-Tracing

Dye receptors were placed in Hidden River Cave at the East River, South River, areas in the Breakdown Canyon (i.e., the Breakdown Canyon entrance, Site 007, drainage wells), the Waterfall Room, and the headwaters of Wheel River (Fig. 2). The East River is the primary downstream tributary of Hidden River Cave and begins at the bottom of the cave's collapsed entrance, draining an area of ~150 km<sup>2</sup>. The South River is a smaller tributary of the East River

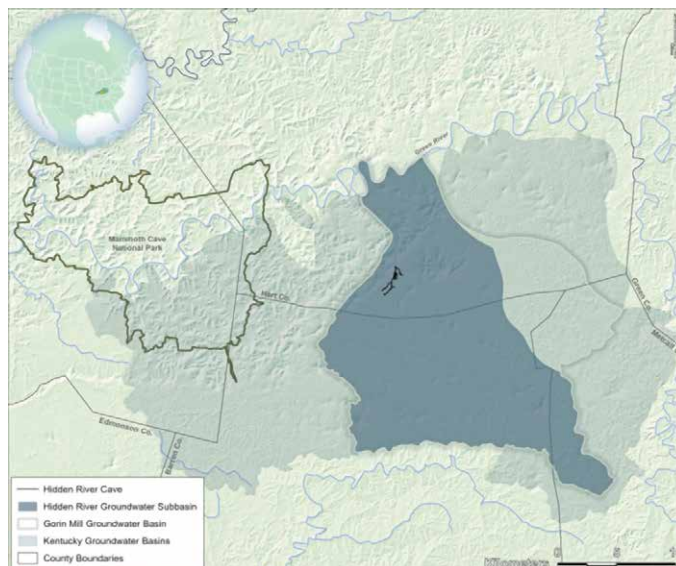


Figure 1. Groundwater basins in south-central Kentucky, including the Hidden River groundwater subbasin that makes up most of the larger Gorin Mill groundwater basin. Data from the Kentucky Division of Geographic Information (KDGI) (<https://kygeonet.ky.gov>) and the Kentucky Geological Survey (KGS) (<http://www.uky.edu/KGS/gis>).

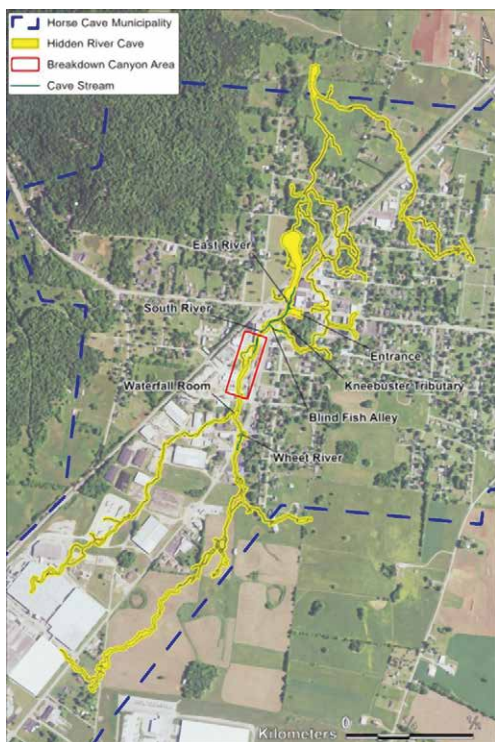


Figure 2. Hidden River Cave, Horse Cave, Kentucky. Data from the Cave Research Foundation and the KGS.

site exhibits the most notable source of contamination, where short-wavelength emitters that are typical of diesel fuels, lubricants, and soaps were observed in seeps and drips near the well casing. Additionally, recharge to the Waterfall Room consistently exhibits a very low, ambient fluorescein peak (515 nm) and produces a distinctive chlorine odor (Raedts and Smart, 2015).

Utilities (particularly stormwater) are not well-documented in Horse Cave, and the management of these features is not apparent (Raedts and Smart, 2015). Thus, four sites in Horse Cave were chosen for dye injection and georeferenced using Collector for ArcGIS (v. 19.0.2). These included a storm drain at the Horse Cave car wash (Fig. 4) that was suggested to discharge at the Waterfall Room (Nims, P., 2018, pers. comm., July 13. Horse Cave, Ky.: ACM), a drainage well located near the concrete mixing plant, and two storm drains near the now-retired Horse Cave Recycling Center. While several sinkholes within the municipality are suitable for dye-tracing, this study focused on infrastructure that has long been questioned by the ACCA.



Figure 4. Horse Cave car wash storm drain.

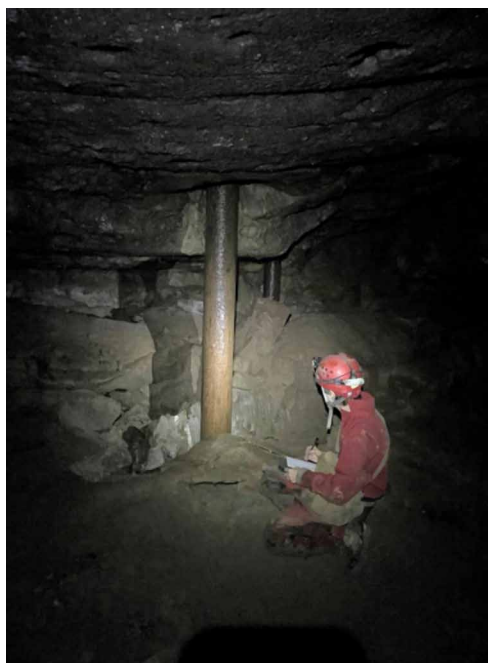


Figure 3. Drainage well casings in the Breakdown Canyon section of Hidden River Cave.

the installation of drainage wells. Among these, two casings are visible in the Breakdown Canyon section of Hidden River Cave (Fig. 3), one of which is inferred to drain wastewater from a concrete mixing plant. This

Each surface and subsurface site was photo-documented and given a unique inventory name and number (Table 1, Fig. 5). Two phases of groundwater dye-tracing occurred during this study; each receptor inventory number corresponds to its respective trace (i.e., the Waterfall Room (003) is denoted 003-1 for Phase I dye-tracing and 003-2 for Phase II dye-tracing).

### Dye-Tracing Procedures

Background fluorescence monitoring occurred before each dye injection to detect dyes used in previous studies, pollutants, or natural compounds with fluorescence properties that may be similar to the dyes used by the Crawford Hydrology Laboratory (CHL) at Western Kentucky University. Dye receptors were installed in the main flow of each site and consisted of five-centimeter mesh bags filled with approximately three grams of activated coconut charcoal. Background monitoring occurred for one week

and drains an area of ~8 km<sup>2</sup> (Quinlan and Rowe, 1977). Wheel River is the primary upstream tributary of Hidden River Cave and is suggested to form the main tributary of the South River (Nims, P., 2018, pers. comm., July 13. Horse Cave, Ky.: ACM) several smaller tributaries and seeps are also suggested to be connected to the South River and recharged via sinkholes. Each of these sites exhibit background fluorescence characteristics similar to optical brighteners and fluorescein (Raedts and Smart, 2015), thus limiting the selection of dyes that can be used for tracing.

Poorly-drained depressions in the city of Horse Cave have been modified by



**Table 1. Dye-tracing feature inventory.**

Dye Injection Sites		Dye Receptor Locations	
Site ID	Location	Site ID	Location
DT1	Horse Cave Car Wash	001	Wheet River
DT2	Injection Well	002	Board Room
DT3	Recycling Center Storm Drain A	003	Waterfall Room
DT4	Recycling Center Storm Drain B	004	Well Casing A
...	...	005	Well Casing B
...	...	006	Well Casing C
...	...	007	Site 007
...	...	008	Breakdown Canyon
...	...	009	South River
...	...	010	East River

before each phase of dye-tracing, after which each dye receptor was rinsed in the respective cave stream to free the sample of any accumulated sediment, carefully placed into a clearly labeled, sealable plastic bag, and stored in a cooler to be transported to the CHL for analysis. New receptors replaced the background samples to prepare for the subsequent dye-traces.

In the laboratory, an eluent consisting of propanol, distilled water, and ammonium hydroxide prepared at a ratio of 5:3:2 was used to extract dye from one gram of charcoal from

each dye receptor; the elutant was then analyzed using synchronous scanning on a Shimadzu RF-6000 spectrofluorometer following established CHL (2016) protocols. The emission spectra of the synchronous scans were plotted on a laser printer, and the results of the analysis were recorded in Excel.

Fluorescent dyes for each trace were chosen based on the analysis and interpretation of background fluorescence spectra. The quantity of dye for each injection was calculated via the following equation as per Aley and Fletcher (1976):

$$W_d = 1.478 \sqrt{\frac{dQ}{v}}, \tag{1}$$

where  $W_d$  represents the weight of the dye to be used (kg),  $d$  represents the distance between injection and receptor sites (km),  $Q$  represents discharge ( $m^3/s$ ), and  $v$  represents stream velocity (m/s).

Dye injection occurred at four sites in the city of Horse Cave, and monitoring occurred for one to two weeks for each phase of dye tracing. After the monitoring period, the receptors were collected, stored, and transported to the laboratory for analysis following the CHL protocols.

**Phase I Dye-Tracing**

Phase I background monitoring occurred on March 9, 2018 and consisted of the placement of nine receptors at all but one site (007). The background receptors were retrieved on March 16, 2018, and a six-dye background analysis was conducted on March 20, 2018 against the standards Tinopal CBS-X (OB, FB351), Fluorescein (FL, AY73), Eosine (EO, AR87), D&C Red 28 (Phloxine B) (R28, AR92), Rhodamine WT (RWT, AR388), and Sulphorhodamine B (SRB, AR52).

Six sites exhibited positive background fluorescence, including the well casings, where OB, FL, R28, and RWT were detected. The Waterfall Room exhibited no significant background concentrations. Thus, RWT was chosen to trace the Horse Cave car wash storm drain (DT1) that was suggested to be associated with recharge to the Waterfall Room, and EO was chosen to trace the drainage well located near the concrete mixing plant (DT2). Phase I dye injection occurred during the evening of April 6, 2018 and included the injection of 0.5 kg of RWT into the car wash storm drain

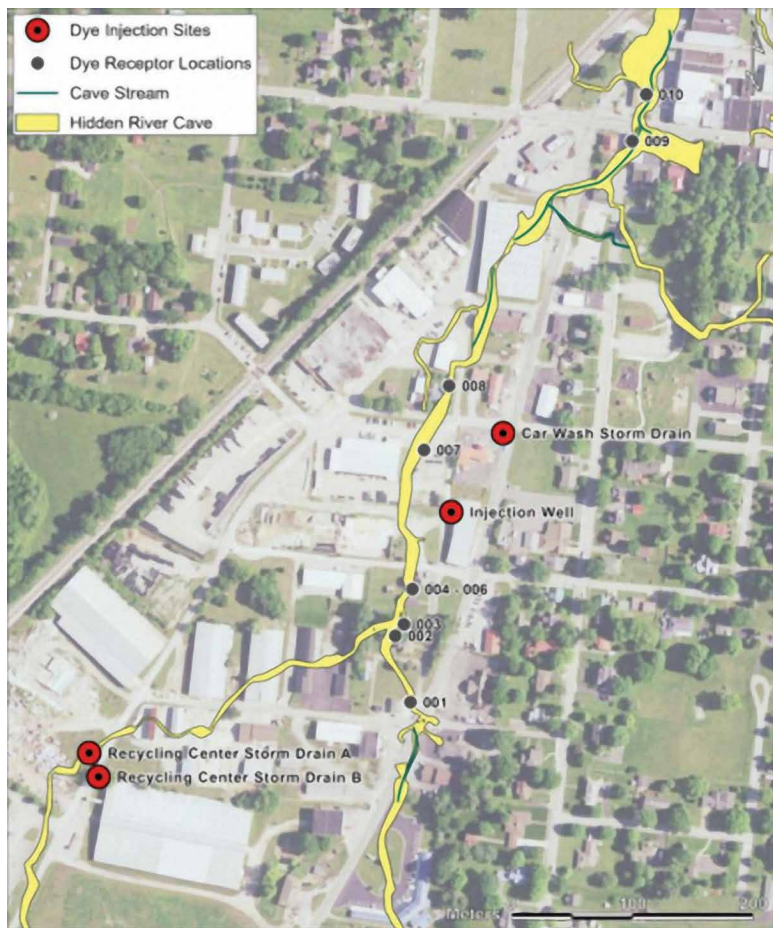


Figure 5. Dye receptor sites in Hidden River Cave and dye injection locations in Horse Cave. Data from the CRF and the KGS.

and 0.3 kg of EO into the drainage well. Both dyes were injected before a rain event to ensure proper flushing. The dye receptors were retrieved on April 20, 2018 and analyzed on April 26, 2018 using CHL protocols.

## Phase II Dye-Tracing

Phase II background monitoring consisted of the placement of 10 receptors on July 20, 2018, which included an additional site in the Breakdown Canyon section (007). The background receptors were retrieved on July 27, 2018, and a five-dye background analysis was conducted on August 1<sup>st</sup> using OB, FL, EO, RWT, and SRB standards.

Four dyes were detected in the background samples, including OB, FL, EO, and RWT. Based on these results and the previous use of EO and RWT, SRB was chosen to trace the Recycling Center Storm Drain A (DT3), and FL was chosen to trace Recycling Center Storm Drain B (DT4). Phase II dye injection occurred on August 3, 2018, and included 0.5 kg of SRB into Recycling Center Storm Drain A and 0.5 kg of FL into Recycling Center Storm Drain B. Both dyes were flushed using a fire truck provided by the Horse Cave fire chief. Dye receptors were retrieved on August 14<sup>th</sup> and analyzed on August 16<sup>th</sup> using the CHL protocols.

## CHARACTERIZATION OF STREAM STAGE

Two Onset HOBO pressure transducers (model U20L-02) were installed in Hidden River Cave on June 10, 2018, to collect high-resolution stage data after flooding events occurred that limited accessibility to Hidden River Cave. The transducers were installed in PVC stilling wells near the Kneebuster tributary in the South River and at the Thomas Boardwalk in the East River to characterize stream responses to precipitation events until September 29, 2018. Each sonde collected five-minute resolution water-level data, except when briefly pulled to download the data; due to an error in deployment, the East River sonde excludes data from Julian dates 180 to 201. The stage data were processed using Onset HOBOWare Pro (v. 3.7.15), which incorporated water level reference readings and barometric pressure compensation data that were recorded at the time of each data download. The processed stage data were organized in Excel, graphed using SigmaPlot (v. 11.0), and compared to five-minute precipitation data acquired from the Kentucky Mesonet HDYV monitoring station located in Munfordville (<https://www.kymesonet.org/>).

## LAND-USE OVER THE HIDDEN RIVER GROUNDWATER SUBBASIN

Changes in land-use over the Hidden River groundwater subbasin between 1989 and 2017 were determined using supervised classification in ArcGIS Pro (v. 2.2) and 30 × 30 m Landsat 5 (10/22/1989) and Landsat 8 (09/26/2017) multispectral imagery obtained from the United States Geological Survey (USGS) Global Visualization Viewer (GloVis) (<https://glovis.usgs.gov>). The scope of the land-use analysis was broadened to include the entire Hidden River groundwater subbasin, as changing land-use in other areas of the subbasin could negatively impact overall recharge. Additionally, because most of Hart County's industry is located in Horse Cave (HCCC, 2013), this time frame was chosen based on the 28-year gap that exists between the publications of the respective City of Horse Cave zoning ordinances.

The study area included a feature class of the Gorin Mill groundwater basin collected from the Kentucky Geological Survey (KGS) that was modified to represent the associated Hidden River groundwater subbasin according to the extent defined by Ray and Currens (1998). Using the Hidden River groundwater subbasin feature class and the Clip tool in ArcGIS Pro, both images from GloVis were clipped to the subbasin boundaries. A qualitative analysis comparing the 1989 and 2017 imagery was conducted during supervised classification, which included creating training samples, reclassifying the imagery, and performing post-classification processing on both images. The results of the reclassification were then compared quantitatively by determining the percentage of land-use classes for each image and an assessment was conducted to determine the accuracy of the classification method used.

Supervised classification was conducted for each image using the Classification Wizard in ArcGIS Pro, and training samples (Fig. 6) were created using the Training Samples Manager and schema provided by the USGS 2011 National Land Cover Dataset (NLCD), which includes the following land-use classes: (1) water, (2) developed, (3) forest, and (4) agriculture. Reclassified rasters were generated from the training samples. Post-classification processing was then applied to the reclassified images by using generalization tools, which remove the noise that is created by isolated pixels or small, misclassified regions and automates the assignment of more reliable values; the Majority Filter tool removed isolated pixels from the reclassified raster, and the Boundary Clean tool smoothed the

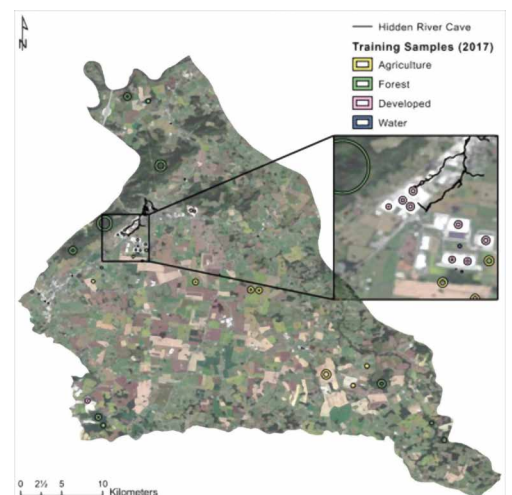


Figure 6. Example of training samples created from the 2017 Landsat 8 imagery used to perform supervised classification. Data from GloVis and the USGS 2011 NLCD (<https://www.usgs.gov/centers/eros/science/national-land-cover-database>).



class boundary edges and grouped the classes to produce more organized imagery (Keranen and Kolvoord, 2014).

To determine the percentages of land cover types, a new field named Percent was added to the attribute table of each reclassified raster and populated via the Field Calculator tool; for each land-use category, the total number of pixels in the respective reclassified image (determined using the Summary Statistics tool) was divided by the number of pixels representing that category and multiplied by 100. These data were used to assess the approximate percentages of land-use change over the Hidden River groundwater subbasin between 1989 and 2017.

### Accuracy Assessment of Supervised Classification

To determine the accuracy of the performed supervised classification, the errors of omission (features that have been excluded from the reclassified imagery that exist) and commission (features that do not exist that have been included in the reclassified imagery) were calculated by generating an error matrix from ground-truthed data, which compares the organized, reclassified imagery to higher resolution aerial imagery (Keranen and Kolvoord, 2014).

Twenty-five points were randomly generated for each image using the Create Random Points tool. Because the reclassified image resolution is  $30 \times 30$  m, a 30-meter buffer was created around the random points to represent the approximate area that a single pixel spans (Fig. 7). The reclassified imagery was then compared to 2016 Kentucky statewide 0.5 m aerial imagery that was downloaded from the Kentucky Division of Geographic Information to ground-truth land cover within the buffer boundaries. Note that high-resolution 1989 imagery was not available; thus, generalizations were made by analyzing the Landsat 5 multispectral imagery in conjunction with the 2016 Kentucky statewide 0.5 m aerial imagery.

A new field was added to the random point feature class called GT (ground-truth) to record the correct type of land-use within the buffer according to the high-resolution imagery. Upon completion of ground-truthing, the Extract Values to Points tool was used on each of the reclassified images, which extracted the land-use values that the random points represented and added them to the attribute table of the Random Point feature class. The final attribute table included the ground-truthed values and the values determined by supervised classification, which were compared to determine the accuracy of the classification method used. An error matrix was constructed using the Select by Attributes tool to identify matching classifications. For example, to determine the number of points that were classified as water (1), the following query was used:

“GT 2017” = 1 AND “Supervised 2017” = 1

The same query was used to determine each corresponding land-use type for both images. From these data, the total classification accuracy percentages were calculated to determine the errors of omission and commission.

## RESULTS AND DISCUSSION

### Phase I and II Dye-tracing

During Phase I dye-tracing, it was anticipated that EO would discharge from drips and seeps surrounding Well Casing B (005-1) due to the suspected age and potential degradation of the well casing and that RWT would discharge at the Waterfall Room (003-1). Conversely, a high concentration of EO was detected at the Waterfall Room rather than RWT (Table 2); EO appeared to bypass the well casings and was detected again at the Breakdown Canyon entrance (008-1), the South River (009-1), and the East River (010-1). No dye was recovered at Well Casing B and, although a direct connection cannot be confirmed, a higher concentration of dye was detected at Well Casing A (004-1) than what the results of background fluorescence analysis determined. Further, the peak center associated with Well Casing A is more indicative of R28 than the recovery of RWT from the Horse Cave car wash storm drain (DT1); thus, 004-1 was considered a questionable positive. Like EO, a significant concentration of RWT was ultimately detected at the Breakdown Canyon entrance and beyond.

Because consideration was not made of RWT potentially being detected at the well casings, and the peak center for RWT and R28 are relatively similar, another trace should be conducted at the drainage well located near the concrete mixing plant (DT2) using a different dye, such as SRB. Alternatively, radiolocation can be used to determine the precise location of the well casing in relation to the surface, as few data exist regarding its installation and ownership (KGS, 1997). It is possible that the well casing seen on the surface is unrelated to either of those seen in the subsurface.

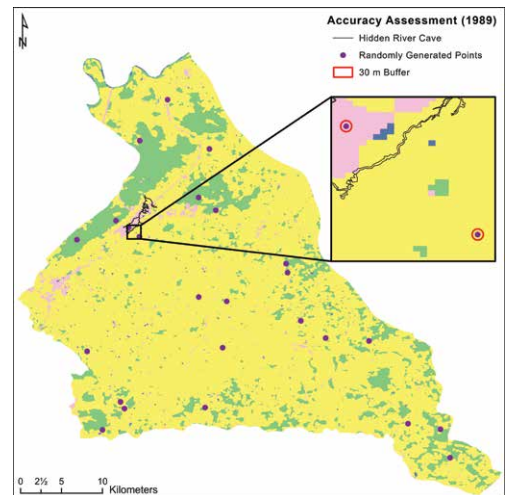


Figure 7. Example of random point generation; a 30 m buffer was created around each point to ground-truth the land cover type within the buffer. Data from GloVis and the USGS 2011 NLCD.

**Table 2. Results of Phase I dye-tracing.**

Feature ID	Eosine			Rhodamine WT		
	Result <sup>a</sup>	Conc., ppb	Peak Ctr., nm	Result <sup>a</sup>	Conc., ppb	Peak Ctr., nm
Waterfall Room (003-1)	+++	222.266	542.2	...	...	...
Well Casing A (004-1)	...	...	...	?+	5.828	564.6
Breakdown Canyon (008-1)	+++	14.962	542.2	++	8.290	568.4
South River (009-1)	+++	9.172	542.4	++	6.020	568.2
East River (010-1)	++	0.692	542.2	+	0.258	567.4

<sup>a</sup> ++ = Positive (10 times background or lowest detection limit)  
 ++ = Very positive (100 times background or lowest detection limit)  
 +++ = Extremely positive (1,000 times background or lowest detection limit)  
 ?+ = Questionable Positive

This inference is based on the misalignment of the GPS data used to georeference the well casing with respect to the approximate locations of the casings in the cave (Osborne, 2018). Therefore, future investigations should consider collecting high-accuracy GPS data and georeferencing the cave to confirm its locational accuracy.

It is unknown where the dyes used for Phase I tracing discharged from their respective injection sites or where water is flowing between the Waterfall Room (003) and the Breakdown Canyon entrance (008). An orange tint was detected at a pool in the Kneebuster tributary (Nims, P., 2018, pers. comm., July 13. Horse Cave, Ky.: ACM), which was not included in the dye-tracing procedures herein. This observation, however, is not surprising, as a small, neighboring tributary exists that connects the headwaters of the South River and the Kneebuster passage, known as Blind Fish Alley (Fig. 2). Concentrated RWT was also observed by the American Cave Museum (ACM) staff at Site 007; however, because the passage was unknown to the author before Phase I dye-tracing, a receptor was not placed there. This red pool, as well as an orange tint to the cascade in the Waterfall Room, was observed less than one day after Phase I dye injection took place (Russell, G., 2018. Pers. comm., May 2. Horse Cave, Ky.: ACM.)

In Phase II dye-tracing, FL and SRB were only detected at the South River (009-2) and the East River (010-2) (Table 3). A much higher concentration of each dye was detected at the South River site. Based on these results, other, concealed groundwater flow paths likely exist beneath the Breakdown Canyon section or in tributaries that lie outside of the known cave boundaries that ultimately discharge to the South River. The South River also could have been an outlet for more dye, either because it is a more direct route from the injection location, it experienced more flow during the monitoring period, or because the flow patterns at the South River where the receptor was deployed were ideal (or a combination of these possibilities). It is also possible that the East River headwaters effectively diluted the dye traveling from 009-2 to 010-2, resulting in lower dye concentrations.

The results of background fluorescence analyses conducted by Raedts and Smart (2015) determined that some tributaries in the cave exhibited consistent spectra. Indeed, the spectra seen during this study from sites such as Wheat River, the Waterfall Room, and the South and East Rivers align with their results. Several other sites in the city of Horse Cave (i.e., the Horse Cave laundromat, sinkholes, catchment basins, etc.) and Hidden River Cave (i.e., the Kneebuster tributary and upstream East River) should be the focus of future dye-tracing investigations. In-cave dye-tracing should also occur to confirm the implied connections between sites such as Wheat River, the Breakdown Canyon entrance, and the South River. Further, using the Hydrology toolset in ArcGIS Pro, the collective dye-traces conducted within the Hidden River groundwater subbasin could be modeled to develop more accurate, rather than inferred, groundwater flow paths. An interactive, visual model can provide a relatively simple way for the ACM to further convey to the public the importance of groundwater protection in karst regions.

The dye-tracing conducted herein also supported Raedts and Smart's (2015) suggestion that acute, point-source contamination events are linked to land-use practices in Horse Cave, as all dyes were detected in Hidden River Cave (Fig. 8). While qualitative dye-tracing does not provide the parameters that are necessary to determine the time of travel of recharge from drainage features on the surface to the cave, it does establish benchmark data that can be coupled

**Table 3. Results of Phase II dye-tracing.**

Feature ID	Fluorescein			Sulphorhodamine B		
	Result <sup>a</sup>	Conc., ppb	Peak Ctr., nm	Result <sup>a</sup>	Conc., ppb	Peak Ctr., nm
South River (009-2)	+++	277.419	518.4	+++	23.556	579.4
East River (010-2)	++	3.907	517.4	++	1.484	578.0

<sup>a</sup> ++ = Very positive (100 times background or lowest detection limit)  
 +++ = Extremely positive (1,000 times background or lowest detection limit)

with stream stage analyses to generalize the seemingly abrupt nature of recharge based on the aforementioned observations made by the ACM staff.

### Characterization of Stream Stage

This study establishes the first recorded, high-resolution flow conditions in Hidden River Cave, which are critical for assessing the rate at which contaminants may enter the cave system. Cave stream responsiveness to four major precipitation events was analyzed using five-minute resolution precipitation data acquired from the Kentucky Mesonet HDYV monitoring station in Munfordville. Scattered thunderstorm events occurred from Julian date (JD) 176 to JD 179 and produced the highest rainfall values during this study (Fig. 9). The approximate baselevel conditions (determined by average minimum stage values) were met on JD 182 (three days after the final precipitation event). A series of four precipitation events occurred from JD 228 to JD 233 that caused subsequent peaks in each stream; a steady decline in stage occurred over nearly a week, although neither stream achieved baselevel conditions. Stage response from Tropical Storm Gordon (<https://www.weather.gov/mob/gordon>) is evident from JD 251 to JD 252. Water levels returned to near baseflow conditions on JD 256, four days after precipitation ended. The most significant storm event during this study occurred during the fall season's first major cold front, which brought rainfall from JD 264 to JD 267. Return to baseflow was not determined for this event due to time constraints. Overall, the East River produced higher stage values than the South River.

The flashy nature of the streams exhibited in the hydrograph is indicative of low storage, high transmissivity, and rapid drainage (Murdoch et al., 2016). Although this study occurred over a short period, the HOBO pressure transducers that were installed at the South and East Rivers provide important data to assess cave stream responsiveness to precipitation events to identify possible contaminant transport scenarios and for flood prediction.

Stage at the South River appeared to respond to precipitation events (and recede) more quickly than at the East River. Significant peaks in the East River hydrograph occur approximately thirty minutes after peak flow occurs at the South River; however, when the East River experienced recharge from sustained precipitation, response times were similar to those observed in the South River. Except for antecedent precipitation, the South River responds within 40 minutes to one hour, while the East River takes longer (approximately 1-1.5 hours). Additionally, except for sustained precipitation (i.e., from JD 228 to JD 233), it appears to take three to four days for both streams to recede to baselevel conditions after precipitation events end. Baselevel conditions were not met for the precipitation events that occurred from JD 228 to JD 233 before precipitation began again upon the arrival of Tropical Storm Gordon, although water recession occurred over nearly a week, aligning with Fiorillo's (2016) suggestion that hydrograph recession can occur over several days. These differing response times are likely indicative of the streams' respective catchment sizes, variations in matrix permeability and porosity (i.e., diffuse vs. conduit flow), storage, or karstification of the cave system (or a combination of these), as well as either inactive tributaries during low flow or the diversion of flow via increased discharge during precipitation events.

The stage data herein can serve as a benchmark to supplement future high-resolution hydrologic studies in Hidden River Cave. Future investigations should consider discharge at the South and East Rivers, as well as Wheel River, the Waterfall Room (where a funnel system, as exemplified by Groves et al. (2013), could be constructed), and the Breakdown Canyon entrance. Discharge data, coupled with in-cave dye-tracing that was previously suggested, can characterize the differences in volumetric flow between Wheel River, the Breakdown Canyon entrance, and the South River, as they are inferred to be hydrologically connected to one another. Additionally, discharge data coupled with quantitative dye-tracing can provide details about the fate and transport of contaminants (Li et al., 2016; Murdoch et al., 2016; Jiang et al., 2018), and hydrochemical analyses can be used to characterize the epikarst in Hidden River Cave and systematically monitor groundwater quality (Ryan and Meiman, 1996; Groves et al., 2013; Knierim et al., 2015;

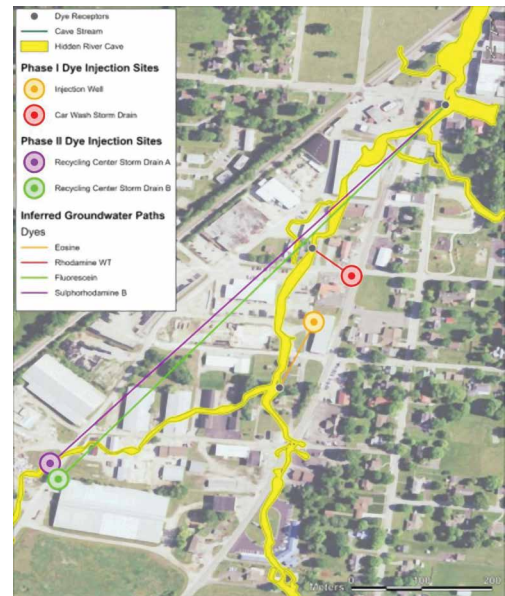


Figure 8. Inferred groundwater flow paths determined by Phase I and II dye-tracing. Data from CRF and KGS.

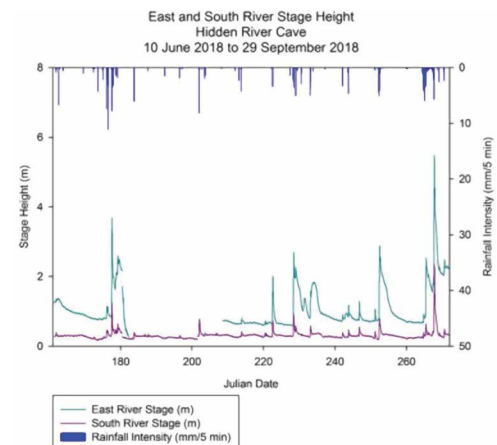


Figure 9. South River and East River stage responses to precipitation from June 10 to September 29, 2018. Data analyzed in SigmaPlot (11.0).



Schreiber et al., 2015), parameters that have not yet been examined. Thus, it is important to understand the type and extent of infrastructural land-use over the Hidden River groundwater basin, as the impermeable nature of development often increases runoff and, consequently, contaminant transport in tributary catchments (Jiang et al., 2018).

### Land-use over the Hidden River Groundwater Subbasin

Hidden River Cave is a case study example of the complexity of the relationship between urban land-use and recharge areas, such as those demonstrated by the dye-tracing herein. Thus, the entire Hidden River groundwater subbasin was examined to assess regional land-use that may further impact the groundwater system outside the main developed area of Horse Cave. Except for agricultural areas, all land-use types over the Hidden River groundwater subbasin have increased since 1989. Developed areas are arguably the most important to analyze for the purposes of this study, as they directly affect Hidden River Cave, according to the dye-tracing results herein. Supervised classification determined that development over the Hidden River groundwater subbasin increased by 7 % between 1989 and 2017 (Fig. 10). While developed areas do not make up the dominant land-cover type, they are critical to understand based on the history of groundwater contamination in this region and the current, discrete contamination events that have occurred since remediation began in 1989.

While agricultural areas decreased by 25 % since 1989, forested areas increased by 17.7 %. It is possible that more agricultural land was converted to forest after several events, such as abandonment, ownership conversion, or restoration efforts. A 0.6 % increase in water can also be seen; however, several discrepancies exist between land-use types, which can be attributed to the lower resolution (30 × 30 m) imagery. For example, water bodies tend to appear either varying shades of green or brown and therefore contain similar reflectance values as agricultural, forested, and industrial areas (as some industrial buildings have green roofs). In the reclassified 2017 imagery, water appears to surround developed areas in Horse Cave; future land-use investigations should consider the occurrence of sinkholes and the amount of precipitation the study area received during the time imagery was taken, as well as the development of catchment basins, such as Creacy Lake.

Using U.S. Census data, population changes over time could shed light on the potentially increased stress that may be imposed on the utilities in Horse Cave (Knierim et al., 2015; Denizman, 2018). Specifically, sewage utilities and the percentage of the population that relies on septic systems should be assessed, as Raedts and Smart (2015) discovered sections of the cave that exhibited fluorescence peaks characteristic of optical brighteners found in raw sewage. Additionally, many rural parts of Kentucky are home to concentrated animal feeding operations (CAFOs), which commonly are not considered risks to karst groundwater (Brahana et al., 2014; Knierim et al., 2015; Murdoch et al., 2016; Tagne and Dowling, 2018). Thus, CAFOs and other agricultural enterprises in Hart County should be included in future land-use analyses.

### Accuracy Assessment of Supervised Classification

An accuracy assessment was conducted by comparing the results of the reclassified 1989 Landsat 5 TM and the 2017 Landsat 8 aerial imagery to ground-truthed data using 2016 Kentucky state wide 0.5 m aerial imagery. Overall accuracy was calculated by dividing the number of correct pixels in the error matrix (the sum of the diagonal) by the total number of pixels. Additionally, the errors of commission (column total) and omission (row total) were calculated by dividing the number of correct pixels in a land-use category by the total number of pixels in that category (Tables 4 and 5).

Results revealed that the reclassified 1989 aerial imagery produced a slightly lower accuracy than the results of the 2017 imagery when compared to ground-truthed data, although these percentages reflect that the supervised classification conducted herein produced relatively accurate results. It is important to note, however, that the classification method used does not account for all of the infrastructure within the study area. For example, the road that dissects the study area consists of pixels that represent all types of land-use rather than a solely developed feature. Thus, these percentages do not reflect all development, but they differ enough to conclude that development has increased.

Developed areas can significantly modify the natural processes of subsurface recharge via features such as impermeable surfaces (i.e., parking lots and landfills) and utility networks (Zhou, 2007). Modern construction typically includes extensive paving over the natural soil surface, which can effectively decrease local recharge by lessening percolation areas while simultaneously increasing the amount of surface runoff to otherwise relatively inactive parts

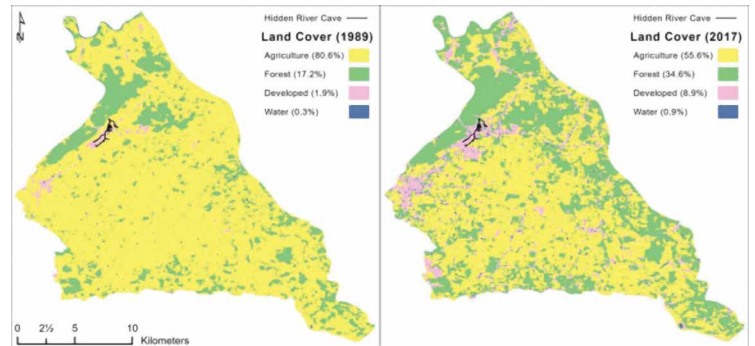


Figure 10. Comparison of the reclassified 1989 and 2017 aerial imagery. Data from GloVis, USGS 2011 NLCD, CRF, and KDGI.



**Table 4. Accuracy assessment of the reclassified 1989 Landsat 5 TM imagery.**

Classified Category	Actual Category: Ground-Truth				Total	Error of Commission, %
	Water	Developed	Forest	Agriculture		
Water	0	0	0	0	0	0
Developed	0	1	0	0	1	100
Forest	0	0	6	0	6	100
Agriculture	1	0	3	14	18	77.7
Total	1	1	9	14	25	...
Error of Omission, %	0	100	66.7	100	...	...
Overall Accuracy, %	84	...	...	...	...	...

Note: errors of commission (column total) and omission (row total) were calculated by dividing the number of correct pixels in a land-use category by the total number of pixels in that category and multiplying the quotient by 100 to obtain a percentage. Overall accuracy was calculated by dividing the number of correct pixels in the error matrix (the sum of the diagonal) by the total number of pixels.

**Table 5. Accuracy assessment of the reclassified 2017 Landsat 8 imagery.**

Classified Category	Actual Category: Ground-Truth				Total	Error of Commission, %
	Water	Developed	Forest	Agriculture		
Water	1	0	0	0	1	100
Developed	0	4	0	0	3	100
Forest	0	0	7	3	11	63.6
Agriculture	0	0	0	10	10	100
Total	1	4	7	13	25	...
Error of Omission, %	100	100	100	76.9	...	...
Overall Accuracy, %	88	...	...	...	...	...

Note: errors of commission (column total) and omission (row total) were calculated by dividing the number of correct pixels in a land-use category by the total number of pixels in that category and multiplying the quotient by 100 to obtain a percentage. Overall accuracy was calculated by dividing the number of correct pixels in the error matrix (the sum of the diagonal) by the total number of pixels.

of the groundwater system (Jiang et al., 2018). Indeed, most of the explored cave system is covered by development (Fig. 10), the impervious nature of which has likely altered the natural recharge and discharge mechanics of the Hidden River groundwater subbasin. Further, stormwater discharge from development sites does not appear to be effectively regulated in Hart County. Thus, the suggested potential for mitigating further contamination of the Hidden River groundwater subbasin through the techniques used in this research can be supplemented by examining the existing policies regarding stormwater discharge regulations in karst regions at national, state, and local levels.

### Implications for Karst Stormwater Regulations

Numerous studies exist that provide the scientific basis to support the need for improved groundwater management in transboundary karst regions (Marín et al., 2000; Escolero, 2002; Bauer-Gottwein et al., 2011; Christenson et al., 2011; Nedvidek, 2014; Ravbar and Šebela, 2015; Stevanović et al., 2016; Castro, 2017; Turpaud et al., 2018). A prevalent theme, however, is the lack of the implementation of such practices (Fleury, 2009; Richardson, 2018).

Except for the management of federally-owned land, where laws such as the Endangered Species Act (1973) and the Federal Cave Resources Protection Act (1988) indirectly protect karst resources, the U.S. federal government is limited in its authority to address concerns related to groundwater quality in karst regions. For example, the Clean Water Act (1972), including the National Pollutant Discharge Elimination System (NPDES) permit program, only protects against the contamination of surface waters (EPA, 2019), and the Safe Drinking Water Act (1974) mentions groundwater but regulates only those karst areas that contain sole-source aquifers (Nedvidek, 2014; Richardson, 2018). Rather, state governments and, to the extent granted by the state, local governments hold the primary authority to regulate groundwater, although this is often not conducted in a meaningful way (Fleury, 2009).

In Kentucky, policies regarding stormwater discharge are contained in Title 401, Chapter 5 of the Kentucky Administrative Regulations (KGA, 2020). The Kentucky Pollutant Discharge Elimination System (KPDES), the state-administered version of the NPDES, requires operators to obtain a permit and create a Stormwater Pollution Prevention Plan (SWPPP) for proposed development. The KPDES implements the six Minimum Control Measures (MCMs) outlined in

Phase II (1998) of the federal NPDES permit program (EPA, 2018) but fails to address regulations that are specific to the karst landscape that makes the state unique. These six MCMs rely heavily on education and quality BMP development. Indeed, a plethora of educational resources and public outreach programs exist in Kentucky that reiterate the importance of protecting karst waters; however, relying solely on education and BMPs (the effectiveness of which are rarely measured) dismisses the opportunity to collect quantitative data from the systematic groundwater monitoring that is necessary for the protection of karst waters (Taylor et al., 2007; Nedvidek, 2014).

In the Hart County Comprehensive Plan, recognition of the karst topography of Hart County and adequate storm-water drainage for development projects is included under the Land Use and Development Objectives (HCPC, 2020, p. 14); however, a foundational management plan is not provided to reinforce these objectives. More specifically, storm-water management is addressed in Articles 10 and 18 of the Hart County Planning Commission's Subdivision Regulations (HCPC, 2007). Similar to the state's SWPPP, the Hart County Planning Commission requires a Storm Water Management Plan (SWMP) for development; here, sinkholes, the only mention of a karst-related feature, are required to be identified, but no formal structure exists for regulating stormwater discharge to these features.

As aforementioned, the City of Horse Cave Zoning Ordinance (CoHC, 2017) which adheres to and references the Hart County Planning Commission's Subdivision Regulations, had not been updated from 1989 (CoHC, 1989) until 2017. Few improvements have been made since 1989; similar to the subdivision regulations, the impacts that development may have on groundwater are not addressed or properly mitigated. Further, all three documents briefly mention karst in the form of regulating development near sinkholes. Setbacks are required around sinkholes, as they "shall be preserved in their natural state to provide drainage to the surrounding area" (HCPC, 2007, p. 41); yet, there is no requirement for monitoring said drainage.

Perhaps the most significant improvement to the 2017 City Zoning Ordinance is the associated map that was created by the Barren River Area Development District using ArcGIS Online (BRADD, 2017). This map provides significant detail compared to that of the 1989 zoning ordinance, but the fact that it was not created by either Hart County or the City of Horse Cave emphasizes their need for GIS. County or city employees can adopt GIS practices using either open-source (i.e., QGIS) or closed-source (i.e., Esri) GIS software, where an inventory of utilities and drainage wells could be developed. Collaboration with GIS software providers can also implement free or relatively inexpensive software training to build and upkeep such an inventory. Additionally, the option to download open-source data from local, state, and federal organizations provides a unique opportunity to complete various cost-effective, broad-scale analyses in GIS (Wilson and Rocha, 2016).

The City of Bowling Green, Kentucky, in collaboration with Western Kentucky University, has developed an inventory of stormwater drainage features that are maintained in a GIS, and they have effectively raised the bar in terms of establishing an efficient stormwater monitoring program (<https://www.underbgky.org/>). Nedvidek (2014) explained that city officials in Bowling Green are aware of the importance of these data for establishing broad-scale permit compliance and producing benchmark data to implement regulations regarding stormwater discharge to karst groundwater. A partnership such as this between the City of Horse Cave and the ACCA could establish an agenda to systematically monitor stormwater discharge to groundwater, especially since the ACCA has existing partnerships with institutions that provide grant opportunities for research (i.e., the Cleveland Grotto, Western Kentucky University, the University of Western Ontario, McMaster's University, etc.). Additionally, Horse Cave's proximity to Mammoth Cave National Park and the City of Bowling Green provides avenues for further collaboration.

Several studies have produced benchmark data that suggests the need for improved management of the Hidden River groundwater subbasin (Quinlan and Rowe, 1977; Quinlan and Ewers, 1989; Lewis, 1995; Raedts and Smart, 2015; Broderick et al., 2017; Osborne, 2018; Feist et al., 2020). The following recommendations, based on the results of the analyses herein, can also be used to further protect the Hidden River groundwater subbasin.

- Hart County and/or the cities within Hart County should consider implementing an organizational GIS using either open-source or closed-source GIS software, and training services should be provided to employees for the creation and maintenance of a geodatabase containing a detailed inventory of utilities, wells, and karst features;
  - Benchmark data from local studies should be synthesized and, where applicable, added to a geodatabase;
  - Exploration and data collection should continue at L&N Cave and the Hidden River Complex;
- The City of Horse Cave zoning ordinance should be regularly revised (i.e., annually or bi-annually) and should consider the local geology, including the maturity of the Pennyroyal Plateau, to make more informed decisions regarding development;
- The City of Horse Cave should form partnerships with the ACCA, Mammoth Cave National Park, nearby municipalities (i.e., Bowling Green, Park City, Cave City, etc.), universities, and caving organizations to establish and enforce more effective regulations regarding stormwater discharge to groundwater;

- Planning and development documents in Hart County should include stormwater discharge policies that are specific to the protection of karst groundwater;
  - Stormwater discharge regulations in Hart County should surpass those established by the KPDES;
  - The regional karst groundwater basins and their respective subbasins should be acknowledged by the officials that create and enforce development ordinances and by development operators;
  - SWMPs should require systematic water quality monitoring (i.e., greater than quarterly) at discharge areas such as Gorin Mill Spring to measure the performance of BMPs set forth by the site operator.

## CONCLUSIONS

An integrative approach, which can be applied to other transboundary karst regions, combined groundwater dye-tracing, high-resolution stage data collection, and remote sensing analysis in a GIS to assess land-use impacts on the hydrology of the Hidden River groundwater subbasin.

Groundwater dye-tracing confirmed that stormwater infrastructure in Horse Cave discharges to Hidden River Cave and, subsequently, to the Hidden River groundwater subbasin, as each of the dyes used during this study were recovered. High-resolution stage data determined that the major trunk streams of Hidden River Cave respond to precipitation events approximately 40 minutes to 1.5 hours after they begin; except for sustained precipitation, baselevel conditions are reached three to four days after precipitation ends. These data and the aforementioned observations of dye made by the ACM staff less than one day after dye injection occurred imply that recharge to Hidden River Cave is relatively abrupt. Thus, the rate at which contaminants enter and traverse the subsurface is likely also abrupt.

Supervised classification in ArcGIS Pro using 30 × 30 m multispectral imagery from the USGS characterized changes in land-use over the Hidden River groundwater subbasin from 1989 to 2017. Development is largely concentrated in Horse Cave and has increased by approximately 7 % between 1989 and 2017, suggesting an increase in impervious surfaces, which can significantly alter the natural recharge and discharge mechanics of the subbasin and introduce a higher volume of contaminants. Additionally, weaknesses were identified in the current stormwater management regulations at the U.S. federal, state, and local levels, where the sparsity or absence of karst-specific regulations suggests either the improvement or implementation of such regulations.

Hidden River Cave serves as an important economic and cultural resource for Horse Cave and the wider region. This research supplements prior studies and addresses gaps in the literature by evaluating land-use and recharge relationships at a local, rather than regional, scale, as most of the commercial development within the boundaries of the Hidden River groundwater subbasin lies over Hidden River Cave. It also demonstrates the important contribution of localized groundwater investigations to broader karst management and sustainable development planning, including for policy development toward water resource protection.

## ACKNOWLEDGMENTS

This work was supported by the Graduate Student Research Committee at Western Kentucky University under Grant number 221531 and the Cleveland Grotto Science Fund. Special thanks to Dave Foster for allowing me to conduct research freely in Hidden River Cave, to the staff at the American Cave Museum and my friends Peggy, Steve, and Chelsea, whose knowledge of the cave contributed greatly to this work, and to the Horse Cave fire chief for flushing my dye during the peak of summer. The research herein is very dear to me, and it is my hope that future generations will continue to work toward creating a pristine environment for Hidden River Cave. Not only does this research support the goals of the American Cave Conservation Association, but also the overall conservation and preservation of karst landscapes.

This work is dedicated to J.F. Quinlan – his work in the south-central Kentucky karst region was phenomenal, and his legacy continues through this research.

## REFERENCES

- Aley, T., and Fletcher, M.W., 1976, The Water Tracer's Cookbook: Missouri Speleology, v. 16, no. 6, p. 1–32.
- Bauer-Gottwein, P., Gondwe, B.R.N., Charvet, G., Marín, L.E., Rebolledo-Vieyra, M., and Merediz-Alonso, G., 2011, The Yucatán Peninsula Karst Aquifer, Mexico: Hydrogeology Journal, v. 19, no. 3, p. 507–524, <https://doi.org/10.1007/s10040-010-0699-5>.
- Blair, R.J., Ray, J.A., O'dell, P.W., Marbert, B.S., and Goodmann, P.T., 2012, Integrated surface water and groundwater assessment of large springs in the Green River Basin (BMU4, Round 2), Kentucky Division of Water: <https://eec.ky.gov/Environmental-Protection/Water/Reports/Reports/NPS0503-BMU4R2.pdf>, [accessed Dec. 20, 2017].
- BRADD (Barren River Area Development District), 2017, Horse Cave Zoning Information; <https://bradd-ky.maps.arcgis.com/apps/Information-Lookup/index.html?appid=5e263aca436c4e3699a02a9f3c0ec9>, [accessed Oct. 24, 2018].
- Brahana, V., Nix, J., Bitting, C., Bitting, C., Quick, R., Murdoch, J., Roland, V., West, A., Robertson, S., Scarsdale, G., and North, V., 2014, CAFOs on Karst – Meaningful data collection to adequately define environmental risk, with a specific application from the Southern Ozarks of Northern Arkansas: U.S. Geological Survey, Scientific Investigations Report 5035, 10 p.
- Broderick, C.A., Wicks, C.M., and Taylor, R.L., 2017, Testing the effectiveness of beryllium-7 as a tracer of the movement of sediment over short periods along a cave stream in Hidden River Cave, Kentucky U.S.A.: Journal of Cave and Karst Studies, v. 79, no. 2, p. 84–88, <https://doi.org/10.4311/2016ES0115>.

- Castro, R.B.P., 2017, Statistical analysis of karst aquifer pollution, Karst Flow Model validation at laboratory scale, and development of seepage meter: [Ph.D. dissertation]: Tallahassee, Florida State University, 101 p.
- CHL (Crawford Hydrology Laboratory), 2016, Standard Operating Procedures: Bowling Green, Crawford Hydrology Laboratory, 80 p.
- Christenson, S., Osborn, N.I., Neel, C.R., Faith, J.R., Blome, C.D., Puckette, J., and Pantea, M.P., 2011, Hydrogeology and Simulation of Groundwater Flow in the Arbuckle-Simpson Aquifer, South-Central Oklahoma: U.S. Geological Survey, Scientific Investigations Report 2011-5029, 104 p., <https://doi.org/10.3133/sir20115029>.
- CoHC (City of Horse Cave), 1989, Zoning Ordinance: City of Horse Cave, Kentucky, <https://www.horsecaveky.com/Zoning%20Ordinance-1.pdf>, [accessed Oct. 24, 2018].
- CoHC (City of Horse Cave), 2017, 2017 City Zoning Ordinance: <https://www.horsecaveky.com/Zoning%20Ordinance-2017-1.pdf>, [accessed Oct. 24, 2018].
- Denizman, C., 2018, Land-use changes and groundwater quality in Florida: Applied Water Science, v. 8, no. 5, Article 134, <https://doi.org/10.1007/s13201-018-0776-9>.
- EPA (U.S. Environmental Protection Agency), 1981, Final Environmental Impact Statement for Mammoth Cave Area, Kentucky, Waste Water Facilities: U.S. EPA, 904/9-81-076, 156 p.
- EPA (U.S. Environmental Protection Agency), 2018, Stormwater Phase II Final Rule Fact Sheet Series: <https://www.epa.gov/npdes/stormwater-phase-ii-final-rule-fact-sheet-series>, [accessed Oct. 16, 2020].
- EPA (U.S. Environmental Protection Agency), 2019, EPA Interpretive Statement on the Application of the NPDES Program to Releases of Pollutants from Point Source to Groundwater: [https://www.epa.gov/sites/production/files/2019-04/documents/interpretative\\_statement\\_fact-sheet\\_41519.pdf](https://www.epa.gov/sites/production/files/2019-04/documents/interpretative_statement_fact-sheet_41519.pdf), [accessed Oct. 16, 2020].
- Escolero, O.A., Marin, L.E., Steinich, B., Pacheco, A.J., Cabrera, S.A., and Alcocer, J., 2002, Development of a protection strategy of karst limestone aquifers: The Merida Yucatan, Mexico Case Study: Water Resources Management, v. 16, no. 5, p. 351–367, <https://doi.org/10.1023/A:1021967909293>.
- Feist, S.K., Maclachlan, J.C., Reinhardt, E.G., and Skelding, H.S., 2020, Anthropogenic events captured within sediment in Hidden River Cave, Kentucky: Quaternary Science Advances, v. 1, no. 100001, <https://doi.org/10.1016/j.qsa.2020.100001>.
- Fiorillo, F., 2016, Spring hydrograph recession: A brief review focused on karst aquifers: *in* Stevanović, Z., Krešić, N., and Kukurić, N., eds., Karst without Boundaries: Boca Raton, CRC Press, V. 23, p. 117–130, <https://doi.org/10.1201/b21380-12>.
- Fleury, S., 2009, Land use policy and practice on karst terrains: Living on Limestone: New York, Springer, 187 p.
- Ford, D.C., and Williams, P.W., 2007, Karst Geomorphology and Hydrology: Chichester, John Wiley & Sons, Ltd., 562 p.
- Foster, D.G., 1999, Cave Management in the United States: An Overview of Significant Trends and Accomplishments: *in* Rea, G.T., ed., Proceedings of the 1999 National Cave and Karst Management Symposium, October 19–22: Chattanooga, Southeastern Cave Conservancy, p. 59–63.
- Groves, C., Polk, J., Miller, B., Kambesis, P., Bolster, C., Vanderhoff, S., Tyrie, B., Ruth, M., Ouellette, G., Osterhoudt, L., Nedvidek, D., McClanahan, K., Lawhon, N., and Hall, H., 2013, The Western Kentucky University Crumps Cave Research and Education Preserve: *in* Land, L. and Joop, M.W., eds., 20th National Cave and Karst Management Symposium, October 4-9: Carlsbad, National Cave and Karst Research Institute, p. 105–110.
- HCCC (Hart County Chamber of Commerce), 2013, Discover Hart County, Kentucky: [https://www.hartcountky.org/Directory\\_To\\_Print.pdf](https://www.hartcountky.org/Directory_To_Print.pdf), [accessed Sept. 26, 2018].
- HCPC (Hart County Planning Commission), 2007, Subdivision Regulations: Design and Development Standards: <https://hartcountky.org/wp-content/uploads/2019/12/subdivision.pdf>, [accessed Oct. 18, 2020].
- HCPC (Hart County Planning Commission), 2020, Hart County Comprehensive Plan Update 2020: [https://www.klc.org/userfiles/files/Hart\\_County\\_Comp\\_Plan\\_Final\\_Web.pdf](https://www.klc.org/userfiles/files/Hart_County_Comp_Plan_Final_Web.pdf), [accessed Oct. 16, 2020].
- Jarvis, T., Giordano, M., Puri, S., Matsumoto, K., and Wolf, A., 2005, International borders, ground water flow, and hydroschizophrenia: Groundwater, v. 43, no. 5, p. 764–770, <https://doi.org/10.1111/j.1745-6584.2005.00069.x>.
- Jiang, Y., Cao, M., Yuan, D., Zhang, Y., and He, Q., 2018, Hydrogeological characterization and environmental effects of the deteriorating urban karst groundwater in a karst trough valley: Nanshan, SW China: Hydrogeology Journal, v. 26, no. 5, p. 1487–1497, <https://doi.org/10.1007/s10040-018-1729-y>.
- KGA (Kentucky General Assembly), 2020, Kentucky Administrative Regulations: Title 401, Energy and Environment Cabinet – Department for Environmental Protection: <https://apps.legislature.ky.gov/law/kar/TITLE401.HTM>, [accessed Oct. 18, 2020].
- KGS (Kentucky Geological Survey), 1997, Detailed Info About This Well (Casing & Lithologic), Kentucky Groundwater Data Repository: <https://kgs.uky.edu/kgsweb/datasearching/water/wellinfo.asp?id=40004470&fromThickbox=true&height=450&width=600>, [accessed Oct. 23, 2018].
- Keranen, K., and Kolvoord, R., 2014, Making Spatial Decisions Using GIS and Remote Sensing: A Workbook: Redlands, Esri Press Academic, 300 p.
- Knierim, K.J., Hays, P.D., and Bowman, D., 2015, Quantifying the variability in *Escherichia coli* (*E. coli*) throughout storm events at a karst spring in northwestern Arkansas, United States: Environmental Earth Sciences, v. 74, no. 6, p. 4607–4623, <https://doi.org/10.1007/s12665-015-4416-5>.
- Lewis, J., 1995, The devastation and recovery of caves and karst affected by industrialization: *in* Rea, G.T., ed., Proceedings of the 1995 National Cave Management Symposium, Spring Mill State Park, October 25–28: Mitchell, National Cave Management Symposium Steering Committee, p. 214–227.
- Li, G., Goldscheider, N., and Field, M.S., 2016, Modeling karst spring hydrograph recession based on head drop at sinkholes: Journal of Hydrology, v. 542, p. 820–827, <https://doi.org/10.1016/j.jhydrol.2016.09.052>.
- Marín, L.E., Steinich, B., Pacheco, J., and Escolero, O.A., 2000, Hydrogeology of a contaminated sole-source karst aquifer, Mérida, Yucatán, Mexico: Geofísica International, v. 39, no. 4, p. 359–365, <https://doi.org/10.22201/igeof.00167169p.2000.39.4.246>.
- McGrain, P., and Currens, J.C., 1978, Topography of Kentucky: Special Publication 25, Kentucky Geological Society, 76 p.
- Meiman, J., Groves, C., and Herstein, S., 2001, Cave dye tracing and drainage basin divides in the Mammoth Cave Karst Aquifer, Kentucky: *in* Kuniandy, E.L., ed., U.S. Geological Survey Karst Interest Group Proceedings, St. Petersburg, FL, Feb. 2001: Reston, U.S. Geological Survey, p. 179–185.
- Milanović, P., 2016, Optimal water management – Prerequisite for regional socio-economic development in the karst of the south-eastern Dinarides: *in* Stevanović, Z., Krešić, N., and Kukurić, N., eds., Karst without Boundaries: Leiden, CRC Press/Balkema, 364 p., <https://doi.org/10.1201/b21380-11>.



- Murdoch, J., Bitting, C., and Van Brahana, J., 2016, Characterization of the karst hydrogeology of the Boone Formation in Big Creek Valley near Mt. Judea, Arkansas – documenting the close relation of groundwater and surface water: *Environmental Earth Sciences*, v. 75, no. 16, Article 1160, <https://doi.org/10.1007/s12665-016-5981-y>.
- Nedvidek, D., 2014, Evaluating the Effectiveness of Regulatory Stormwater Monitoring Protocols on Groundwater Quality in Urbanized Karst Regions [M.S. thesis]: Bowling Green, Western Kentucky University, 136 p.
- Osborne, C.N., 2018, Land-Use Impacts on the Hydrology of the Hidden River Groundwater Subbasin, Horse Cave, Hart County, Kentucky. [M.S. Geoscience thesis], Department of Geography and Geology, Western Kentucky University, Bowling Green, KY. Online at: <https://digital-commons.wku.edu/theses/3078/>, <https://doi.org/10.1130/abs/2018AM-324422>.
- Palmer, A.N., 1995, *A Geological Guide to Mammoth Cave National Park*: Teaneck, Zephyrus Press, 196 p.
- Palmer, A.N., 2007, *Cave Geology*: Dayton, Cave Books, 454 p.
- Quinlan, J.F., and Ewers, R.O., 1989, Subsurface drainage in the Mammoth Cave area: *in* White, W.B., and White, E.L., eds., *Karst Hydrology: Concepts from the Mammoth Cave Area*: New York, Van Nostrand Reinhold, 346 p, [https://doi.org/10.1007/978-1-4615-7317-3\\_3](https://doi.org/10.1007/978-1-4615-7317-3_3).
- Quinlan, J.F., and Rowe D.R., 1977, *Hydrology and Water Quality in the Central Kentucky Karst: Phase I*, University of Kentucky: Water Resources Research Institute, Report No. 101, 93 p.
- Raedts, C., and Smart, C., 2015, Tracking of karst contamination using alternative monitoring strategies: Hidden River Cave, Kentucky: *in* Doctor, D.H., Land, L., and Stephenson, J.B., eds., *Proceedings of the 14<sup>th</sup> Multidisciplinary Conference on Sinkholes and the Engineering and Environmental Impacts of Karst*, Rochester, MN, Oct. 2015: Carlsbad, NM, National Cave and Karst Research Institute, p. 327–336, <https://doi.org/10.5038/9780991000951.1055>.
- Ravbar, N., and Šebela, S., 2015, The effectiveness of protection policies and legislative framework with special regard to karst landscapes: insights from Slovenia: *Environmental Science & Policy*, v. 51, p. 106–116, <https://doi.org/10.1016/j.envsci.2015.02.013>.
- Ray, J.A., and Currens, J.C., 1998, Mapped Karst Ground-Water Basins in the Campbellsville 30 × 60 Minute Quadrangle: Lexington, Kentucky Geological Survey, Map and Chart Series 17, Series XI, 1:100,000, 2 p.
- Richardson, J.J., 2018, Fitting regulatory square pegs into round holes: local land use regulation: *in* karst terrain: *in* White, W.B., Herman, J.S., Herman, E.K., and Rutigliano, M., eds., *Karst Groundwater Contamination and Public Health: Beyond Case Studies*: Berlin, Springer, 347 p.
- Ryan, M., and Meiman, J., 1996, An examination of short-term variations in water quality at a karst spring in Kentucky: *Groundwater*, v. 34, no. 1, p. 23–30, <https://doi.org/10.1111/j.1745-6584.1996.tb01861.x>.
- Schreiber, M.E., Schwartz, B.F., Orndorff, W., Doctor, D.H., Eagle, S.D., and Gerst, J.D., 2015, Instrumenting caves to collect hydrologic and geochemical data: case study from James Cave, Virginia: *in* Younos, T., and Parece, T.E., eds., *Advances in Watershed Science and Assessment*: Berlin, Springer, p. 205–231, [https://doi.org/10.1007/978-3-319-14212-8\\_8](https://doi.org/10.1007/978-3-319-14212-8_8).
- Stevanović, Z., Kukurić, N., Pekaš, Ž., Jolović, B., Pambuku, A., and Radojević, D., 2016, Dinaric Karst Aquifer – One of the world's largest trans-boundary systems and an ideal location for applying innovative and integrated water management: *in* Stevanović, Z., Krešič, N., and Kukurić, N., eds., *Karst Without Boundaries*: Leiden, CRC Press/Balkema, 364 p., <https://doi.org/10.1201/b21380-3>.
- Tagne, G.V., and Dowling, C., 2018, Inferring groundwater flow and recharge from time series analysis of storm responses in a karst aquifer of southeastern Kentucky (USA): *Hydrogeology Journal*, v. 26, no. 8, p. 2649–2668, <https://doi.org/10.1007/s10040-018-1837-8>.
- Taylor, A., Curnow, R., Fletcher, T., and Lewis, J., 2007, Education campaigns to reduce stormwater pollution in commercial areas: do they work?: *Journal of Environmental Management*, v. 84, no. 3, p. 323–335, <https://doi.org/10.1016/j.jenvman.2006.06.002>.
- Theesfeld, I., 2010, Institutional challenges for national groundwater governance: Policies and issues: *Groundwater*, v. 48, no. 1, p. 131–142, <https://doi.org/10.1111/j.1745-6584.2009.00624.x>.
- Turpaud, P., Zini, L., Ravbar, N., Cucchi, F., Petrič, M., and Urbanc, J., 2018, Development of a protocol for the Karst Water Source Protection Zoning: Application to the classical karst region (NE Italy and SW Slovenia): *Water Resources Management*, v. 32, no. 6, p. 1953–1968, <https://doi.org/10.1007/s11269-017-1882-4>.
- White, W.B., Watson, R.A., Pohl, E.R., and Brucker, R.W., 1970, The Central Kentucky Karst: *Geographical Review*, v. 60, p. 88–115, <https://doi.org/10.2307/213346>.
- Wilson, J., and Rocha, C., 2016, A combined remote sensing and multi-tracer approach for localising and assessing groundwater-lake interactions: *International Journal of Applied Earth Observation and Geoinformation*, v. 44, p. 195–204, <https://doi.org/10.1016/j.jag.2015.09.006>.
- Worthington, S.R.H., Ford, D.C., and Davies, G.J., 2000, Matrix, fracture and channel components of storage and flow in a Paleozoic limestone aquifer: *in* Sasowsky, I.D. and Wicks, C.M., eds., *Groundwater Flow and Contaminant Transport in Carbonate Aquifers*: Rotterdam, A.A. Balkema, 203 p.
- Zhou, W., 2007, Drainage and flooding in karst terranes: *Environmental Geology*, v. 51, no. 6, p. 963–973, <https://doi.org/10.1007/s00254-006-0365-3>.

## GUIDE TO AUTHORS

The *Journal of Cave and Karst Studies* is a multidisciplinary journal devoted to cave and karst research. The *Journal* is seeking original, unpublished manuscripts concerning the scientific study of caves or other karst features. Authors do not need to be members of the National Speleological Society, but preference is given to manuscripts of importance to North American speleology.

**LANGUAGES:** The *Journal of Cave and Karst Studies* uses American-style English as its standard language and spelling style, with the exception of allowing a second abstract in another language when room allows. In the case of proper names, the *Journal* tries to accommodate other spellings and punctuation styles. In cases where the Editor-in-Chief finds it appropriate to use non-English words outside of proper names (generally where no equivalent English word exist), the *Journal* italicizes them. However, the common abbreviations i.e., e.g., et al., and etc. should appear in roman text. Authors are encouraged to write for our combined professional and amateur readerships

**CONTENT:** Each paper will contain a title with the authors' names and addresses, an abstract, and the text of the paper, including a summary or conclusions section. Acknowledgments and references follow the text. Manuscripts should be limited to 6,000 words and no more than 10 figures and 5 tables. Larger manuscripts may be considered, but the *Journal* reserves the right to charge processing fees for larger submissions.

**ABSTRACTS:** An abstract stating the essential points and results must accompany all articles. An abstract is a summary, not a promise of what topics are covered in the paper.

**STYLE:** The *Journal* consults The Chicago Manual of Style on most general style issues.

**REFERENCES:** In the text, references to previously published work should be followed by the relevant author's name and date (and page number, when appropriate) in brackets. All cited references are alphabetical at the end of the manuscript with senior author's last name first, followed by date of publication, title, publisher, volume, and page numbers. Geological Society of America format should be used (see [http://www.geosociety.org/documents/gsa/pubs/GSA\\_RefGuide\\_Examples.pdf](http://www.geosociety.org/documents/gsa/pubs/GSA_RefGuide_Examples.pdf)). Please do not abbreviate periodical titles. Web references are acceptable when deemed appropriate. The references should follow the style of: Author (or publisher), year, Webpage title: Publisher (if a specific author is available), full URL (e.g., <http://www.usgs.gov/citguide.html>), and the date the website was accessed in brackets. If there are specific authors given, use their name and list the responsible organization as publisher. Because of the ephemeral nature of websites, please provide the specific date. Citations within the text should read: (Author, Year).

**SUBMISSION:** Manuscripts are to be submitted via the PeerTrack submission system at <http://www.edmgr.com/jcks/>. Instructions are provided at that address. At your first visit, you will be prompted to establish a login and password, after which you will enter information about your manuscript and upload your manuscript, tables, and figure files. Manuscript files can be uploaded as DOC, WPD, RTF, TXT, or LaTeX. Note: LaTeX files should not use any unusual style files; a LaTeX template and BiBTeX file may be obtained from the Editor-in-Chief. Table files can be uploaded as DOC, WPD, RTF, TXT, or LaTeX files and figure files can be uploaded as TIFF, AI, EPS, or CDR files. Extensive supporting data may be placed on the *Journal's* website as supplemental material at the discretion of the Editor-in-Chief. The data that are used within a paper must be made available upon request. Authors may be required to provide supporting data in a fundamental format, such as ASCII for text data or comma-delimited ASCII for tabular data.

**DISCUSSIONS:** Critical discussions of papers previously published in the *Journal* are welcome. Authors will be given an opportunity to reply. Discussions and replies must be limited to a maximum of 1000 words and discussions will be subject to review before publication. Discussions must be within 6 months after the original article appears.

**MEASUREMENTS:** All measurements will be in Systeme Internationale (metric) except when quoting historical references. Other units will be allowed where necessary if placed in parentheses and following the SI units.

**FIGURES:** Figures and lettering must be neat and legible. Figure captions should be on a separate sheet of paper and not within the figure. Figures should be numbered in sequence and referred to in the text by inserting (Fig. x). Most figures will be reduced, hence the lettering should be large. Photographs must be sharp and high contrast. Figures must have a minimum resolution of 300 dpi for acceptance. Please do not submit JPEG images.

**TABLES:** See <http://caves.org/pub/journal/PDF/Tables.pdf> to get guidelines for table layout.

**COPYRIGHT AND AUTHOR'S RESPONSIBILITIES:** It is the author's responsibility to clear any copyright or acknowledgement matters concerning text, tables, or figures used. Authors should also ensure adequate attention to sensitive or legal issues such as land owner and land manager concerns or policies and cave location disclosures.

**PROCESS:** All submitted manuscripts are sent out to at least two experts in the field. Reviewed manuscripts are then returned to the author for consideration of the referees' remarks and revision, where appropriate. Revised manuscripts are returned to the appropriate Associate Editor who then recommends acceptance or rejection. The Editor-in-Chief makes final decisions regarding publication. Upon acceptance, the senior author will be sent one set of PDF proofs for review. Examine the current issue for more information about the format used.

# Journal of Cave and Karst Studies

Volume 84 Number 1 March 2022

## CONTENTS

### Article

3D Resistivity Survey Over Mapped Caves in Eogenetic Karst Terrane, west-central Florida, USA  
*Charles W. McCrackin, Henok G. Kiflu, Sarah E. Kruse, Philip E. van Beynen, Jason S. Polk and Ben. Miller*

1

### Article

Geology and Palaeoenvironment of Karin Tak Cave (Lesser Caucasus)  
*Avagyan Ara, Sahakyan Lilit H., Igityan Hayk, Gevorgyan Mikayel, Sahakyan Kristina, Antonosyan Maria, Tepanosyan Gevorg, Sahakyan Lilit V., Atalyan Tatul, Grigoryan Taron, Aspaturyan Narek, Avagyan Seda, and Yepiskoposyan Levon*

14

### Article

Land-Use Impacts on the Hydrology of the Hidden River Groundwater Subbasin, Horse Cave, Hart County, Kentucky  
*Cesalea N. Osborne, David J. Keeling, Jason S. Polk, Patricia N. Kambesis, and Kevin B. Cary*

27

Visit us at [www.caves.org/pub/journal](http://www.caves.org/pub/journal)